Design of an 8x8 Cross-Configuration Butler Matrix with Interchangeable 1D and 2D Arrays

by

Chad Bartlett

B.Eng, University of Victoria, 2017

A Thesis Submitted in Partial Fulfillment of the Requirements for the Degree of

MASTER OF APPLIED SCIENCE

in the Department of Electrical and Computer Engineering

Design of an 8x8 Cross-Configuration Butler Matrix with
Interchangeable 1D and 2D Arrays

by

Chad Bartlett
B.Eng, University of Victoria, 2017

Supervisory Committee

Dr. Jens Bornemann, Supervisor
(Department of Electrical and Computer Engineering)

Dr. Thomas Darcie, Departmental Member
(Department of Electrical and Computer Engineering)

Supervisory Committee

Dr. Jens Bornemann, Supervisor

(Department of Electrical and Computer Engineering)

Dr. Thomas Darcie, Departmental Member

(Department of Electrical and Computer Engineering)

ABSTRACT

An ever-increasing demand for wider bandwidths in communication, radar, and imaging systems has emerged. In order to facilitate this growing demand, progressive research into millimeter-wave technologies has become vital in achieving next generation networks such as 5G. Being cost effective and easy to manufacture, Substrate Integrated Waveguide (SIW) circuits have been demonstrated as a viable candidate for high-frequency applications due to their low-loss, high quality-factor, and high power-handling capabilities.

Research on beam-forming networks, specifically the Butler matrix, has demonstrated powerful beam-steering capabilities through the use of passive component networks. Through these clever configurations, a cost effective and robust option is available for us to use. In order to further millimeter-wave research in this area, this thesis presents a modified configuration of the Butler Matrix in SIW that is physically reconfigurable; by separating the Butler matrix from the antenna array at a pre-selected point, the array can be easily interchanged with other 1-Dimensional, and 2-Dimensional slot antenna arrays. Although this system does not fall under the rigorous definitions of Reconfigurable Antennas, it should be noted that the interchangeability of 1 and 2 dimensional arrays is not typically expressed in Butler matrix configurations. Design and simulations are carried out in CST Microwave Studio to inspect individual components as well as system characteristics. Circuit prototypes are then manufactured and tested in an anechoic chamber to validate simulation results and the design approach.

Contents

List of Tables

List of Figures

List of Abbreviations

1-D 1 Dimensional

2-D 2 Dimensional

3-D 3 Dimensional

5G fifth generation cellular network technology

SIW Substrate Integrated Waveguide

SLL Sidelobe level

S-parameter Scattering Parameter

TE Transverse Electric

TEM Transverse Electromagnetic

TM Transverse Magnetic

TRL Thru, Reflect, Line

ACKNOWLEDGEMENTS

I would like the time to extend my gratitude and thank those who have helped me along the way:

Prof. Jens Bornemann, for being a great mentor, whose door has been always open.

CADMIC Research Group Members, Dr. Sara Salem, Alireza Seyfollahi, Gabriela Luciani, and Deisy Mamedes for their insight and wisdom along the way.

Thomas Francis, David Waltzman, and Ubercloud Inc. For their support of my research and providing remarkable computational power

Dr. Aidin Taeb and Dr. Safieddin Safavi-Naeini of the University of Waterloo For their support, insight and expertise with near-field measurements at the CIARS (Centre for Intelligent Antenna and Radio Systems) facility.

Ian Goode and Dr. Carlos Saavedra of Queens University For their support, insight and expertise with far-field measurements at the Queens University anechoic chamber.

Rogers Corporation, For their support of University research and donation of dielectric substrate materials.

Southwest Microwave, Inc. For their support of University research and donation of end-launch connectors.

Ainsley Morgan For her constant encouragement, love and unwavering support.

My family For all of their love and support.

Sometimes, we cant say 'I can do that,' but we can say 'its possible'.
Les Brown

DEDICATION

For my family, past, present, and future.

Chapter 1

Introduction

Progressive research into microwave and millimeter-wave technologies has become vital for the future of satellite, wireless, and communication systems. In order for technological trends to occur in industry, scientific advancements must propose a cost-effective solution that can be deployed on a global scale. *Substrate Integrated Waveguide* (SIW) has been demonstrated as a viable candidate for future high-frequency applications due to many significant attributes. Substrate integrated waveguide is designed to mimic a dielectric-filled rectangular waveguide; it is manufactured by coating the top and bottom of a dielectric substrate with metal ground planes, where the side walls are bound by rows of metallized vias through the substrate. Rectangular waveguide features such as low transmission loss, high-power handling, and high quality-factor can be embodied in substrate integrated waveguide while maintaining a compact, light weight, planar solution.

In order to achieve transmission or reception of a directional radio frequency signal, manipulation - or *steering* - of the beam pattern can be accomplished by mechanical or electronic means. While mechanical beam steering has its many uses, the physical size of rotational equipment and the operational delay from motion, both pose prominent complications that inhibit the abilities of mechanical beam scanning for high-speed and high-accuracy conditions such as communications or defense. Electronic steering, however, presents alternative solutions that can overcome these problems; several different methods of electronic steering can be reviewed in [1]. One notable method is *beamforming*, which can be sub-categorized into quasi-optical networks such as Rotman lenses, and circuit based networks such as Butler matrices [2], which each provide an ingenious method of controlling the direction of the beam.

Butler matrices are a family of passive reciprocal beamforming networks that allows an antenna array to be fed with predetermined phase shifts [3]. Recent research on substrate integrated waveguide Butler matrices has been able to demonstrate numerous uses with a diverse range of configurations. For instance, a 60 GHz end-fire circularly polarized septum antenna array with a 4x4 Butler matrix scheme was demonstrated in [4] and a 60 GHz end-fire magneto-electric dipole antenna array with an 8x8 Butler matrix scheme was demonstrated by [5]. Most relevant and influential

to the work of this thesis are the contributions of a broadside slot antenna array fed by a dual-layer 8x8 Butler matrix [6], a 2-dimensional scanning array utilizing dual-layer 4x8 Butler matrices for sidelobe level (SLL) suppression [7] and a 94-GHz, 2-dimensional multibeam antenna on multifolded SIW [8]. Equally important are papers presented on a broadband microstrip 8x8 Butler matrix using coupled-line directional couplers [9] and an 8x8 Butler matrix utilizing quadrature couplers and Schiffman phase shifters [10].

1.1 Motivation

Applications such as 5G depend on large bandwidths at high frequencies [11]. By applying substrate integrated waveguide technology to Butler matrices, a viable option for millimeter-wave multi-beam applications can be exploited; this is especially true when compared with planar circuits such as microstrip, which tend to have higher losses at high frequencies, and with conventional rectangular waveguides which are bulky, expensive systems [12–14].

In order to further research in this field, a standard 8x8 Butler matrix is reorganized into a planar cross-configuration with the eight corresponding outputs separated at some distance. Each output line of the matrix carries 1/8th of the power. The excitation of a single input port determines a $\pm 22.5, \pm 67.5, \pm 112.5$, or ± 157.5 degree phase difference between the output ports. With the matrix scheme organized into a cross configuration on the first substrate integrated layer, eight dual-layer folded passband filters are connected to facilitate the transfer of power into the next layer. By using dual-layer folded passband filters, the benefit of reversing the direction of signal flow and the mitigation of any frequencies outside of the selected passband can be achieved. The outputs of the folded passband filters are connected to the second substrate integrated layer. It is important to note here that the filters act as a detachment point for the second substrate integrated layer; this detachment point allows for different 1- and 2-dimensional antenna array configurations to be interchanged for desirable beam patterns. In this thesis, two interchangeable configurations are demonstrated: the first detachable array reorganizes the separated output signal into a staggered 2x8 slot antenna array for 1-dimensional beam scanning, and the second array reorganizes the separated output signal into a 2x4 center-slot antenna array for 2-dimensional beam scanning.

The final structure is able to control 8 beams with either 1- or 2-dimensional coverage depending on the interchangeable top layer by selecting which input port to excite. The proposed design is created and analyzed with the electromagnetic field solver CST Microwave Studio. In order to validate the simulation results, a prototype of the beamforming network is fabricated; the radiation patterns, return loss, and isolation values are measured and compared to simulation results between 28.5 and 31.5 GHz.

1.2 Contributions

The contributions made by this research are as follows:

- A new substrate integrated waveguide 8x8 cross-configuration beamforming network is demonstrated with a 10 dB return loss and isolation bandwidth between 28.5 and 31.5 GHz.
- By arranging the input connections of the beamforming network on the first substrate integrated layer, detachable array structures of the second layer demonstrate a level of configurability that is not typically expressed in standard Butler matrix configurations. A measured 2x8 slot antenna array provides a 1-dimensional beam sweep with approximately 7.6 to 13.0 dB gain over eight beam angles, while a measured 2x4 slot antenna array provides a 2-dimensional beam sweep with approximately 7.6 to 10.1 dB gain over eight beam angles.
- A research publication has been submitted to the open-access scientific journal IEEE Access, entitled Cross-Configuration Substrate Integrated Waveguide Beam-Forming Network for 1D and 2D Beam Patterns. This article is pending revisions and intended for publication.

1.3 Thesis Overview

This section outlines the structure of the following chapters in this thesis.

Chapter 2 describes the fundamental concepts and theory of substrate integrated waveguides (SIWs), H-plane couplers, slot antennas, folded passband filters, phase shifters, Butler matrices and microstrip feed lines.

Chapter 3 discusses the individual component design and the accumulation of the components as a dual-layer 8x8 Butler matrix structure for beamforming. The design details are followed by a discussion on the S-parameter results that are obtained from CST Microwave Studio; where permitted, the corresponding radiation patterns are discussed as well.

The first section describes each individual components design. The second section describes the bottom layer as the 8x8 Butler matrix feed network, the two top-layer arrays for 1-dimensional and 2-dimensional beam patterns, and finally the system as a whole; a cross-configuration 8x8 Butler matrix with interchangeable arrays.

Chapter 4 describes the fabrication and measurements of the prototype beamforming network. The measured S-parameter and radiation pattern results are plotted; a comparison is presented between the simulated and measured results.

Chapter 5 discusses future work avenues, proposed developments for the system and a final conclusion.

Chapter 2

Fundamental Concepts

This chapter discusses the fundamental concepts, important parameters, and relevant literature in which this thesis work is based. Understanding of each individual topic is crucial for the design and proper operation of the proposed beamforming network. This chapter is divided into topics in which an individual technology or component is described, relevant equations are discussed, and the basic design guidelines are reviewed. This chapter is divided into the following subsections:

- Substrate Integrated Waveguides (SIWs)
- H-Plane Couplers
- Slot Radiators
- Multilayer SIW Transitions
- Phase Shifters
- Butler Matrices
- Microstrip to SIW Transitions.

2.1 Substrate Integrated Waveguides

Substrate integrated waveguide (SIW) consists of a dielectric substrate with two parallel rows of metallized rectangular or circular via holes, and a metallized top and bottom ground plane. The metallized via holes act as sidewalls, while the path formed by the via holes and the metallized top and bottom ground planes allow electromagnetic waves to propagate through the substrate; the waveguide arrangement and behaviour is analogous to that of a TE_{10} dielectric filled waveguide [15,16]. The valuable characteristics of metallic waveguides such as low loss, high quality factor and electromagnetic shielding, are combined with the advantages of microstrip technology

such as low cost, light weight, and ease of fabrication to form a suitable technology for future millimeter-wave applications.

2.1.1 Design of Via Diameter and Pitch

Detailed analysis of the via diameter and pitch spacing can be reviewed in [16]. To this end, the operating *region of interest* - defined by equations 2.1(a)-(c), where λ_c is the cutoff wavelength - is important design consideration that allows the substrate integrated waveguide to operate as an equivalent dielectric-filled waveguide structure.

$$p > d \tag{2.1a}$$

$$0.05 \leq \frac{p}{\lambda_c} \leq 0.25 \tag{2.1b}$$

$$0.5 \leq \frac{d}{p} \leq 0.83 \tag{2.1c}$$

For the circuit to be physically realizable, Equation 2.1(a) requires that the pitch dimension p (the center-to-center spacing between vias) must always be larger than the via hole diameter d, Equation 2.1(b) is required to deter any band gaps from appearing in the operating bandwidth, and Equation 2.1(c) aims to mitigate any leakage loss between the vias to a negligible level. Figure 2.1(a) illustrates the region of interest discussed, while Figure 2.1(b) depicts basic substrate integrated waveguide geometry.

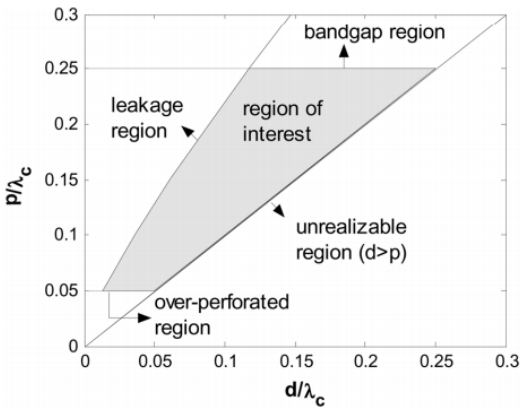

(a)

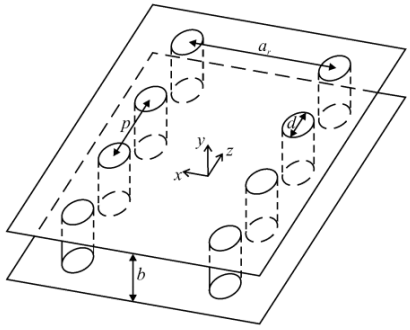

(b)

Figure 2.1: (a) Region of interest for SIW design [16]. (b) Perspective view of SIW structure [16].

2.1.2 Equivalent Waveguide Width

As discussed, the TE_{10} mode in a substrate integrated waveguide is comparable to that of a conventional dielectric-filled waveguide. To design the equivalent dielectric-filled waveguide width w_{equi}, the desired cutoff frequency f_c and dielectric constant ϵ_r of the substrate must be selected. Equation 2.2 is used to determine w_{equi} where the cutoff frequency is bounded by the operating frequency range $1.25f_c$ - $1.9f_c$. To mimic an equivalent dielectric-filled waveguide, several methods have been developed for the accurate placement of the via holes by [17–22]. For this thesis work, the design equation from [22] is selected due to its accuracy. Equation 2.3 formulates the actual substrate integrated waveguide width, a_{SIW}. The values of d and p are selected based on Equations 2.1 (a)-(c), from [16].

$$w_{equi} = \frac{c}{2f_c\sqrt{\varepsilon_r}} \tag{2.2}$$

$$a_{SIW} = w_{equi} + p(0.766e^{0.4482d/p} - 1.176e^{-1.214d/p}) \tag{2.3}$$

Figure 2.2 demonstrates the equivalent dielectric-filled waveguide, and substrate integrated waveguide geometry, where Figure 2.3 depicts the simulation of the electromagnetic field contained in an equivalent dielectric-filled waveguide, and in its synonymous substrate integrated waveguide, respectively. Inspection of Figure 2.3 allows for a visualization of the TE_{10} mode in both structure types; it can be noted that the substrate integrated waveguide structure exhibits negligible leakage loss due to the accurate selection of d and p from Equations 2.1 (a)-(c) [23].

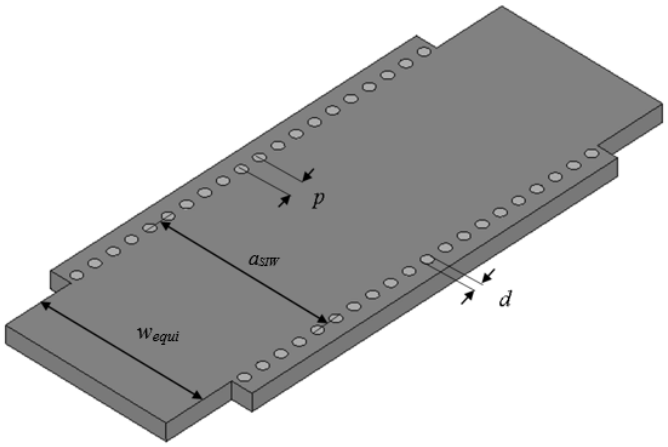

Figure 2.2: Equivalent dielectric-filled waveguide and SIW geometry. Metallization layers not shown.

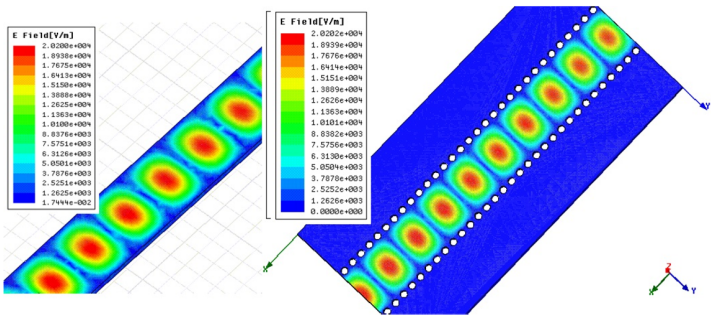

Figure 2.3: Electric field propagation in rectangular waveguide (left) and in SIW (right) [23].

2.2 H-Plane Couplers

Two types of H-plane couplers are demonstrated in this thesis; the *quadrature hybrid coupler*, and the *cross-over coupler*. Both couplers are four port passive devices and completely symmetric; this allows for any port to be designated as the input port while the output ports are either connected for use, or simply isolated. Theory and design of couplers has been extensively researched in conventional rectangular waveguides and - more recently - has been applied to substrate integrated waveguide circuit theory; References [24–27] demonstrate several key findings as well as exemplify the design approach. For this section, basic theory is discussed and then applied to substrate integrated waveguide technology.

2.2.1 Quadrature Hybrid Coupler

The quadrature hybrid coupler is derived from a *Riblet short slot* type coupler [24]. The coupler can be described as two waveguides placed side-by-side with a section of the center wall removed. The removal of the center wall - and compaction of the outer walls - allows for the TE_{10} and TE_{20} modes to propagate within the structure; this section is viewed as the *coupling section* [24, 28]. Figure 2.4 depicts the ideal quadrature hybrid junction while Figure 2.5 depicts a perspective view of the Riblet short slot coupler in rectangular waveguide technology. Port (P1) serves as the input port, ports (P2) and (P3) serve as the through and coupled ports, and port (P4) is isolated due to the geometry of the structure.

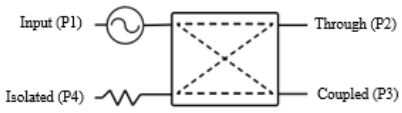

Figure 2.4: Ideal hybrid quadrature coupler.

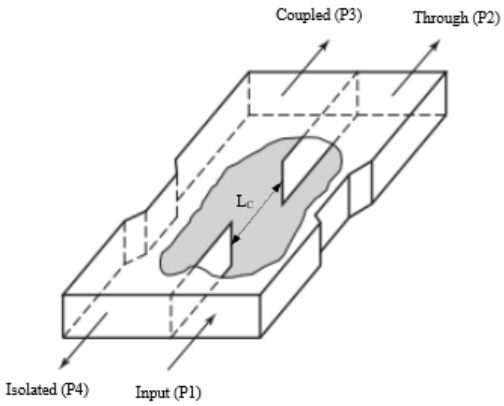

Figure 2.5: Geometry of a hybrid quadrature coupler in conventional rectangular waveguide - Modified from [28].

The length L_C of the coupling section determines the *coupling ratio* between output ports (P2) and (P3). For a -3 dB coupling ratio, an equal power division must be achieved by the proper selection of L_C. An initial length can be obtained from equation 2.4 where $\Delta\theta = \pi/2$ is required for quadrature coupling. Variables β_1 and β_2 are the propagation constants of the even and odd modes (TE_{10} and TE_{20}). Further analysis can be reviewed in [24] and [29]. Optimization of the structure's parameters in both rectangular waveguide and substrate integrated waveguide is necessary to achieve the desired performance.

$$\Delta\theta = L_c(\beta_1 - \beta_2) \tag{2.4}$$

For a hybrid quadrature coupler in substrate integrated waveguide, Equations 2.1-2.4 provide the initial design parameters. Figure 2.6 illustrates a quadrature hybrid coupler in substrate integrated waveguide technology.

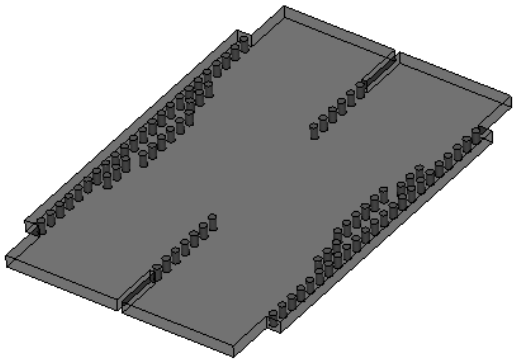

Figure 2.6: Hybrid quadrature coupler in SIW. Metallization layers not shown.

2.2.2 Cross-Over Coupler

The cross-over coupler makes use of two back-to-back quadrature hybrid couplers [30]. The cascaded arrangement of the two couplers allows for isolation of two crossing paths. For example, if port 1 (P1) is selected as an input, ports 2 (P2) and 4 (P4) are isolated, while port 3 (P3) serves as the output (through) port. It is important to note that the connection between mirrored quadrature couplers requires fine-tuning to achieve an optimal result; further details are discussed in Chapter 3. Figure 2.7 (a) illustrates an ideal cross-over coupler junction, while Figure 2.7 (b) depicts a cross-over coupler in substrate integrated waveguide technology.

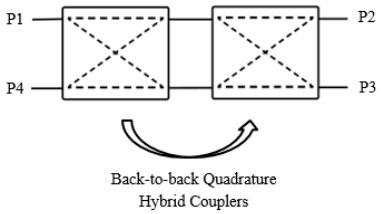

(a)

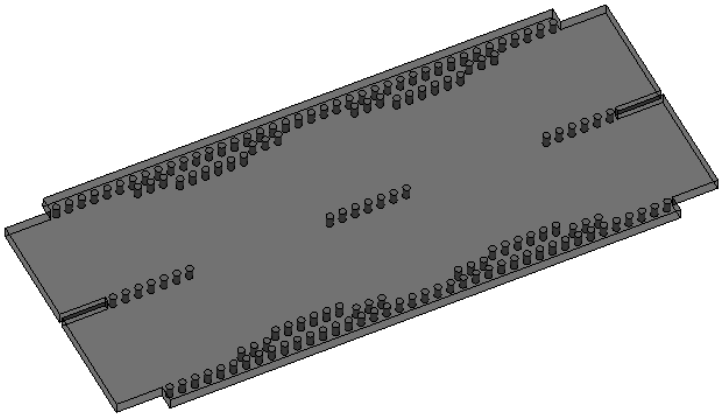

(b)

Figure 2.7: (a) Ideal cross-over coupler. (b) Cross-over coupler in SIW. Metallization layers not shown.

2.3 Slot Radiators

Radiating elements play a fundamental role in the way information is communicated in modern wireless systems. The transmission and reception of signals is facilitated by the transfer of electromagnetic waves to and from these transducers. Many different designs for radiating elements are available as an interface between the circuit and free

space. Using Babinets principle, one of the simplest schemes for a radiating element can be designed; the *slotted waveguide antenna* [31–35]. In this type of antenna, the radiating slots are part of the feeding waveguide. For the electromagnetic waves to pass between the waveguide and into free space, the surface current distribution along the waveguide walls must encounter a disturbance, where for this instance, the disturbance is the introduction of the slot. By creating a potential difference over the slot, power is coupled from the modal field through the slot, and out into free space [31–35].

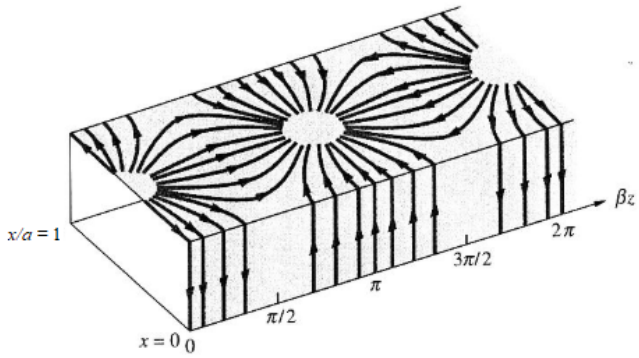

Figure 2.8: Surface currents in a rectangular waveguide. Modified from [36].

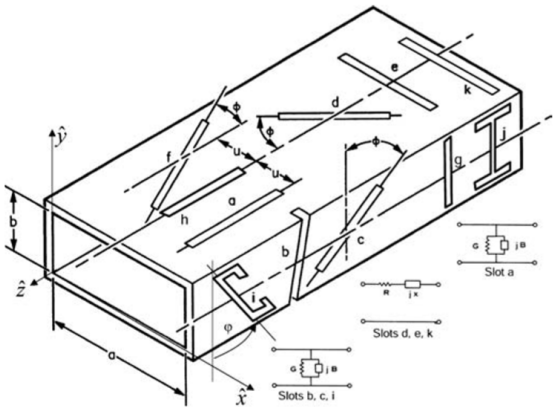

Figure 2.9: Slots cut in the walls of a rectangular waveguide. Slot g does not radiate because the slot is lined up with the direction of the sidewall current. Slot h does not radiate because the transverse current is zero there. Slots a, b, c, i, and j are shunt slots because they interrupt the transverse currents (J_x , J_y) and can be represented by two-terminal shunt admittances. Slots e, k, and d interrupt J_z and are represented by series impedance. Slot d interrupts J_x, but the excitation polarity is opposite on either side of the waveguide center-line, thus preventing radiation from that current component. Both J_x and J_z excite slot f. A Pi- or T-impedance network can represent it [33].

An understanding of waveguide modes TE_{mn} and surface currents J_{xy} is necessary for the design of slot antennas. Figure 2.8 depicts the distribution of surface currents flowing along the waveguide walls [36], while a detailed analysis of the interaction between the TE_{10} modal field and slot distribution is illustrated in Figure 2.9 [33].

Because substrate integrated waveguides behave similar to conventional rectangular waveguides for the TE_{10} mode, the principles for slot antennas can be applied to substrate integrated waveguides [19] and are further discussed in Chapter 3. Two different types of slot antenna schemes are proposed in substrate integrated waveguide for this thesis; a *linear resonant slot antenna* for the 1-dimensional array, and a *resonant center-slot antenna* for the 2-dimensional array. Preliminary descriptions and concepts are discussed in the following subsections.

2.3.1 Linear Resonant Slot Antenna

For the 1-dimensional array, a linear resonant slot type antenna is selected. By staggering the slots across the waveguide center-line and distributing them by half of the guided wavelength ($\lambda_g/2$), the propagating TE_{10} waves interact with each of the slots with the same phase angle. The end of the waveguide is capped off by metal and is placed a quarter of the guided wavelength $\lambda_g/4$ spacing from the center of the last resonant slot. Figure 2.10 illustrates several linear resonant slots distributed along a conventional rectangular waveguide. Figure 2.11 depicts two resonant slots distributed on substrate integrated waveguide. The slot length is approximately $\lambda_g/2$ but later optimized for return loss and beam shape.

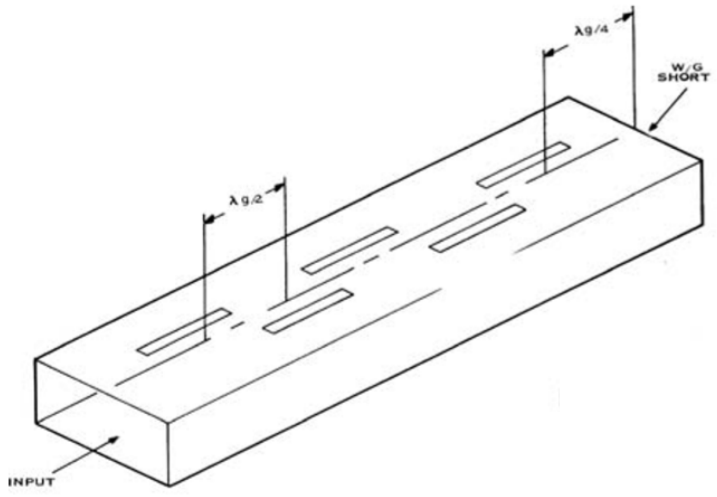

Figure 2.10: Slot antenna distribution in rectangular waveguide. Modified from [33].

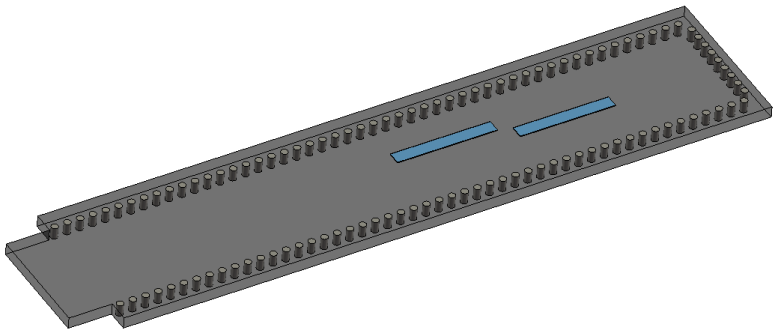

Figure 2.11: Slot antenna distribution in SIW. Metallization layers not shown; apertures (blue) indicate the slot locations.

2.3.2 Resonant Center-Slot Antenna

For the 2-dimensional array, a resonant center-slot type antenna is selected. In the previous section on *Linear Resonant Slot Antennas*, the distribution and phasing of the apertures is based on careful selection of position for the interaction with the TE_{10} mode's surface current. However, studying slot h in Figure 2.9 – a center-slot – we can determine that it cannot radiate due to its position; there is no transverse surface current at this point. In order for this slot to radiate, deviation of the incoming electric field needs to take place at this point to effectively disrupt the current distribution. One method for deviating the TE_{10} field can be accomplished by strategically inserting a via or metallic post in the proximity of the slot as demonstrated in [7]. Upon reaching the center slot and via, the electric field is pushed to the side of the waveguide wall, allowing for redistribution of the surface current.

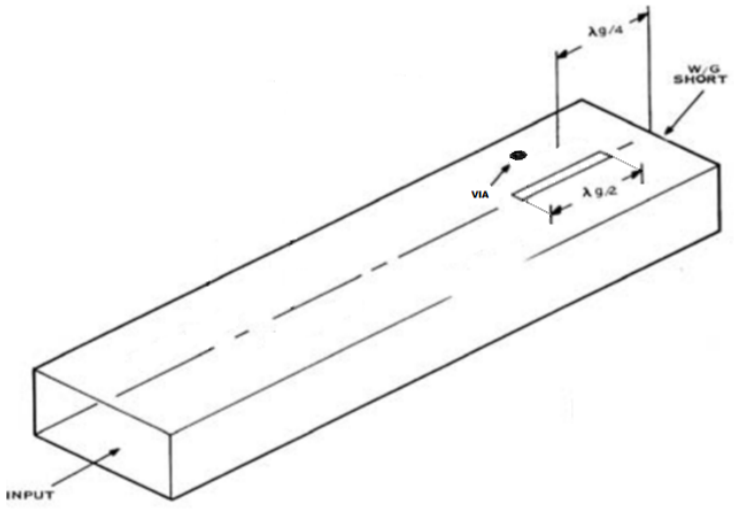

Figure 2.12: Center-slot antenna distribution in rectangular waveguide. Modified from [33].

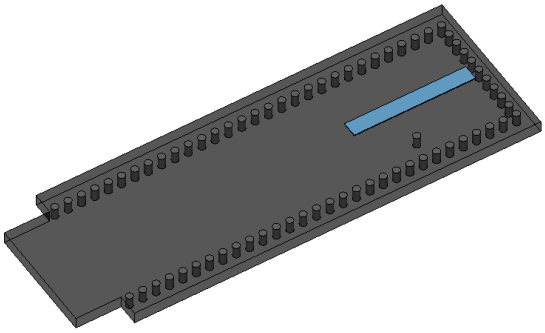

Figure 2.13: Center-slot antenna in SIW. Metallization layers not shown; aperture (blue) indicates the slot location

A single center-slot antenna with a metallized via in a conventional rectangular waveguide is depicted in Figure 2.12. The end of the waveguide is capped off by metal and is placed a quarter of the guided wavelength ($\lambda_g/4$) spacing from the center of the slot. Figure 2.13 depicts a single center-slot and via hole in substrate integrated waveguide. The slot length - approximately $\lambda_g/2$ - and via position is optimized for return loss and beam shape.

2.4 Multilayer SIW Transitions

E-plane layer-to-layer transitions are an important part of substrate integrated circuit development. The transfer of TE_{10} mode signals from one planar layer into another can be facilitated by several different techniques. These transitions have been demonstrated by [4,37–41] and several others. In this thesis, an E-plane transition with 180 degree directional change is required. Figure 2.14 exemplifies the ideal circuit transition, where variable a is the waveguide length, w is the transition slot, ϵ_r is the dielectric constant, and b is the waveguide height.

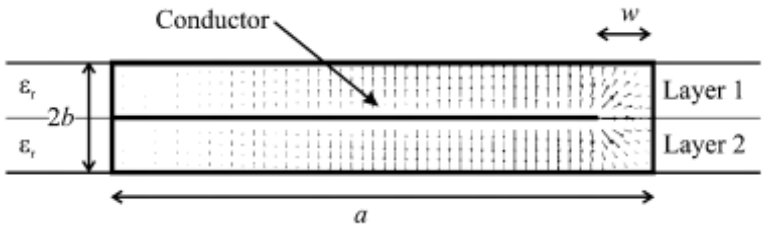

Figure 2.14: Cross-sectional view of TE_{10} layer-to-layer transition in conventional rectangular waveguides [40].

The use of filter theory, as demonstrated in [40–43], provides a unique way of transferring the electrical energy from one layer to the next while providing a 180 degree directional change. The obvious additional benefit of utilizing this type of transition is the ability to define passband filter properties. Figure 2.15 exemplifies

the desired transition in rectangular waveguide technology; a folded direct coupled filter [42]. A review on the design and synthesis of passband filter theory in [42, 44–49] helps to define the initial design of the Ka-band folded four-cavity filter as a transition mechanism in substrate integrated waveguide layers. Design details are discussed in Chapter 3.

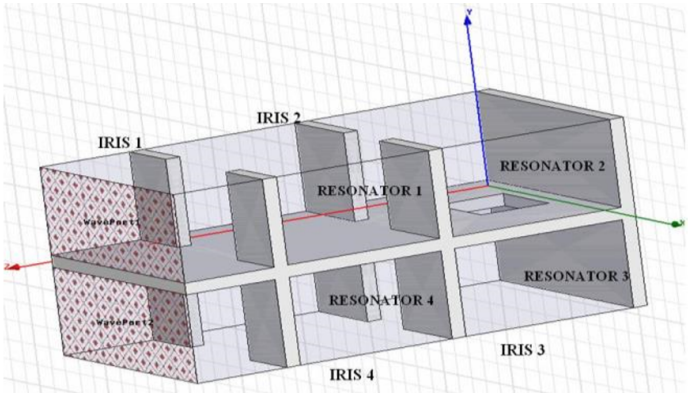

Figure 2.15: Folded direct coupled filter in conventional rectangular waveguide [42].

2.5 Phase Shifters

Phase shifters are an important part of signal distribution in electrical circuits. These components allow for the signal phase to vary from one area to the other while maintaining vital electrical characteristics such as insertion loss, and return loss. Several passive methods have been developed and presented in [50–54] for substrate integrated waveguides circuits. For this section, basic theory is discussed for two types of phase shifters - the *delay line* and the *equal-length unequal width line*. As mentioned above, phase variation between two electrical lines can be accomplished in several different ways. The simplest form is that of the delay line as shown in Figure 2.16 (a). This method uses the distinction between the electrical lengths to demonstrate the phase difference. The phase difference $\Delta\theta$ between ports 1 and 2, and ports 3 and 4 can be found using Equations 2.5. and 2.6, where f is the operating frequency, l_i is the length of the conductor, c is the speed of light, ϵ_r is the dielectric constant and w is the equivalent waveguide width [54]; which in the case of substrate integrated waveguide is equal to w_{equi} discussed in Section 2.1.2.

$$\Delta\theta = \beta(l_2 - l_1) \tag{2.5}$$

$$\beta = \sqrt{\left(\frac{2\pi f\sqrt{\varepsilon_r}}{c}\right)^2 - \left(\frac{\pi}{w}\right)^2} \tag{2.6}$$

(a) (b)

Figure 2.16: (a) Phase Delay Line. (b) Equal-length unequal-width phase shifter. Modified from [54].

Another method can be accomplished using an equal-length unequal-width type phase shifter. By modifying the width of the electrical line, a phase difference can be observed. Figure 2.16 (b) illustrates this type of phase shifter and a comparison can be made to that of Figure 2.16 (a). The phase difference $\Delta\theta$ between ports 1 and 2, and ports 3 and 4 can be found using Equation 2.7, where f is the operating frequency, l is the length of the width deviation, c is the speed of light, ϵ_r is the dielectric constant and w_i is the equivalent waveguide widths [54].

$$\Delta\theta = l\left[\sqrt{\left(\frac{2\pi f\sqrt{\varepsilon_r}}{c}\right)^2 - \left(\frac{\pi}{w_2}\right)^2} - \sqrt{\left(\frac{2\pi f\sqrt{\varepsilon_r}}{c}\right)^2 - \left(\frac{\pi}{w_1}\right)^2}\right] \tag{2.7}$$

2.6 Butler Matrices

Different from the sections discussed previously, Butler matrices [3] are a sophisticated network comprised of several components for the purpose of beamforming. By design, the arrangement of phase shifters, cross-over couplers, and hybrid couplers, can create a passive reciprocal network with 2^n inputs and 2^n outputs. The excitation of one of the inputs of the matrix distributes the power equally and introduces a progressive phase shift between each of the outputs. The selection of which input port to excite determines the angle of the phase progression at the outputs. The diffraction pattern created by the antennas at the output steers the beam, where the angle of the beam's direction is dependent on the phase progression observed at the outputs. To become familiar with the basic operation, Figure 2.17 illustrates an ideal 4x4 Butler matrix with antennas; the selection of an input - 1R, 2L, 2R, or 1L - determines the corresponding switched beam pattern at the output [55]. Determination of the beam angle β_i can be found using Equation 2.8, where α_i is the phase progression at the output of the matrix, κ is the wave number, and d is the distance between array elements. Detailed descriptions can be reviewed in [10, 32, 56, 57].

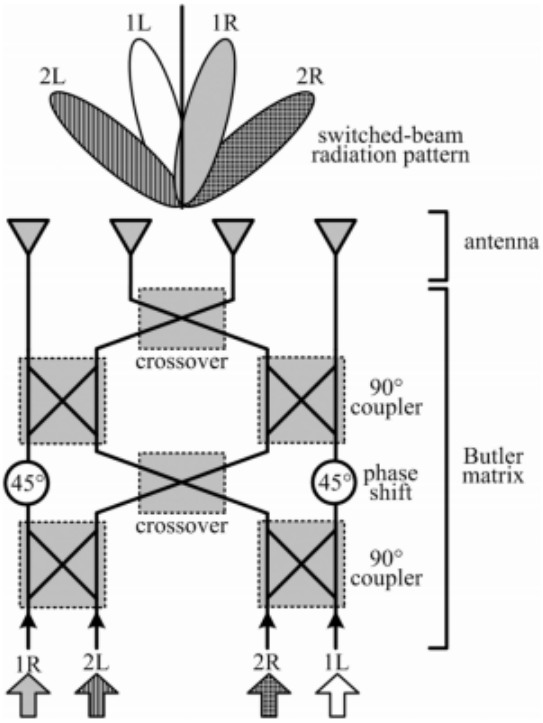

Figure 2.17: Ideal 4x4 Butler matrix scheme illustrating switched output beam patterns [55].

$$\beta_i = 90^\circ - \arccos\left(\frac{-\alpha_i}{\kappa d}\right) \tag{2.8}$$

A through review of the literature demonstrates many unique designs in a wide variety of technologies. Some of the key designs relative to this project can be reviewed here in [6–10, 58]. Each encompasses different operating characteristics and attempts to address attributes such as physical size and material cost while simultaneously optimizing characteristics such as isolation, return loss, and phase error.

For the purpose of this thesis, an 8x8 Butler matrix is selected for design. An ideal schematic is illustrated in Figure 2.18. The phase shifters ϕ_1, ϕ_2, and ϕ_3 correspond to -67.5, -22.5, and +45 degrees, respectively. For selection of input ports 1 through 8, the phase progressions between output ports 9 through 16 will correspond to either ± 22.5, ± 67.5, ± 112.5, or ± 157.5 degrees. The layout of this ideal 8x8 Butler matrix makes use of 8 phase shifters, 12 quadrature couplers, and 16 cross-over couplers. Further design details and individual components are reviewed in Chapter 3.

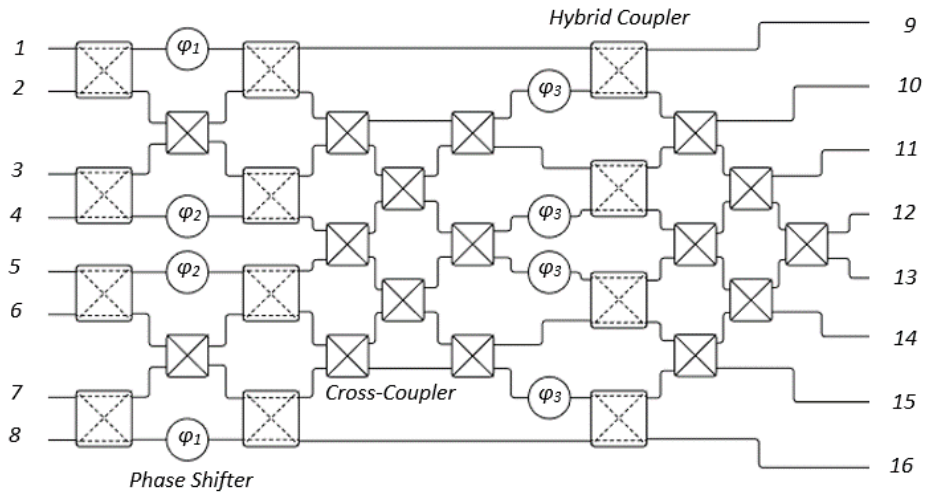

Figure 2.18: Ideal 8x8 Butler matrix scheme.

2.7 Microstrip to SIW Transitions

Microstrip circuits are a frequently used technology for high-frequency applications and have been heavily adopted by industry. The vast majority of network analyzers and spectrum analyzers on the market can handle the calibration and mounting of microstrip circuits. To this end, specialized microstrip transitions can function as a practical medium for testing rectangular or substrate integrated waveguides. The basics of microstrip design as well as microstrip-to-substrate integrated waveguide transitions are discussed.

2.7.1 Microstrip Design

Microstrip is composed of a thin metal conductor on top of a dielectric substrate. The bottom of the substrate is coated with metal to act as a ground plane. Figure 2.19 (a) depicts a perspective view of a microstrip line where W is the conductor width, t conductor thickness, h is the substrate height, and ϵ_r is the dielectric constant. Due to the geometry of microstrip, the electromagnetic field extends into two media; part of the field is confined within the substrate, and part of the field flows though the air. The arrangement of the microstrip can not maintain a pure TEM mode, but if the conductor and the ground plane are close enough together ($h \ll \lambda$), the fields will propagate similar to that of the TEM mode; this condition can be considered *quasi-TEM* [28, 59]. The inhomogeneous regions around a microstrip conductor are illustrated in Figure 2.19 (b) where the electric (E) and magnetic (H) fields are extended into both media.

To quantify the quasi-TEM mode, a homogeneous medium is considered around the microstip conductors. The new medium is considered to have an effective dielectric

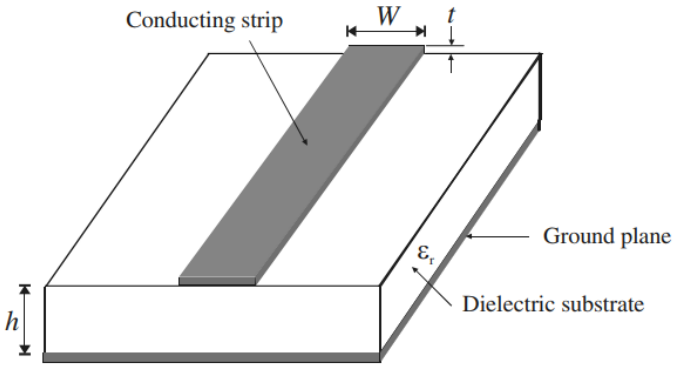

(a)

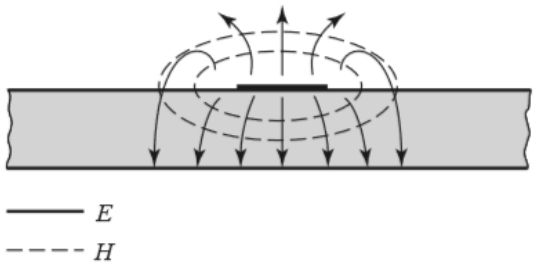

(b)

Figure 2.19: (a) Microstrip geometry [59] (b) Electric and magnetic field lines in microstrip [28].

constant ε_e which can be found using Equation 2.9 from [28]. Figure 2.20 depicts the replacement of the inhomogeneous substrate/air model with that of the homogeneous medium. With given dimensions for W and h, the characteristic impedance Z_0 can be found using equation 2.10 from [28, 59].

$$\varepsilon_e = \frac{\varepsilon_r + 1}{2} + \frac{\varepsilon_r - 1}{2}\left(\frac{1}{\sqrt{1 + 12h/W}}\right) \tag{2.9}$$

$$Z_0 = \begin{cases} \frac{60}{\sqrt{\varepsilon_e}} ln\left(\frac{8h}{W} + \frac{W}{4h}\right) & for \quad W/h \leq 1 \\ \\ \frac{120\pi}{\sqrt{\varepsilon_e}[W/h + 1.393 + 0.667\, ln(W/h + 1.444)]} & for \quad W/h \geq 1 \end{cases} \tag{2.10}$$

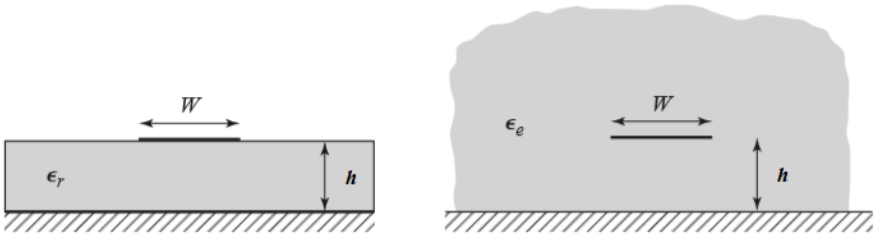

Figure 2.20: Microstrip geometry surrounded by its inhomogeneous medium (left) and the equivalent geometry surrounded by a homogeneous medium defined by the effective dielectric constant (right). Modified from [28].

2.7.2 Microstrip to SIW Design

Due to the wide use of microstrip circuits, transitions between microstrip lines and other planar technologies have been an important research topic. In order to interface microstrip lines with rectangular waveguides or (in this case) substrate integrated waveguides, tapered transitions are proposed due to their ability to maintain important electrical characteristics such as bandwidth and insertion loss [60–62]. Figure 2.21 depicts a typical microstip-to-substrate integrated waveguide transition.

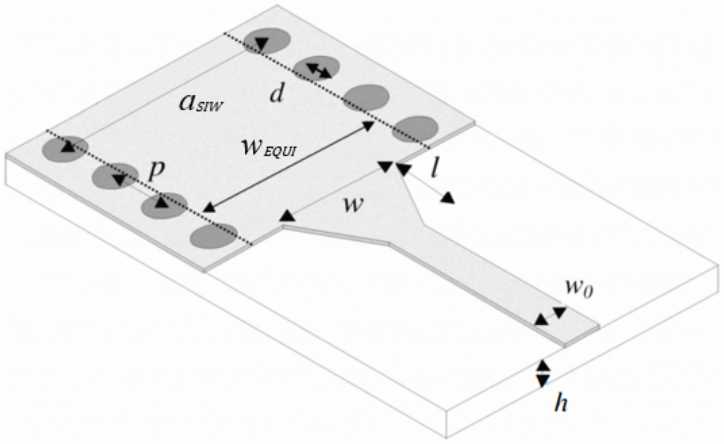

Figure 2.21: Geometry of a microstrip-to-SIW transition. Modified from [60].

As part of the initial design, a comparison can made between the electric fields of a TE_{10} mode rectangular waveguide and the quasi-TEM mode of a microstrip line - see Figure 2.22. The interconnection of the microstrip and waveguide requires matching of both the step transition and the tapered line section. The equivalent waveguide structures are analyzed in [60] and are depicted in Figure 2.23 where the dielectric material (ε_e) in the waveguide is equal to the effective dielectric constant found from

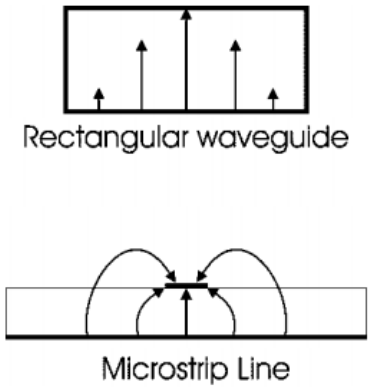

Figure 2.22: Comparison of electric field lines in rectangular waveguide and microstrip line. Modified from [61].

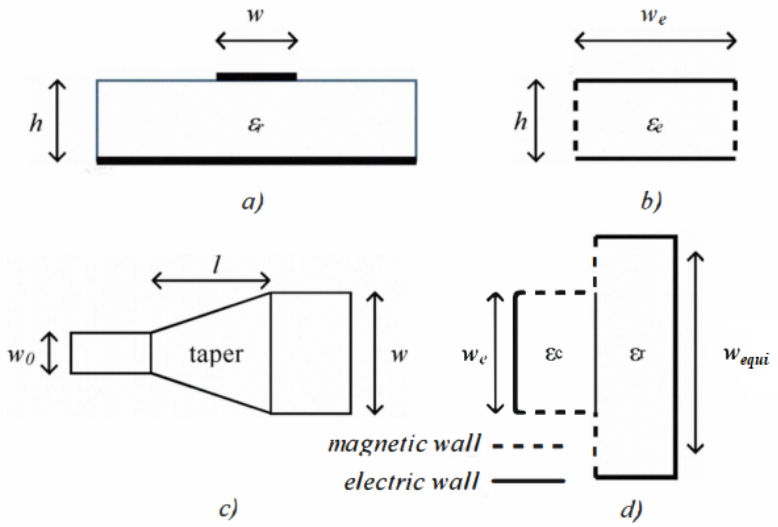

Figure 2.23: Equivalent topology for microstrip-to-SIW: a) Microstrip line, b) waveguide equivalent of microstrip line, c) microstrip taper, d) microstrip-to-SIW step. Modified from [60].

Equation 2.9. The waveguide impedance is found using Equation 2.11, where w_e is the waveguide equivalent width of the microstrip line. In order to find the matching impedance for the microstrip line, the two previous equations are set equal to each other, as shown in Equation 2.12.

$$Z_e = \sqrt{\frac{\mu}{\varepsilon_o \varepsilon_r}} \frac{h}{w_e} \tag{2.11}$$

$$Z_e = \sqrt{\frac{\mu}{\varepsilon_o \varepsilon_r}} \frac{h}{w_e} = \begin{cases} \frac{60}{\sqrt{\varepsilon_e}} ln\left(\frac{8h}{w} + \frac{w}{4h}\right) & for \quad w/h \leq 1 \\ \frac{120\pi}{\sqrt{\varepsilon_e}[w/h + 1.393 + 0.667\, ln(w/h + 1.444)]} & for \quad w/h \geq 1 \end{cases} \tag{2.12}$$

The model of the step is detailed in Figure 2.23 (d). We can see that the scattering parameters are independent of height, but are dependent on the ratios of w_{equi}/w_e and $\varepsilon_e/\varepsilon_r$. The final equations determined by [60] are shown in (2.13) and (2.14). By equating these two formulas, the optimal taper width w can be found for a given height h, dielectric constant ε_r, and equivalent width w_{equi}.

$$\frac{1}{w_e} = \begin{cases} \frac{60}{\eta\, h} ln\left(\frac{8h}{w} + \frac{w}{4h}\right) & for \quad w/h \leq 1 \\ \frac{120\pi}{\eta\, h\, [w/h + 1.393 + 0.667\, ln(w/h + 1.444)]} & for \quad w/h \geq 1 \end{cases} \tag{2.13}$$

$$\frac{1}{w_e} = \frac{4.38}{w_{equi}}\, e^{-0.627 \frac{\varepsilon_r}{\frac{\varepsilon_r + 1}{2} + \frac{\varepsilon_r - 1}{2}\left(\frac{1}{1 + 12h/w}\right)}} \tag{2.14}$$

Chapter 3

Design Process and Performance Analysis

For this work, a dual-layer substrate-integrated beamforming network is developed based on an 8x8 cross-configuration Butler matrix. To arrive at the final design, the theories explored in Chapter 2 are used to develop the individual components that make-up the entire system. This chapter first describes the design process and simulated performance of the individual components, then details the operation of the 8x8 Butler matrix and beamforming network as a sum of these components. By the end of this chapter, the system is demonstrated for operation as an interchangable 1-dimension and 2-dimension beamforming network between 28.5 and 31.5 GHz. When each of the arrays are combined with the Butler matrix, 8 individually switched beams are produced with predetermined directions based on phase progressions at the output ports.

The design and simulation work is conducted in the commercially available Microwave Studio software by Computer Simulation Technology (CST). Each of the components are optimized for performance needs based on the initial design conditions that are described in Chapter 2. These performance needs are generally based on transmission, isolation, return loss, and phase error. Figures and tables outline the dimensions of each component. For all of the designs, the dielectric substrate is based on the Rogers RT/Duroid 5880 with $\varepsilon_r = 2.2$, $\tan\delta = 0.0009$ and height $h = 0.508$ mm. The copper metallization has a thickness $t = 0.035$ mm, and conductivity $\sigma = 5.8\text{x}10^7$ S/m

3.1 Design of Individual Components

As previously mentioned, this section outlines the design process of each of the individual components in the system based on the theory and calculations explained in Chapter 2. The figures and tables outline the metric dimensions (mm), while simulation results are presented to demonstrate the characteristics of the components. Each of the structures has been optimized for performance from the initial design guide-

lines; trade-offs between characteristics such as phase error, bandwidth, and return loss are discussed where permitted. Unless noted otherwise, each of the components has been fed by equivalent dielectric waveguide ports for simulation purposes.

3.1.1 Design of SIW Lines

For the design of the substrate integrated waveguide, theory and calculations discussed in Section 2.1 are used to derive the structure parameters based on the geometry of Figure 2.1(b). Table 3.1 presents the parameter values of the structure based on Equations 2.1-2.3. Figure 3.1 again depicts the perspective view of the substrate integrated waveguide with its corresponding geometry and equivalent waveguide width. Studying Figure 3.2, we can see that the structure has a return loss that is better than 50 dB over the band of interest (28.5–31.5 GHz), and that the ripple behavior depends on the length of the structure. Unless specified, the basic dimensions of Table 3.1 are used for the substrate integrated components throughout this thesis, and the cutoff frequency used in Equations (2.2) and (2.3) is approximately 21.1 GHz.

Structural Parameters	**Dimensions (mm)**
d	0.300
p	0.560
h	0.508
w_{equi}	4.795
a_{SIW}	5.000

Table 3.1: Parameter values of SIW geometry.

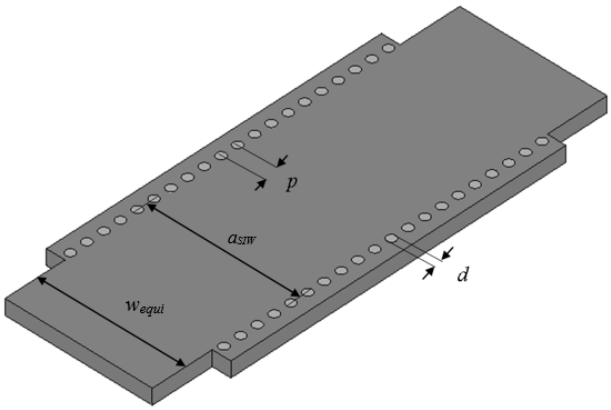

Figure 3.1: Equivalent dielectric-filled waveguide and SIW geometry. Metallization layers not shown.

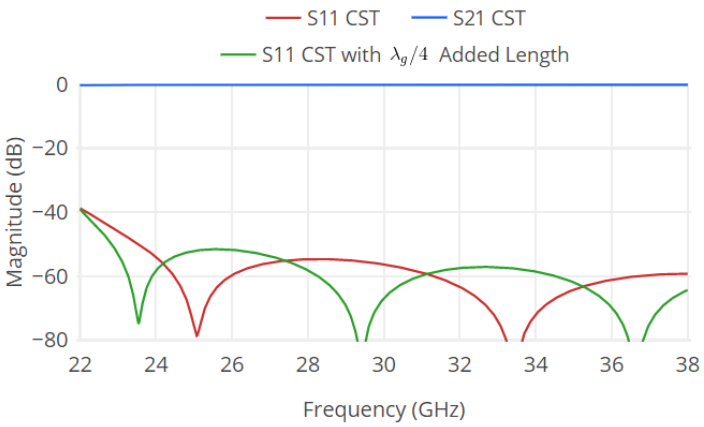

Figure 3.2: S-parameters of SIW line.

3.1.2 Design of H-Plane Coupler Components

The H-plane couplers are designed using the initial design conditions of a Riblet slot type coupler from Section 2.2 and Equation 2.4. First, the quadrature hybrid coupler is designed and optimized for operation, then the cross-over coupler is designed by setting two of the hybrid couplers back-to-back, then optimizing the center vias.

The goal of the hybrid coupler is two fold: First, divide the power equally (-3 dB) between ports 2 and 3 (Through and Coupled), while port 4 remains isolated. Second, maintain a 90 degree phase shift between the signals at port 2 and 3 over the bandwidth of interest. Table 3.2 presents the parameter values, while Figure 3.3 illustrates the dimensions of the hybrid coupler from a top view. Reviewing the S-parameter results in Figure 3.4, it can be shown that for S_{21} and S_{31}, the hybrid coupler is able to split the output power around -3 dB while maintaining approximately 90 degree phase difference over the band of interest. The maximum phase error which can be seen at 31.5 GHz, is less than 0.5 degrees. The return loss and isolation are better than 20 dB over the frequency band and reach approximately 35 dB at 30 GHz. Due to symmetry, results for the other ports are similar to that of Figure 3.4

To create the cross-over coupler, two of the hybrid couplers discussed above are set back-to-back while the length of vias between them are adjusted for optimal conditions. The parameters shown in Table 3.3 define the position of the new via holes. The geometry detailed in Table 3.3 and Figure 3.5 result in the S-parameter simulations that are depicted in Figure 3.6. The simulated results demonstrate the transmission of the signal from port 1 to port 3 (across diagonal), while ports 2 and 4 are isolated. The return loss and isolation are better than approximately 20 dB for the full band of interest. Due to symmetry of the component, the input signal can be transferred from one port to its cross-diagonal port and visa-versa, making it an

Structural Parameters	Dimensions (mm)
l_1	1.120
l_2	2.800
L_c	6.160
w_1	0.800
w_2	0.450
a_{SIW}	5.000

Table 3.2: Parameter values of hybrid coupler geometry.

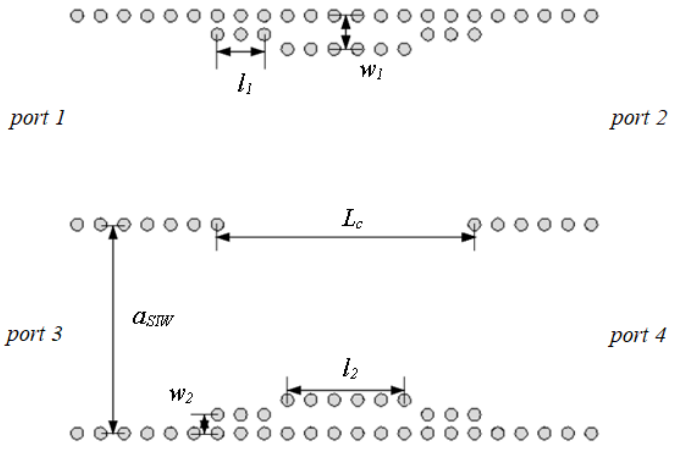

Figure 3.3: Hybrid coupler geometry (top view).

important junction for directing signal flow. Simulation results for the other ports are similar to that of Figure 3.6

Structural Parameters	Dimensions (mm)
l_3	3.360
w_3	5.000

Table 3.3: Additional parameter values for cross-over coupler geometry.

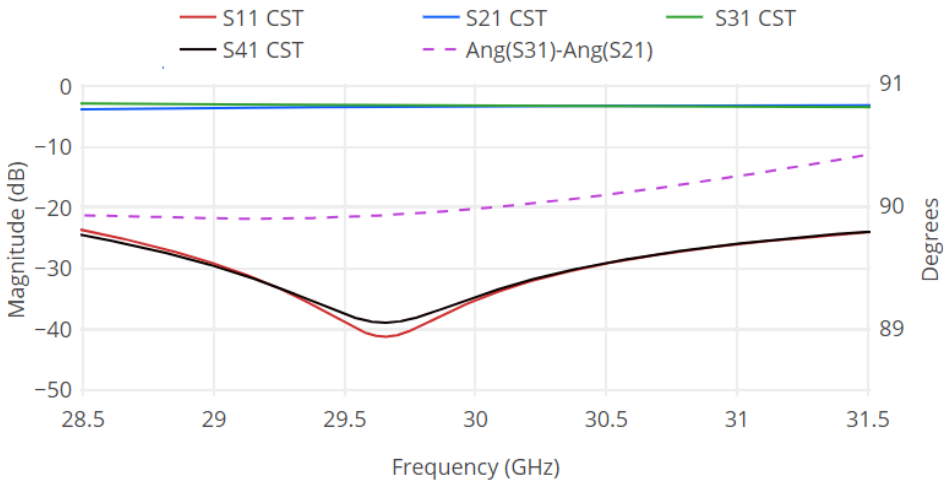

Figure 3.4: S-parameters and phase difference of hybrid coupler.

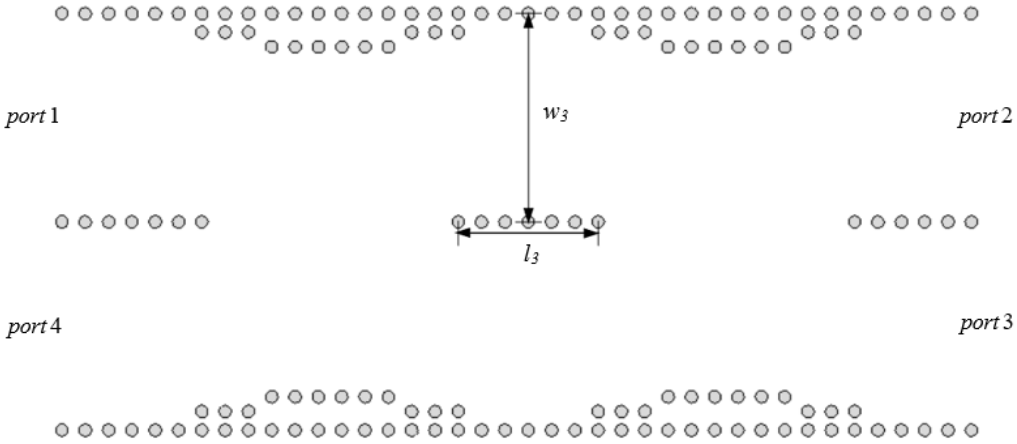

Figure 3.5: Cross-over coupler geometry; two hybrid couplers placed back-to-back (top view).

3.1.3 Design of Slot Radiator Components

The design process for the slot radiators follow the modal field and surface current principles discussed in Section 2.3. For each of the antennas, the width of the substrate integrated waveguide feed line is equal to a_{SIW} as calculated in Section 3.1.1. It is also important to note here that the parameters of the slot antennas have a detrimental impact on the physical layout, S-parameters, and beam-lobe geometry when combined as an array; this impact is taken into account, as these designs will be used in arrays.

Reviewing the geometry proposed in Figure 2.10, a staggered dual slot antenna configuration can be created. For the case of substrate integrated waveguide, the short circuit at the end of the antenna is created by setting a row of vias across the width.

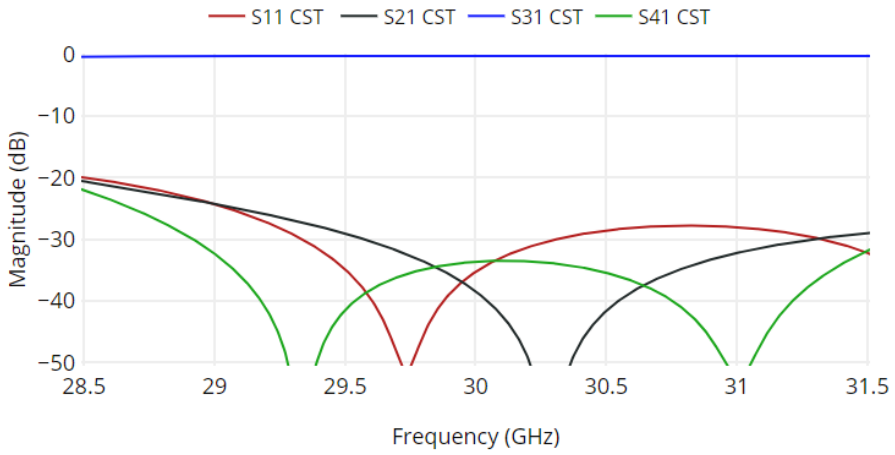

Figure 3.6: S-parameters of cross-over coupler.

The first slot in this case is not set $\lambda_g/4$ wavelength back from the waveguide short, but $3\lambda_g/4$. By positioning the first slot in this manner, the phasing of the slots is respected but offset by 180 degrees. The second slot is then positioned approximately $\lambda_g/2$ from the first. The slots are staggered across the center line and cut into the metallization layer. Table 3.4 and Figure 3.7 detail the geometric features of the slot antenna after optimization. Each slot is 0.55 mm wide. Figure 3.8 depicts the reflection coefficient over 28.5 - 31.5 GHz; a return loss better than 10 dB can be observed over the full bandwidth and reaches approximately 11.9 dB at 30 GHz.

Structural Parameters	**Dimensions (mm)**
l_{1A}	4.400
l_{1B}	4.200
w_{1A}	0.325
w_{1B}	0.375
s_{1A}	4.900
s_{1B}	7.010

Table 3.4: Parameter values of staggered slot antenna geometry.

Different from that of the staggered slot antenna, the single center-slot antenna requires a special via along the path of the waveguide to alter the surface current distribution. If the via is not in the correct place, the slot will not radiate. Upon reviewing Figure 2.12 from Section 2.3.2, a slot can be positioned $\lambda_g/4$ from the end of the waveguide short. Again, the short is created from a row of vias across the width of the substrate integrated waveguide line. The slot is cut into the metallization layer 0.65 mm wide and centered. Table 3.5 and Figure 3.9 portray the geometric

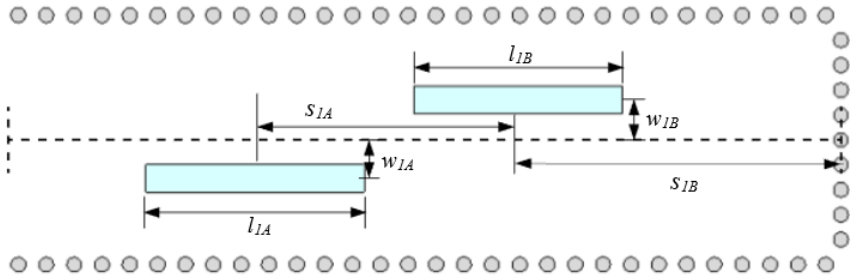

Figure 3.7: Staggered slot antenna geometry (top view).

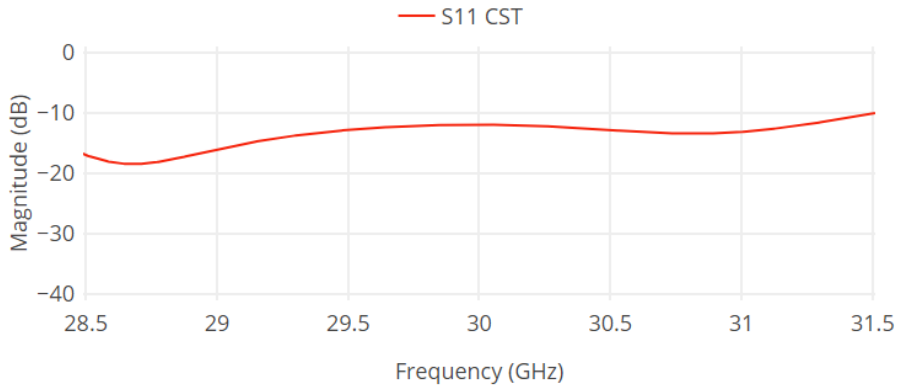

Figure 3.8: Reflection coefficient of staggered slot antenna.

parameters of the antenna and the via hole position after optimization. Figure 3.10 depicts the reflection coefficient results over 28.5 - 31.5 GHz; a return loss better than 10 dB can be observed over 28.5 - 31.25 GHz and reaches approximately 14.8 dB at 30 GHz. The return loss is lower than 10 dB at the higher end of the spectrum, but as mentioned previously, the parameters and physical layout of the array structure have been taken into account for future implementation; the return loss, isolation, and beam-lobe geometry of the full array structure will be revisited in Section 3.2.2.

Structural Parameters	**Dimensions (mm)**
l_{2A}	5.100
s_2	2.900
d_{2A}	3.560
d_{2B}	1.000
d_{2C}	0.300

Table 3.5: Parameter values of staggered slot antenna geometry.

Figure 3.9: Center-slot antenna geometry (top view).

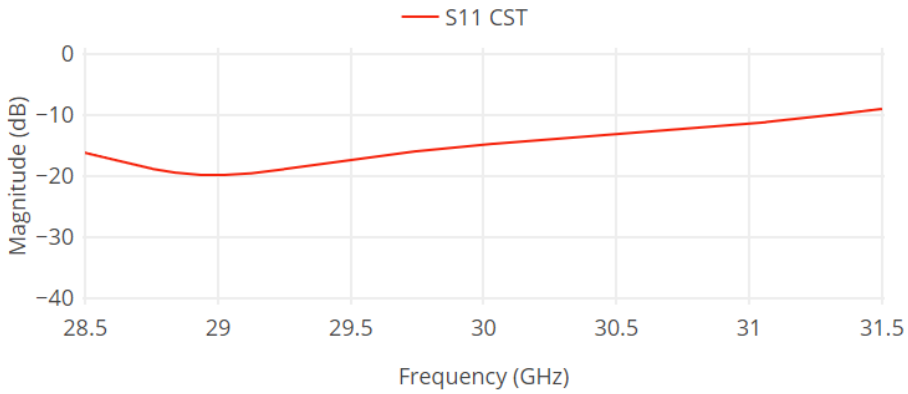

Figure 3.10: Reflection coefficient of center-slot antenna.

3.1.4 Design of Multilayer Transition Components

Several different E-plane layer-to-layer transitions are available for use as previously discussed. The folded passband filter is a unique option for this project for several reasons: First, it has the ability to change the signal flow direction by 180 degrees in an E-plane fashion. Second, it provides a filtering element that can be tuned according to specific use, and finally, it can serve as detachment point for mounting or changing arrays fabricated in the top layer. To produce the folded direct-coupled passband filter transition, two substrate integrated waveguide layers are created with the same geometry and stacked vertically. A horizontal slot is cut in each of the layers where resonators 2 and 3 are positioned. Due to manufacturing process, the stacking of the layers create a thicker metallization layer (0.070 mm, rather then 0.035 mm) and must be accounted for during simulation.

For a perspective reference, Figure 2.15 demonstrates the layout of the folded direct coupled filter in rectangular waveguide. Table 3.6 and Figure 3.11 illustrate the dimensions in the center of the filter. The S-parameters of the filter are demonstrated in Figure 3.12; the return loss is better than 20 dB over a range greater than 26 - 34

GHz, and allows transmission of the full frequency band of interest (depicted by the crosshatched section). This transition successfully operates as a passband filter while directing the signal from one layer to the next.

Several comments can be made about the filtering aspect; although the passband is set for a wide range in this example, creative passband tuning can be applied for more specific instances or applications. Additionally, more dramatic effects such as transmission zeros can be added to the design through the use of cross-coupled resonators. Although both of these aspects are of interest and fully applicable, they are out of the scope of this thesis at this time. As demonstrated later in this thesis, the physical location of the filters will also offer an advantage over other transitions; filtering of the signal is incorporated after the antenna array, but before reaching the Butler matrix network.

Structural Parameters	**Dimensions (mm)**
l_3	0.700
w_{3A}	2.000
w_{3B}	1.6500
w_{3C}	4.100
s_3	0.860
d_{3A}	3.180
d_{3B}	3.190
d_{3C}	0.300

Table 3.6: Parameter values of the folded direct coupled passband filter geometry.

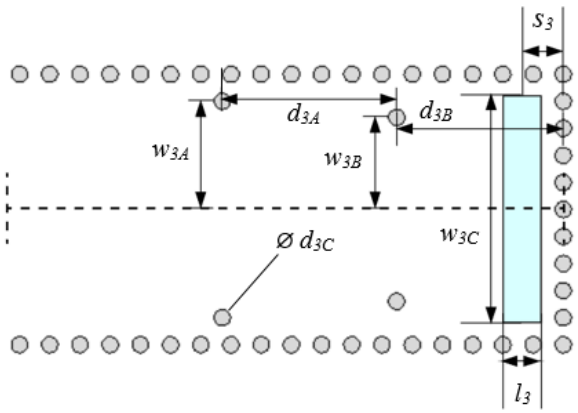

Figure 3.11: Folded direct coupled passband filter geometry (center layer, top view).

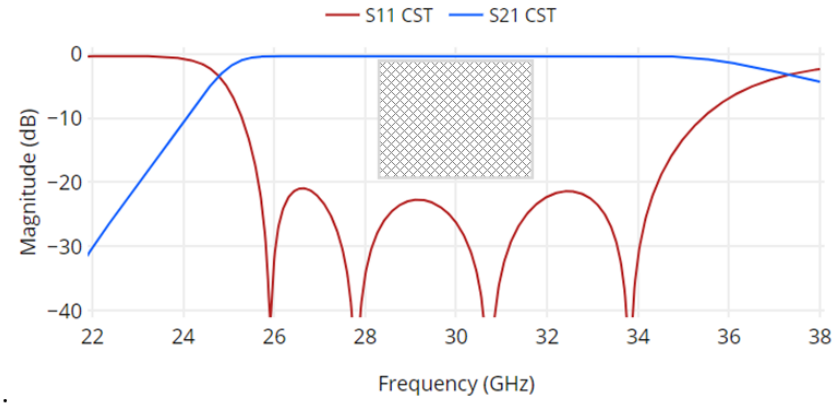

Figure 3.12: S-parameters of the folded direct-coupled passband filter. Crosshatched inset depicts system operating frequencies.

3.1.5 Design of Phase Shifter Lines

Two types of phase shifters (delay line and equal-length, unequal-width) are used in this project. Multiple variations are used and combined to tune the phase of the final network. In this section, a simple example of the equal length, unequal width phase shifter is given to exhibit its effect, followed by a demonstration of one of the phase shifters of the Butler matrix with respect to its corresponding cross-over coupler.

For the first example, an equal-length, unequal-width phase shifter is created by modifying the via hole locations along a substrate integrated waveguide line. Table 3.7 and Figure 3.13 depict the example geometry of the equal-length, unequal-width phase shifter between two transmission lines which are defined by Port 1 to Port 2, and Port 3 to Port 4. It can be noted that the variation of phase is more dramatic due the displacement of the common side wall effecting both lines; the side wall of a single line could have been varied and compared with respect to its original phase. Figure 3.14 portrays the transmission, reflection coefficient, and phase difference of the lines. The return loss is better than 20 dB over the frequency band of interest for both lines. The phase difference between the output ports is approximately 15 degrees with less than ±2 degrees error in the lower and higher frequencies.

Structural Parameters	**Dimensions (mm)**
l_4	2.800
w_4	0.285

Table 3.7: Parameter values of equal-length, unequal-width phase shifter geometry.

For implementation of the phase shifters in the Butler matrix scheme, *phase compensation* is taken into account to decrease phase imbalance; this is done by developing

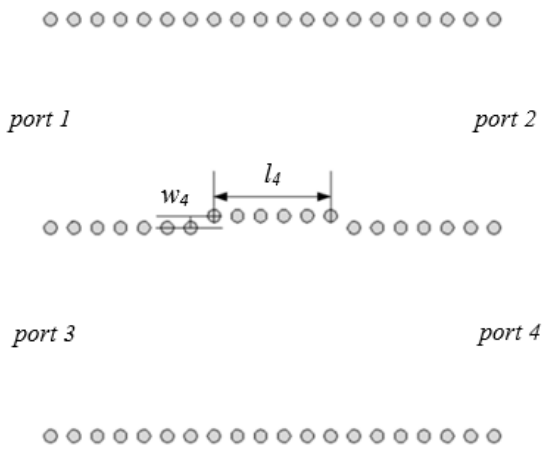

Figure 3.13: Equal-length, unequal-width phase shifter geometry (top view).

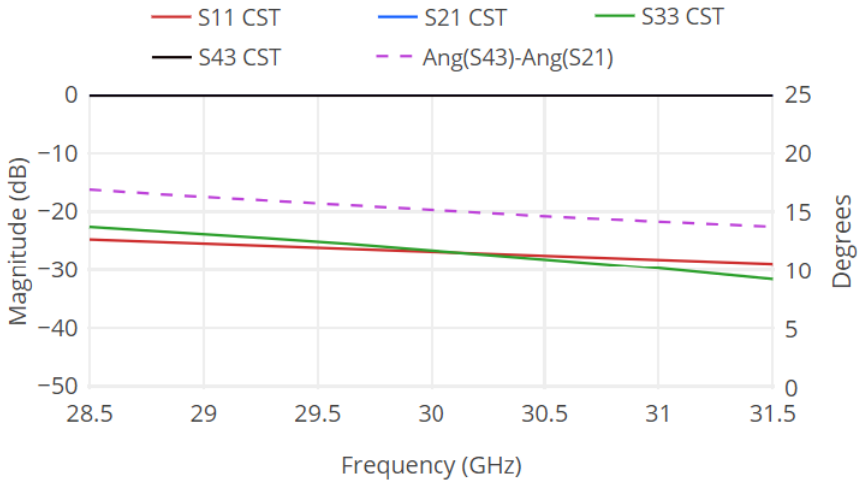

Figure 3.14: S-parameters and phase difference of equal-length, unequal-width phase shifter.

the phase shifter with reference to specific locations. In the case of the 8x8 Butler matrix discussed in Section 2.6 and Figure 2.18 for example, the -67.5 degree phase shifter value is taken with respect to its parallel cross-over coupler. This method effectively compensates for phase shift caused by the cross-over coupler since in practice it is a non-ideal component. Table 3.8 and Figure 3.15 depict the dimensions and layout of the -67.5 degree phase shifter. Figure 3.16 illustrates the transmission and reflection coefficient of the phase shifter, as well as the phase with respect to the cross-over coupler developed in Section 3.1.2. The return loss of the phase shifter is better than 20 dB over the full spectrum. Between 28.5 and 30.5 GHz, the phase is close to -67.5 degrees (within 2 degrees) and rises to approximately -75 degrees at 31.5 GHz.

Structural Parameters	Dimensions (mm)
l_{5A}	2.240
l_{5B}	6.160
l_{5C}	2.240
w_{5A}	1.700
w_{5B}	3.000
w_{5C}	1.200
d_5	0.400

Table 3.8: Parameter values of -67.5 degree phase shifter.

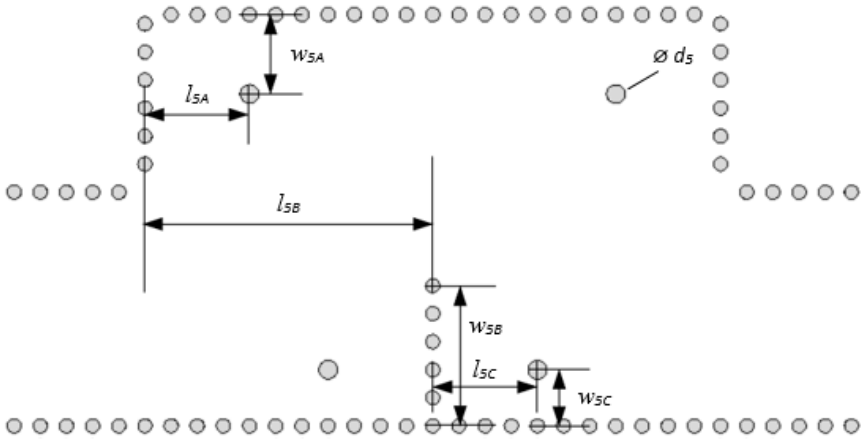

Figure 3.15: -67.5 degree phase shifter geometry.

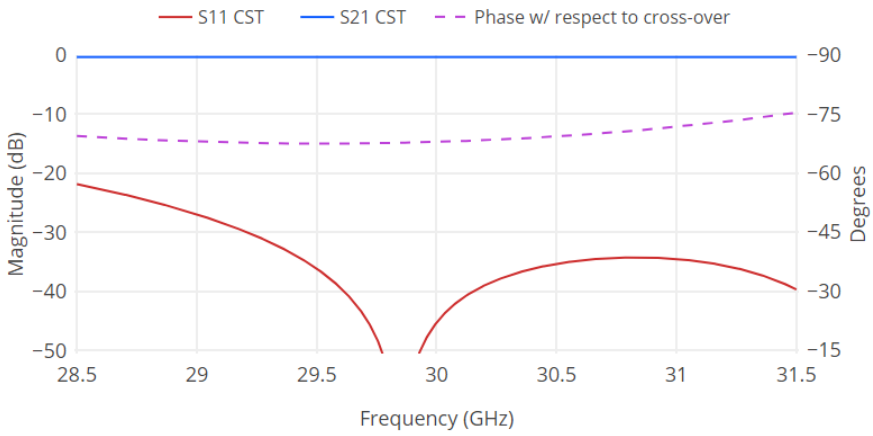

Figure 3.16: S-parameters and phase of -67.5 degree phase shifter.

3.1.6 Design of Microstrip-to-SIW Transitions

The use of microstrip transitions provide a low-cost, planar method of integrating substrate integrated waveguides into microstrip circuits. The microstrip line and the taper transition is designed in this section. To demonstrate operation, a simple circuit is simulated and the S-parameters and the E-field distribution are exhibited for a more dynamic view. The initial design is discussed in Section 2.7.1 and 2.7.2. For the first part of the design, Equations 2.9 and 2.10 are used to define the width of a 50Ω impedance microstrip line. The initial microstrip design parameters are equivalent to that of the substrate integrated waveguide's height, metallization thickness, and dielectric constant. The initial conditions for the tapered microstrip section is defined by solving Equations 2.11-2.14. In order to improve the return loss, the taper dimensions are optimized. The dimensions and geometry of the regular microstrip line and the taper transition are shown in Table 3.9 and Figure 3.17. After optimization of the initial design, the return loss and transmission values are simulated when two transitions are set back-to-back (microstrip-SIW-microstrip). The circuit is fed with microstrip ports in CST; the S-parameters are depicted in Figure 3.18, and a top view of the circuit's E-field distribution is demonstrated in Figure 3.19. The circuit has a return loss of better than 33 dB over 28.5 to 31.5 GHz.

Structural Parameters	**Dimensions (mm)**
l_6	0.848438
w_6	2.540
w_{6o}	1.580
a_{SIW}	5.000

Table 3.9: Parameter values of microstrip-to-SIW transition.

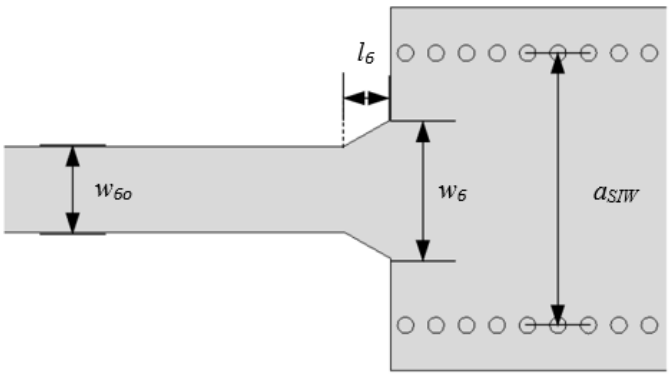

Figure 3.17: Microstrip-to-SIW transition geometry (top metallization view).

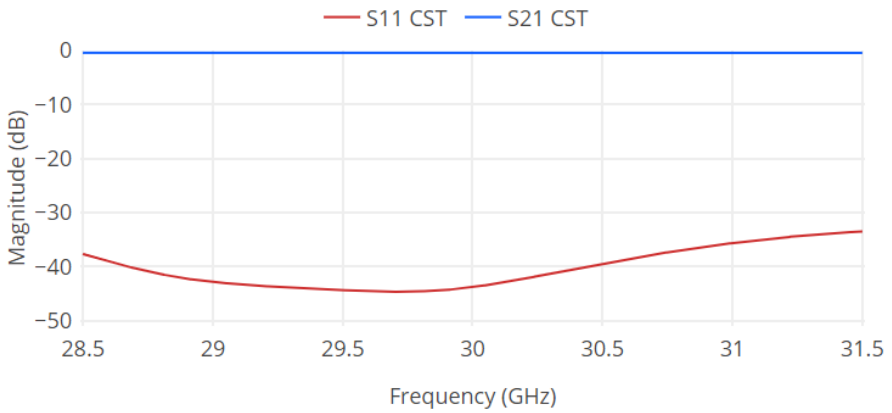

Figure 3.18: S-parameters of back-to-back microstrip-to-SIW transition.

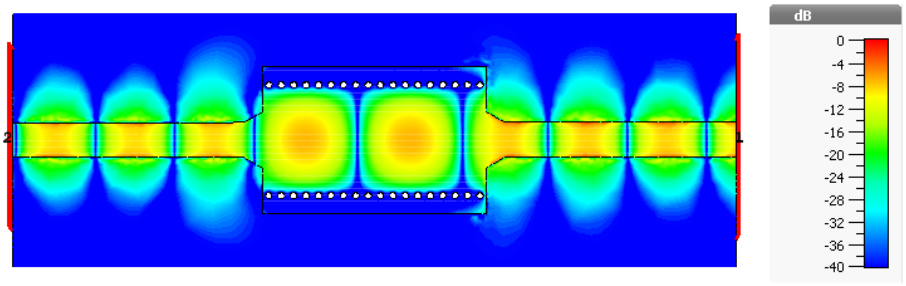

Figure 3.19: E-field of back-to-back microstrip-to-SIW transition (top view).

3.2 Assembly of Individual Components as a System

To design the beamforming network as a whole, the components outlined in Section 3.1 are used to create two individual layers of the system. The first (bottom) layer forms the 8x8 cross-configured Butler matrix; the design layout and basic operation is reviewed followed by a presentation of the simulated results. The second (top) layer forms the broadside antenna array structure. Two different antenna structures are created for demonstration as interchangeable 1-dimensional and 2-dimensional arrays. The designs of each are discussed, followed by a presentation of the simulated S-parameters and the corresponding beam patterns.

In the final subsection, the bottom Butler matrix layer and one of the top antenna array layers are combined as a full beamforming network; the network is demonstrated as a 1-dimensional system. The system is then reconfigured using the second antenna array which is demonstrated as a 2-dimensional system. The S-parameters and beam plots of each of the examples is illustrated and discussed in depth.

3.2.1 Design of the 8x8 Butler Matrix

For this thesis, an 8x8 Butler matrix is selected as the feed network to the antenna array. Butler matrices have been presented as a powerful method for passive beamforming, but unlike the ideal schematic version, real-world applications introduce problems such as insertion loss and reflections, as well as substantial physical dimensions that cannot be ignored. One factor adding to this dilemma is the number of cross-over couplers throughout the matrix. Many attempts have been made in order to address the issue of cross-over couplers, all with the goal of mitigating losses as well as reducing the physical size – References [6–10] illustrate several notable applications that address the issues as well as have influenced this work.

An ideal Butler matrix scheme is illustrated in Figure 3.20; the design utilizes 12 quadrature hybrid couplers, 16 cross-over couplers, and 8 phase shifters. The phase shifters ϕ_1, ϕ_2, and ϕ_3 correspond to -67.5, -22.5, and +45 degrees, respectively. An attempt at reforming this matrix with the goal of reducing the number of cross-over couplers is made in Figure 3.21 and similar to that of [9, 10]. In this configuration, the Butler matrix operates as intended but with the amount of cross-over couplers reduced to 6 and ϕ_3 modified to be a -45 degree phase shifter. It is worth noting that in the typical Butler matrix version shown in Figure 3.20, outputs 9 through 16 can terminate sequentially as well as in close enough proximity that the antennas of the array can coincide with the desirable $\lambda/2$ spacing. In the cross-configured Butler matrix of Figure 3.21, output ports 9 through 16 are not terminated sequentially and have far greater than $\lambda/2$ spacing between elements. The implications of non-sequential and widely-spaced output ports will be addressed in Section 3.2.2, but for now, the goal will be to demonstrate the cross-configured Butler matrix operation in substrate integrated waveguide technology.

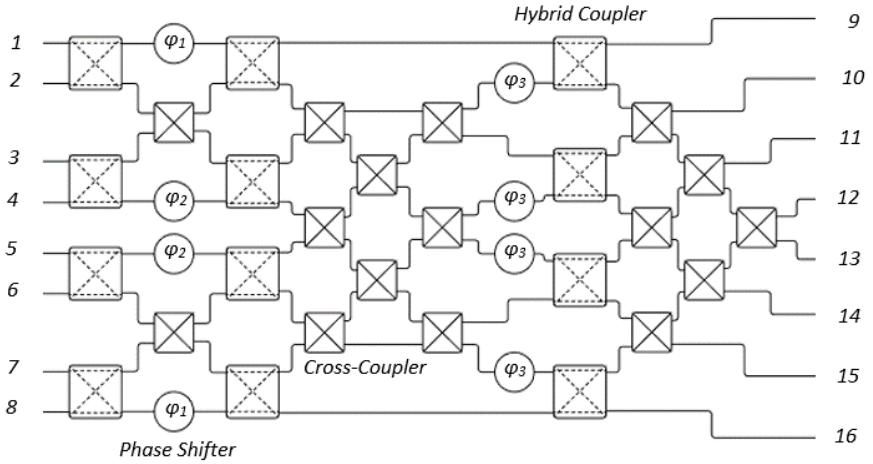

Figure 3.20: Ideal 8x8 Butler matrix.

With the Butler matrix modified into the cross-configuration shown in Figure 3.21, several considerations must be taken into account. These considerations relate

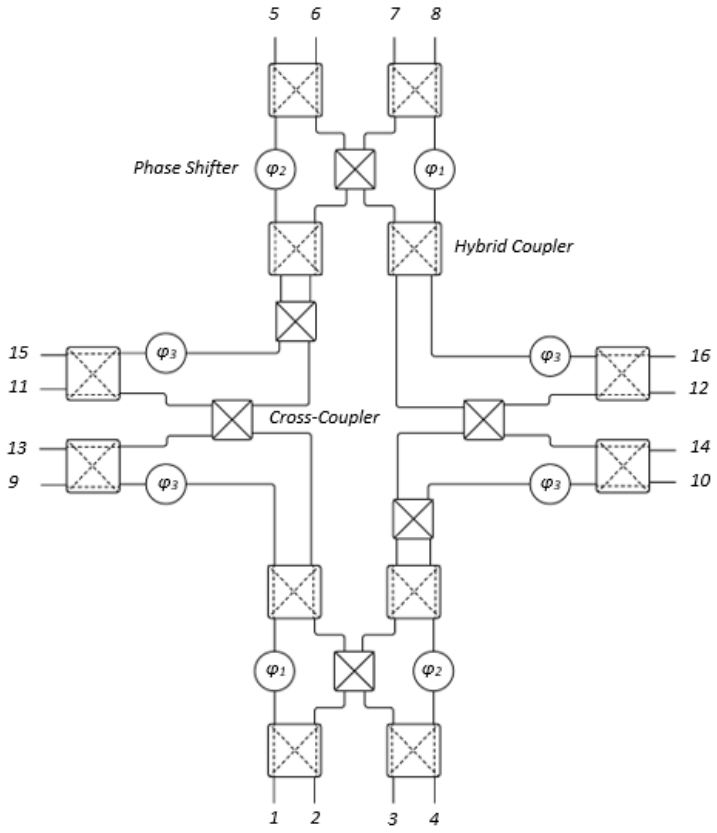

Figure 3.21: Ideal cross-configured 8x8 Butler matrix.

to a change in the length of the waveguide feed paths between individual components, which in turn modifies where the -45 degree phase shifter reference points are taken from. This dilemma stems from the phase of the cross-overs combined with the 90 degree corners in the waveguide feed paths that distribute to corresponding outputs. The addition of the 90 degree corners modifies the physical length of waveguide with a non-negligible phase value that must be compensated for proper operation. The phase compensation can be understood by observing Figure 3.22 and Figure 3.23 which illustrate the final cross-configuration scheme. The waveguide paths are modified by observing the longest physical path for a selected input. For example, the path from input port 1 to output port 16 is the longest path when compared to input port 1 and output ports 9 through 15. Therefore, each sequential output path must adhere to the final phase value developed by path 1 to 16. Using the phase developed from path 1 to 16 as a reference, the next sequentially decreasing output port (15) must have a phase progression of 22.5 degrees with respect to port 16. To achieve this, compensating phase shifter ϕ_a is added and operates as a 0 degree phase shifter. In this manner, the electrical length of the second cross-over coupler in path 1 to 16 is compensated. The next 22.5 degree phase progression of output (14) is realized though tuning of the respective phase shifter ϕ_3. The phase shifter compensates the additional line length

caused by a difference in the feed paths of the 90 degree corner sections, cross-over couplers and addition of ϕ_a. Following the pattern of 22.5 degree phase progressions between each consecutive output port and tuning each phase shifter (ϕ_3) to maintain the proper phase relations, the final matrix design is rendered in substrate integrated waveguide as shown in Figure 3.23.

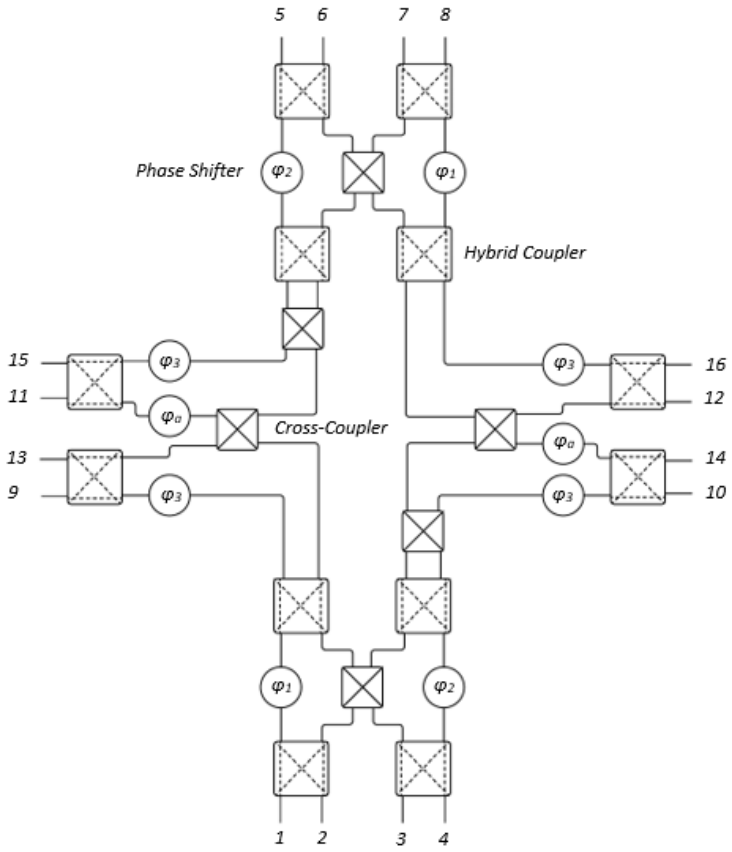

Figure 3.22: Cross-configured 8x8 Butler matrix with compensating phase shifters.

Using dielectric waveguide ports for excitation of the structure shown in Figure 3.23, the simulated results for reflection coefficient, transmission, isolation, and phase distribution are recorded. Figure 3.24 through Figure 3.27 demonstrate the reflection coefficient, transmission and isolation of ports 1 through 4, while Figures 3.28 through Figure 3.31 demonstrate the phase distribution at the output ports when ports 1 through 4 are excited. Not shown are the results of exciting ports 5 through 8, but due to the symmetry of structure, the reflection coefficient, transmission, isolation and phase distribution are of similar form. The return loss for each port is better than 20 dB for almost the entire frequency region. Ideally, the coupled power would have equal power division at the outputs of -9 dB, but due to losses, they are closer to the -10.5 dB level and spread over frequency. The phase distributions converge close to their respective phase references at 30 GHz, and deviate as they move further

away from the center frequency.

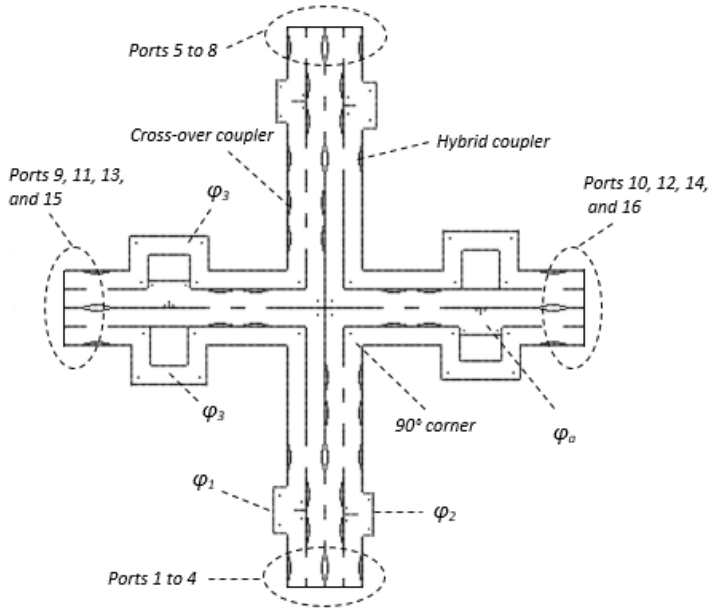

Figure 3.23: 8x8 cross-configured Butler Matrix in SIW.

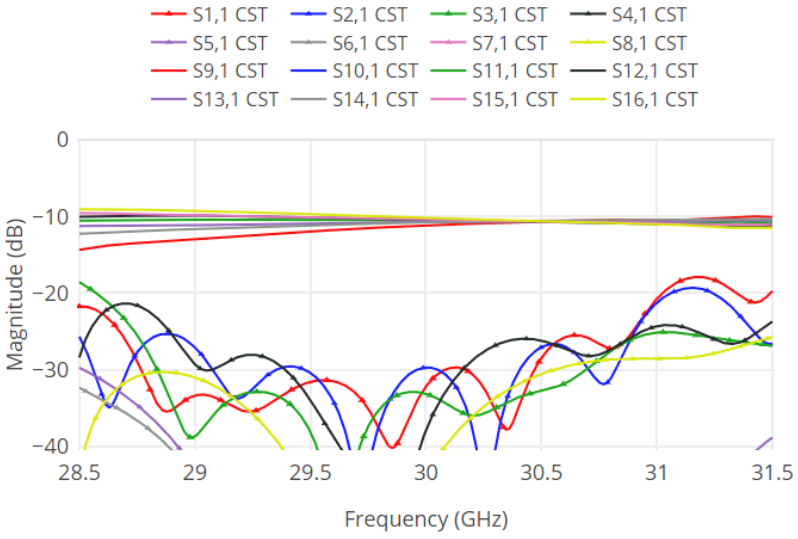

Figure 3.24: Simulated S-parameters of cross-configured Butler matrix; Port 1 excited.

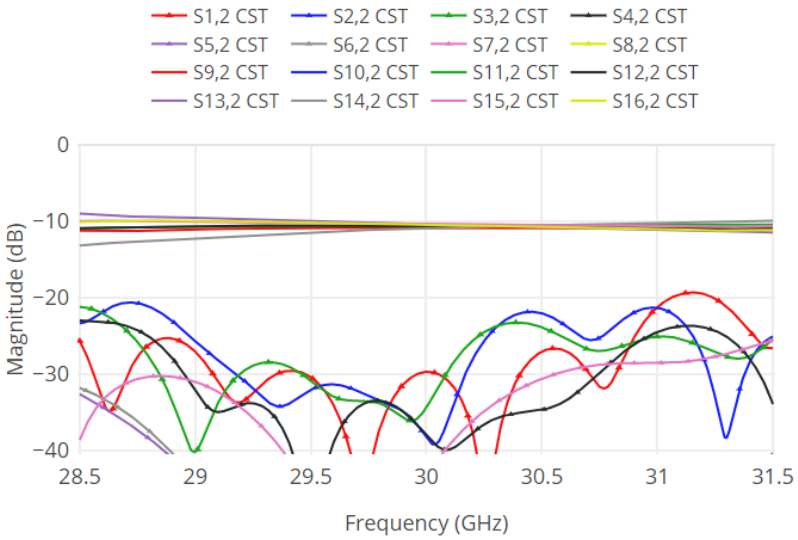

Figure 3.25: Simulated S-parameters of cross-configured Butler matrix; Port 2 excited.

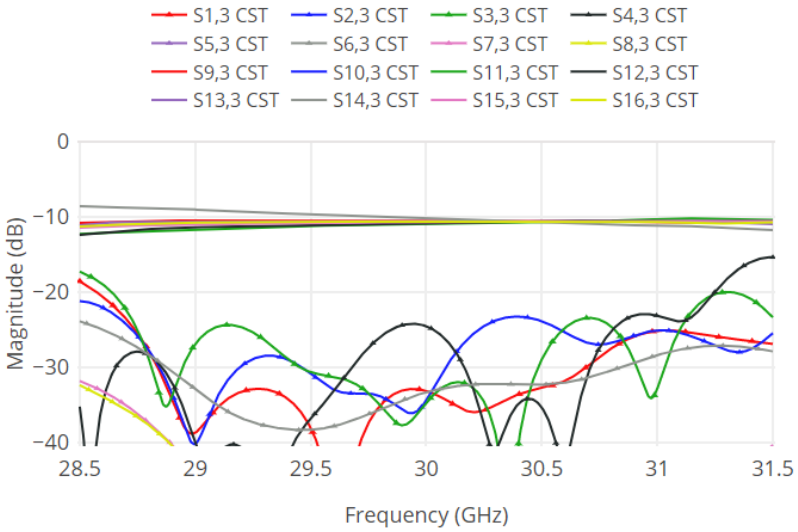

Figure 3.26: Simulated S-parameters of cross-configured Butler matrix; Port 3 excited.

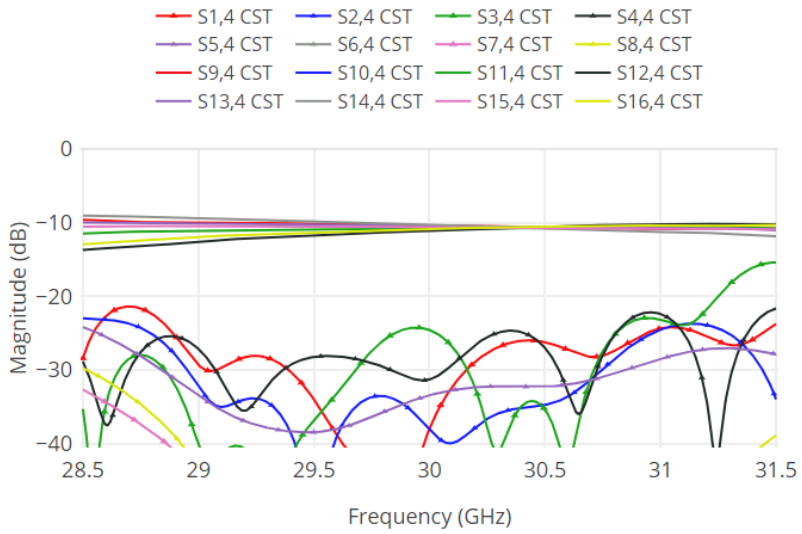

Figure 3.27: Simulated S-parameters of cross-configured Butler matrix; Port 4 excited.

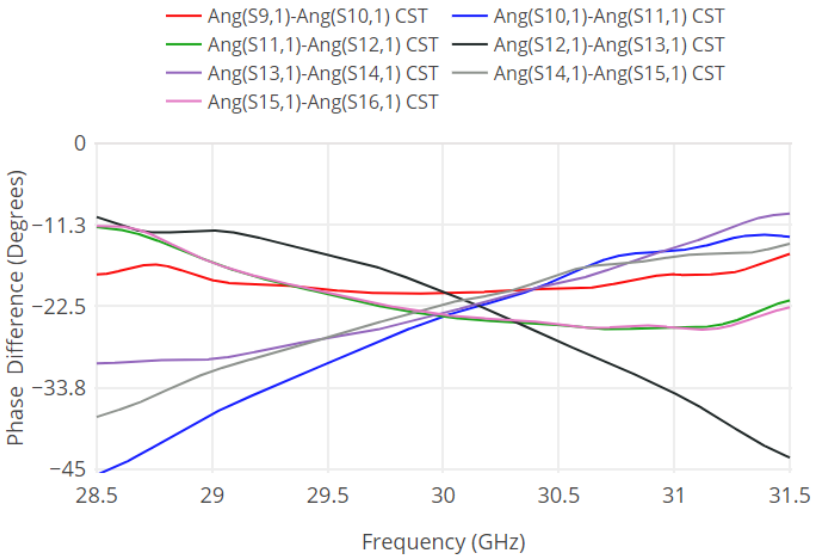

Figure 3.28: Simulated phase progressions at the output of the Butler matrix; Port 1 excited.

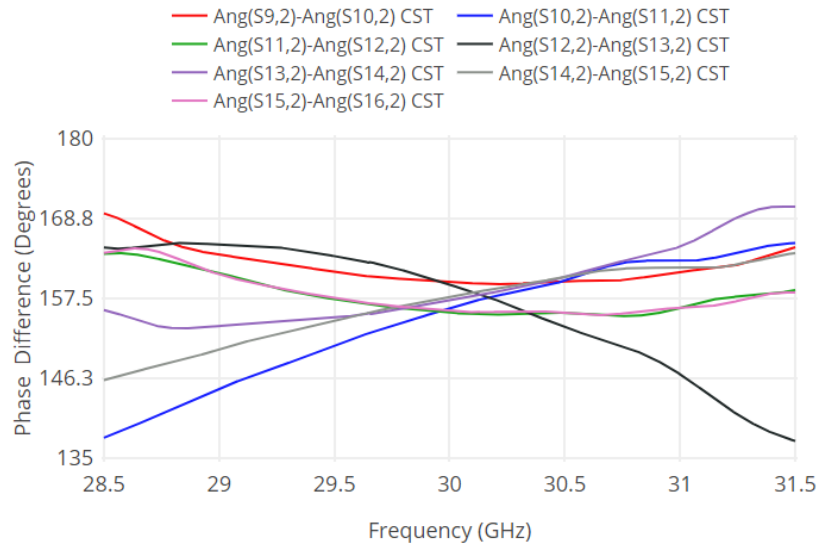

Figure 3.29: Simulated phase progressions at the output of the Butler matrix; Port 2 excited.

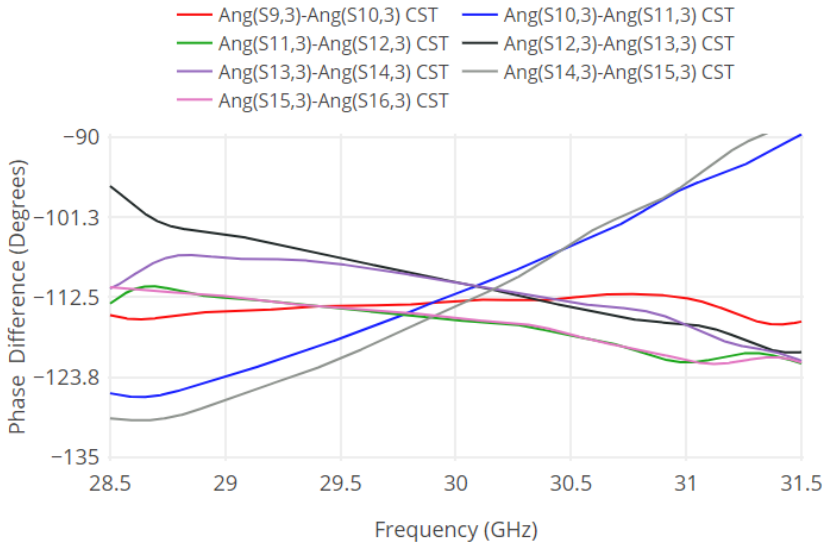

Figure 3.30: Simulated phase progressions at the output of the Butler matrix; Port 3 excited.

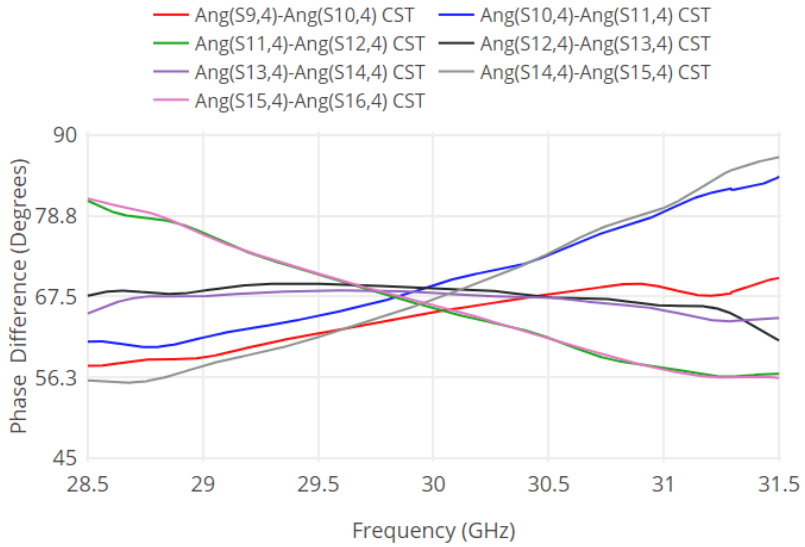

Figure 3.31: Simulated phase progressions at the output of the Butler matrix; Port 4 excited.

3.2.2 Design of the Array Networks

For the design of the array networks, two considerations should be noted; the first being that phase progressions determined by the bottom layer Butler matrix must be maintained at the top layer antenna outputs, and second, the passband filter transition must be fabricated into both of the top and bottom substrate layers. In the array examples that follow, it will be shown that the passband filters become staggered with respect to one another in order to mimic phase delay lines; the offsetting of the filters in this way allows for the Butler matrix phase progressions to be respected while simultaneously distributing the feed lines to their appropriate antenna ports.

1-dimensional broadside array

As discussed in Section 3.2.1, the output ports of the cross-configured Butler matrix scheme do not terminate in a sequential order and are distributed far greater then $\lambda/2$ spacing from each other. In order to realign the ports into a practical configuration, the top array layer is created with phase delay lines and two cross-over couplers. The phase delay lines are incorporated by staggering the passband filters that transfer the signal from the bottom layer to the top layer. Figure 3.32 demonstrates the bottom layer 8x8 butler matrix with the bottom layer of staggered passband filters attached. The individual filters are that of Section 3.1.4. Figure 3.33 depicts the top layer array configuration to be mounted on top of the Butler matrix layer. The structure is built to maintain the crucial phase shifts created by the Butler matrix, while simultaneously distributing the signal to the proper output ports.

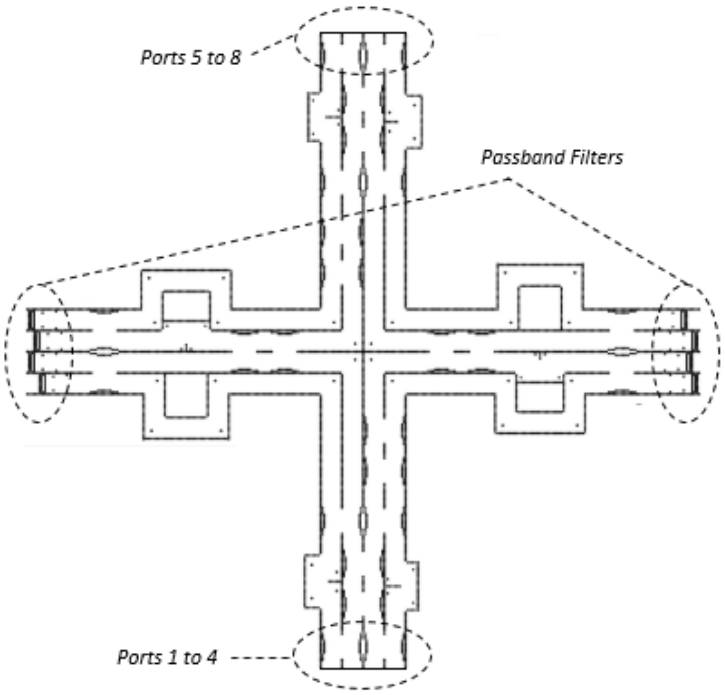

Figure 3.32: Cross-configured Butler matrix with passband filters attached.

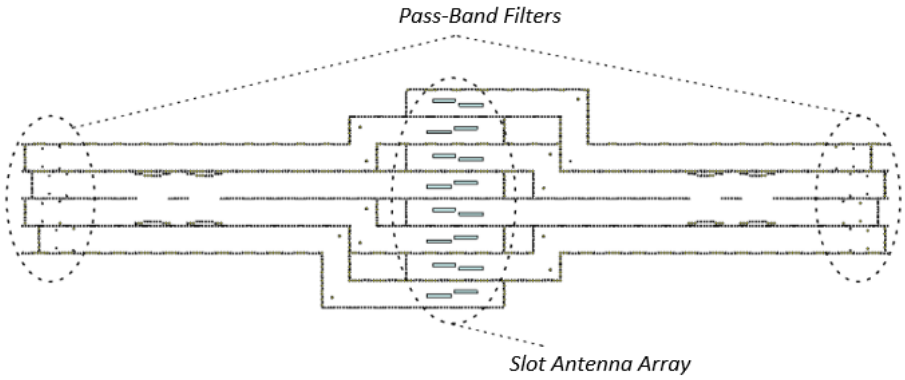

Figure 3.33: Staggered 2x8 antenna array structure.

The antennas are designed in a staggered configuration for desirable return loss and isolation. Table 3.10 and Figure 3.34 depict the layout of the antennas with respect to one another; the individual antenna dimensions are given in Section 3.1.3. Figure 3.35 depicts the simulated S-parameters of port 1 where the observed return loss and isolation are better than 10 dB over 28.5 to 31.5GHz. Excitation of the other ports and isolation values are similar.

Structural Parameters	Dimensions (mm)
l_7	17.790
w_7	10.000

Table 3.10: Parameter values of 2x8 antenna array geometry.

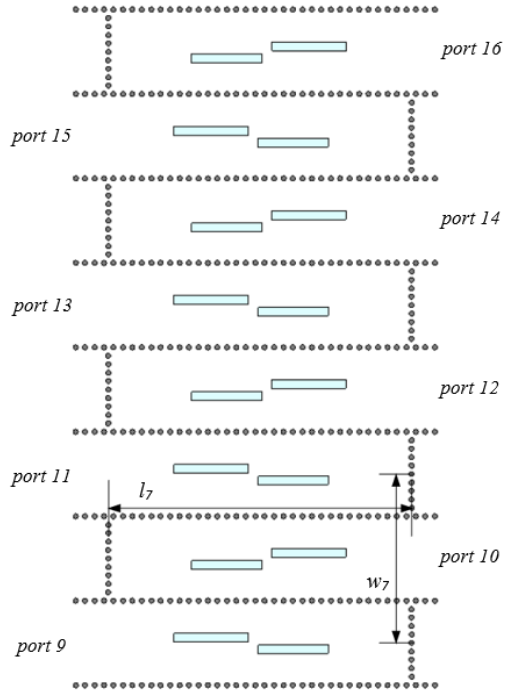

Figure 3.34: 2x8 antenna array geometry.

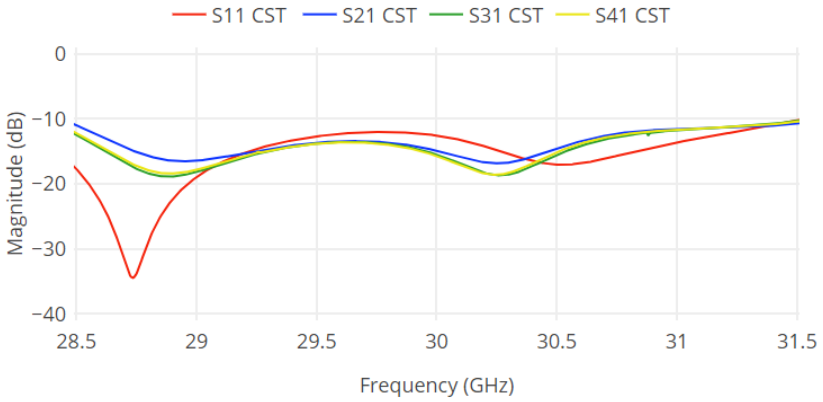

Figure 3.35: Simulated S-parameters of 2x8 antenna array.

2-dimensional broadside array

For the design of the 2-dimensional array structure, single center-slot antennas are proposed. In order to align the antennas for a practical beam configuration, the antennas are not staggered in a linear fashion as demonstrated in the 1-dimensional scanning array case, but terminated in a 2x4 format. An important note in this configuration is that the top layer array structure does not require the additional cross-over couplers for operation; the outputs are utilized in a non-sequential order. The phase distribution is maintained by a rearrangement of phase delay lines that compensate for the staggered passband filters required by the 1-dimensional array format. Figure 3.36 illustrates the top layer array structure. Table 3.11 and Figure 3.37 illustrate the 2x4 antenna array geometry and non-sequential alignment of the antenna ports. The simulated S-parameters of port 1 are depicted in Figure 3.38. The return loss and isolation are observed to be better than 10 dB over 28.5 to 31.5GHz. Excitation of the other ports and isolation values are similar.

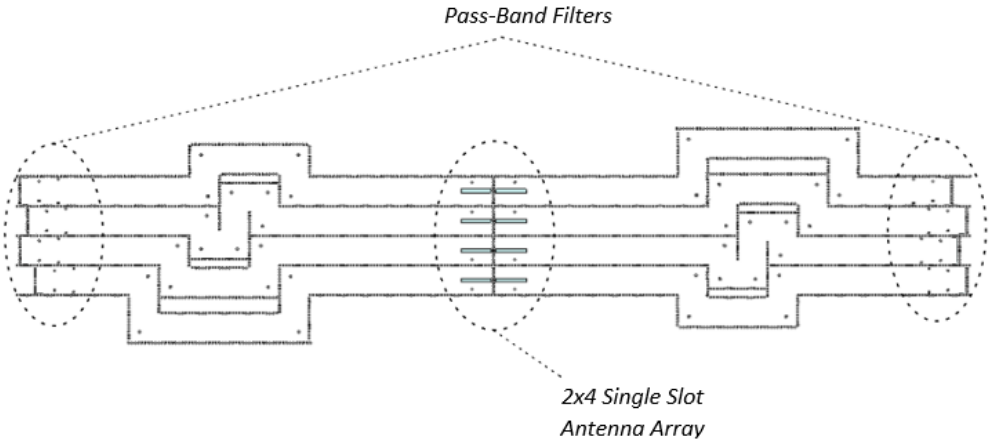

Figure 3.36: 2x4 center-slot antenna array structure.

Structural Parameters	**Dimensions (mm)**
l_8	5.800
w_8	5.000

Table 3.11: Parameter values of 2x4 antenna array geometry.

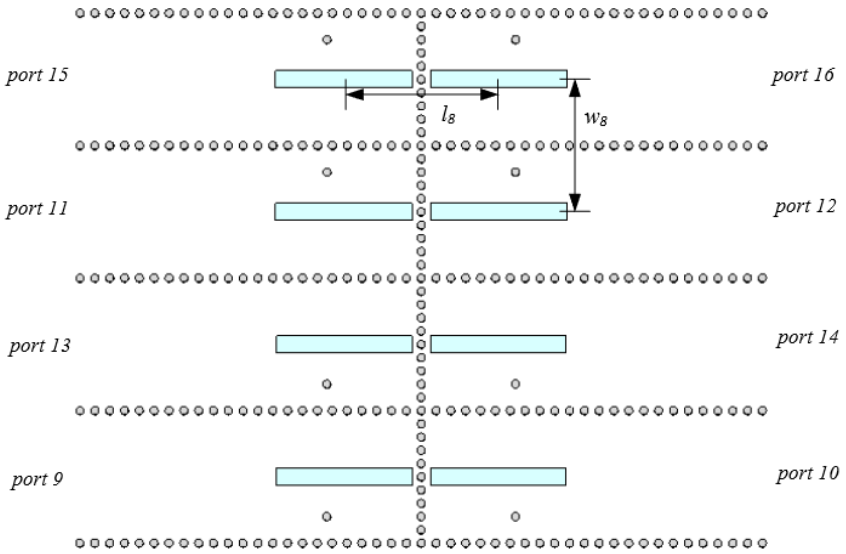

Figure 3.37: 2x4 antenna array geometry.

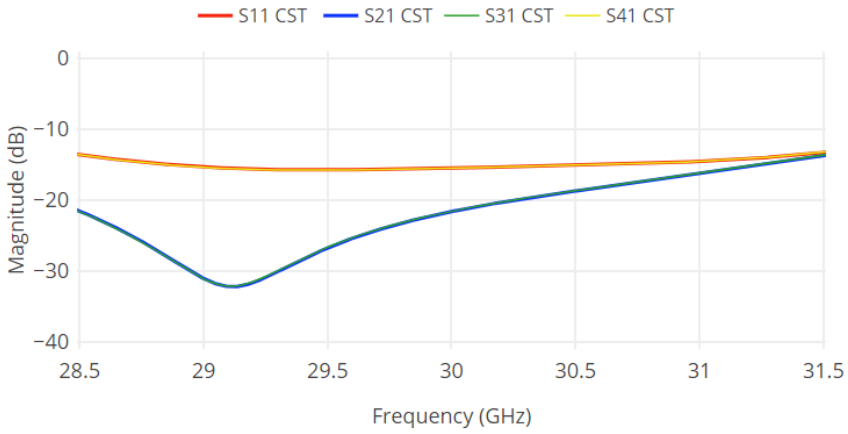

Figure 3.38: Simulated S-parameters of 2x4 antenna array.

3.2.3 Assembly and Simulation of the Beamforming Networks

Incorporating the top and bottom structures in a multi-layer configuration allows for operation as an eight-beam passive beamforming network. A top array layer is to be fixed to the bottom Butler matrix structure by nylon screws. The following subsections describe the operation, beam patterns, and simulated results while using each of the top layer array structures. The S-parameters and beams of the system were simulated using CST Microwave Studio's Time Domain Analysis simulator in

order to utilize multiple GPUs. It should be noted here that dielectric waveguide ports were used as the feeding method in each of the simulations; the goal being to reduce lengthy computational time, as well as demonstrate a substrate integrated circuit that can be integrated into a system that does not require bulky transitions or connectors.

1-dimensional beamforming network

Figure 3.39 illustrates an assembly view of the 1-dimensional top layer and the bottom matrix layer to be joined (metallized ground planes not shown). For visual reference, Figure 3.40 depicts the simulated output beam patterns of the structure at 30 GHz.

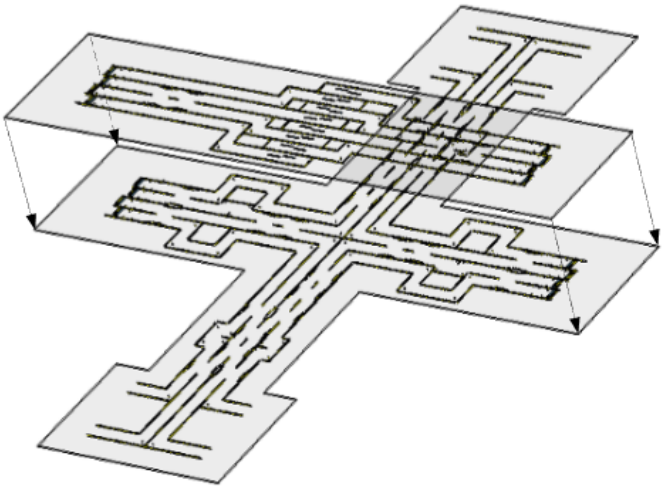

Figure 3.39: 1-dimensional beamforming network (assembly view).

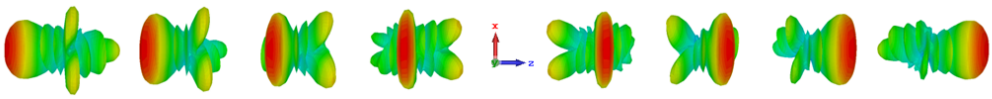

Figure 3.40: Simulated output beam pattern of the 1-dimensional beamforming network at 30 GHz.

The simulated results of the reflection coefficient from ports 1 through 8 are depicted in Figure 3.41. The return loss is observed to be better than 15 dB for each of the ports over 28.5 to 31.5 GHz and corresponds closely to the 20 dB level. The lowest return loss value at 30 GHz is approximately 23 dB. Although the Butler matrix is a symmetric device, the 2x8 slot antenna array adds a level of asymmetry; Figure

3.42 illustrates the array when it is rotated 180 degrees, and it can be noted that the staggering of the antenna slots slightly alters the layout. This antenna layout asymmetry with respect to the Butler matrix can explain the deviations between the supposed symmetric ports as seen in Figure 3.41. Nonetheless, the general shape and values are still quite similar.

The isolation between the input ports are demonstrated in Figures 3.43 to 3.46. The isolation levels correspond closely to the -20 dB level except for S7,2 in Figure 3.44; the isolation value averages close to -12.4 dB and remains better than -10 dB over the frequency range. This, in part, can be attributed to the layout of the array, as well as the top SIW layer cross-over couplers. This isolation parameter is shown to be improved in the 2-D system on the account of the alternative array layout, which in turn, does not require cross-over couplers in the top layer.

The eight output beams are demonstrated with respect to theta in Figure 3.47 and Figure 3.48 for 29.5 GHz and 30.5 GHz, respectively. The angular sweep allows for horizontal beam maxima at approximately ±7.0, ±22.0, ±38.0, and ±60.0 degrees when analyzed at 30 GHz, which agrees closely to values calculated using Equation 2.8 from Section 2.6. The asymmetries depicted in the 29.5 GHz and 30.5 GHz beam patterns of Figures 3.47 and 3.48 and seen in the 3-dimensional view of Figure 3.40 are also a product of the staggered 2x8 slot antenna arrangement asymmetry.

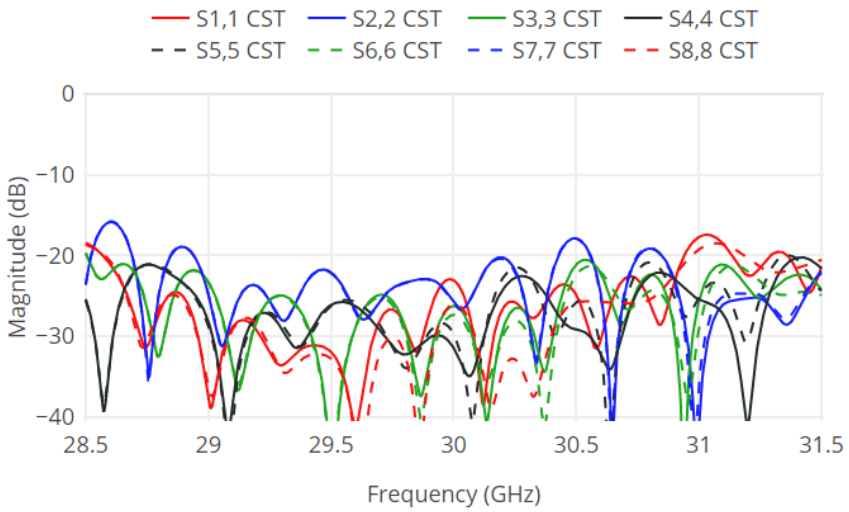

Figure 3.41: Simulated reflection coefficients results of 1-dimensional beamforming network.

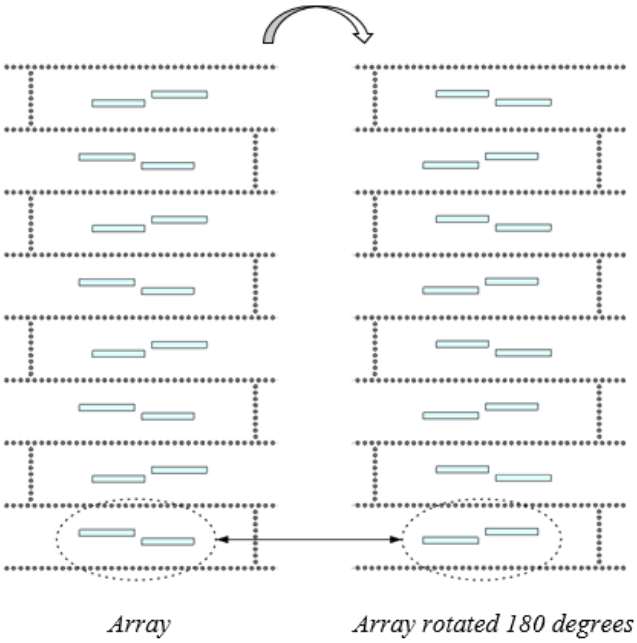

Figure 3.42: 180 degree rotation of the 2x8 antenna layout. The circled portions high-light several of the antenna asymmetries. These can be extended to the other slots as well.

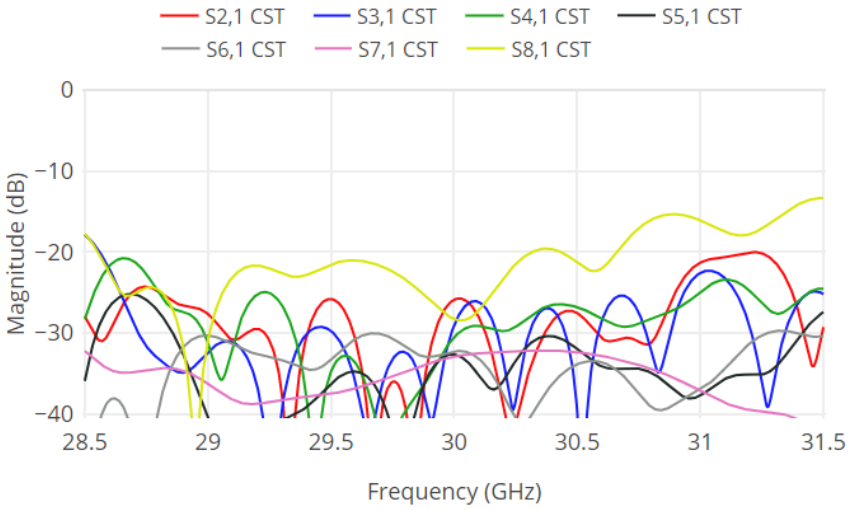

Figure 3.43: Simulated isolation results of 1-dimensional beamforming network; Port 1 excited.

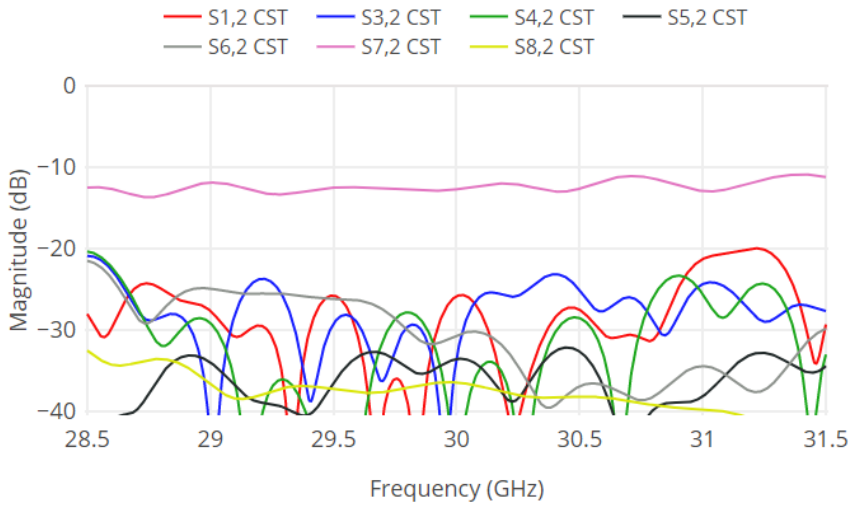

Figure 3.44: Simulated isolation results of 1-dimensional beamforming network; Port 2 excited.

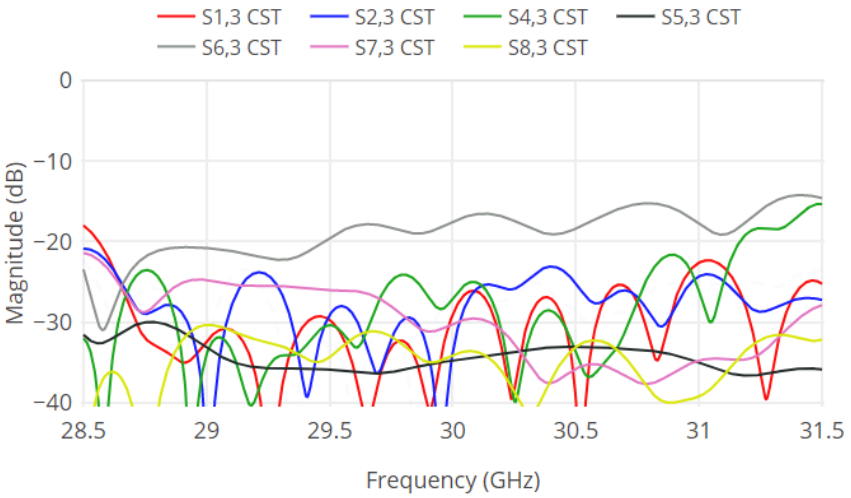

Figure 3.45: Simulated isolation results of 1-dimensional beamforming network; Port 3 excited.

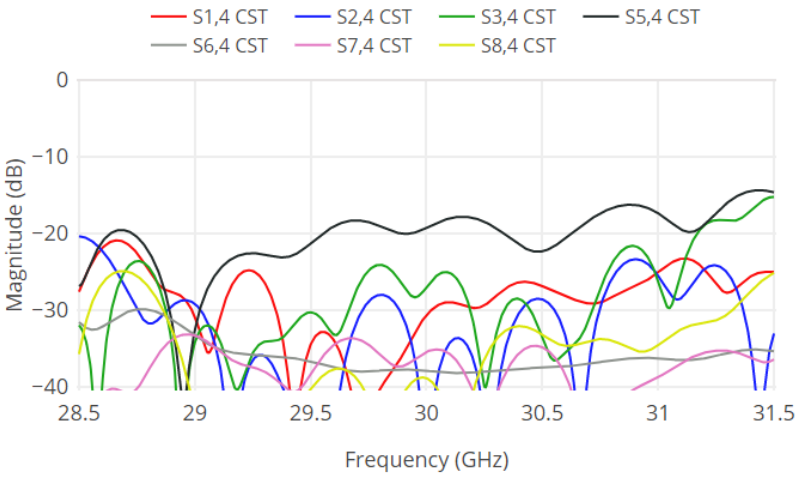

Figure 3.46: Simulated isolation results of 1-dimensional beamforming network; Port 4 excited.

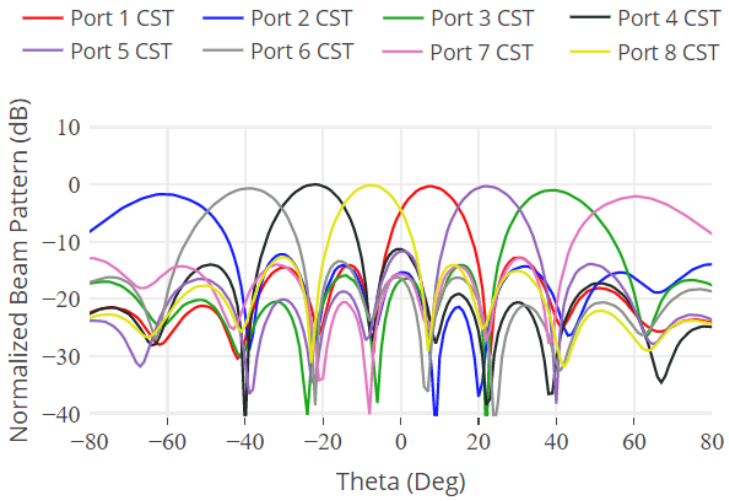

Figure 3.47: Normalized beam patterns of beamforming network with 1-dimensional scanning array at 29.5 GHz.

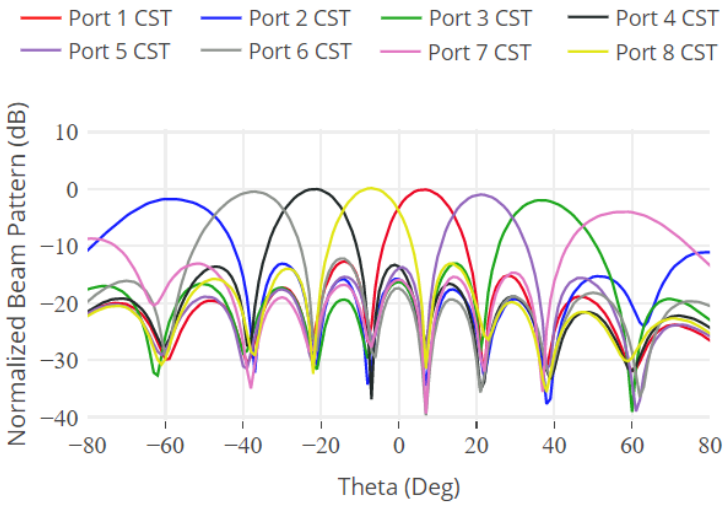

Figure 3.48: Normalized beam patterns of beamforming network with 1-dimensional scanning array at 30.5 GHz.

2-dimensional beamforming network

Figure 3.49 illustrates an assembly view of the 2-dimensional top layer and the bottom matrix layer to be joined (metallized ground planes not shown). For visual reference, Figure 3.50 depicts the simulated output beam patterns of the structure at 30 GHz.

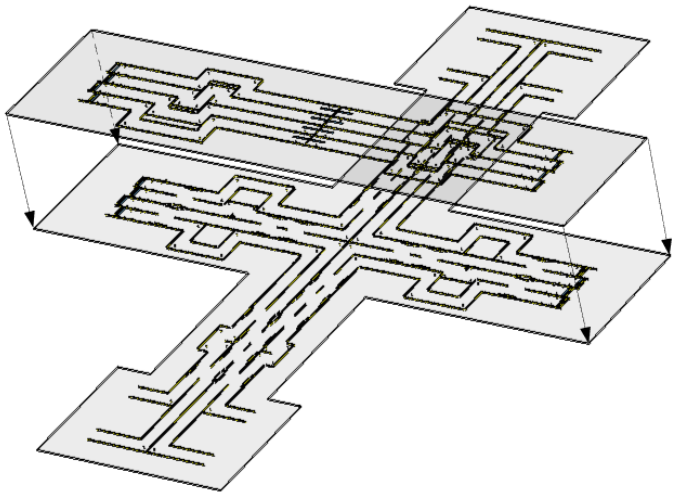

Figure 3.49: 2-dimensional beamforming network (assembly view).

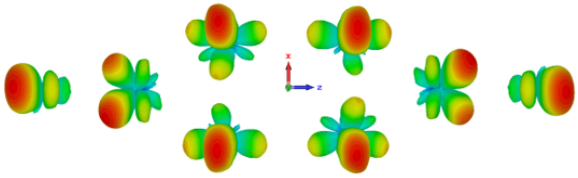

Figure 3.50: Simulated output beam pattern of the 2-dimensional beamforming network at 30 GHz.

The simulated reflection coefficients of Ports 1 through 4 are depicted in Figure 3.51. For this configuration, the layout of the array does not give rise to the same asymmetries as previously shown in the 1-dimensional scanning array example; therefore, ports 5 through 8 are symmetric (not shown). The return loss is observed to be better than 16 dB for each of the ports over 28.5 to 31.5 GHz, and correspond closely to the 20 dB level. The lowest return loss value at 30 GHz is approximately 25.5 dB. The isolation between the input ports is demonstrated in Figures 3.52 to 3.55. It can be noted that the isolation value of S7,2 is reduced significantly in Figure 3.53 when compare to that of Figure 3.44. Additionally, all of the isolation values remain under -11.5 dB over the frequency range. The eight output beams are demonstrated with respect to theta in Figure 3.56 and Figure 3.57 for 29 GHz and 31 GHz, respectively. At 30 GHz, the beam maxima coordinates (Azimuth,Elevation) are at approximately (±10.0,±14.0), (±10.0,∓24.0), (±44.0,±32.0) and (±36.0,∓8.0) degrees (as visualized in Figure 3.50.) The diagonal symmetries are a product of the phase progressions that determine the output beam angles. Figures 3.58 and 3.59 depict the angular sweep in the azimuth and elevation coordinate system at 30 GHz for ports 1 through 4.

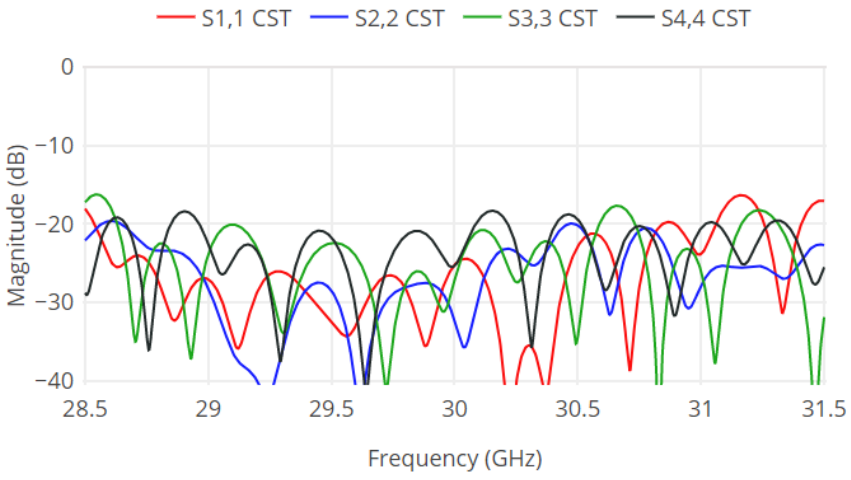

Figure 3.51: Simulated reflection coefficient results of 2-dimensional beamforming network.

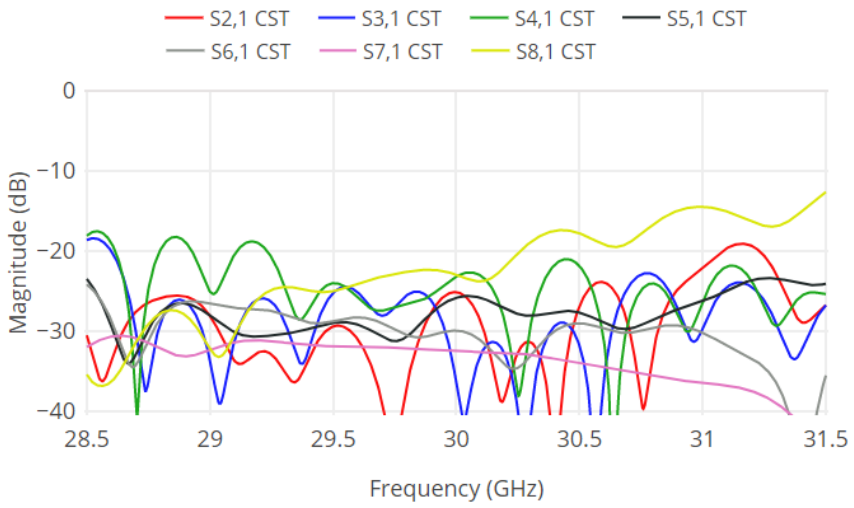

Figure 3.52: Simulated isolation results of 2-dimensional beamforming network; Port 1 excited.

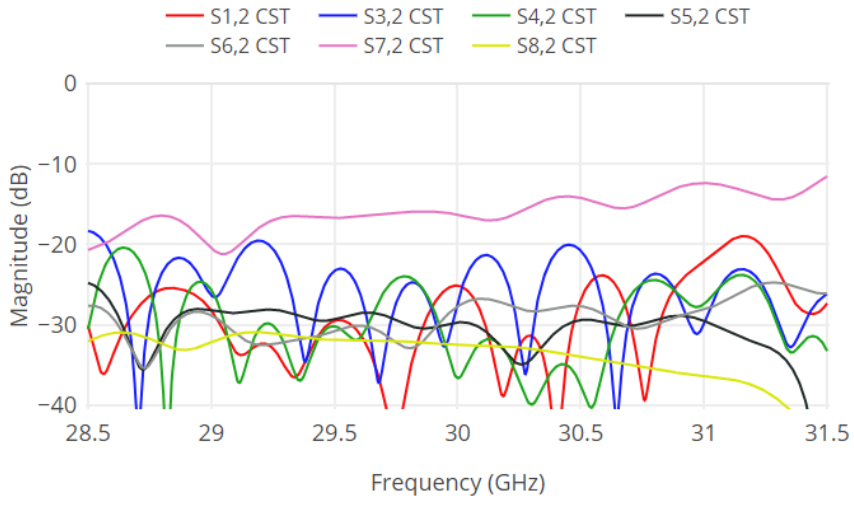

Figure 3.53: Simulated isolation results of 2-dimensional beamforming network; Port 2 excited.

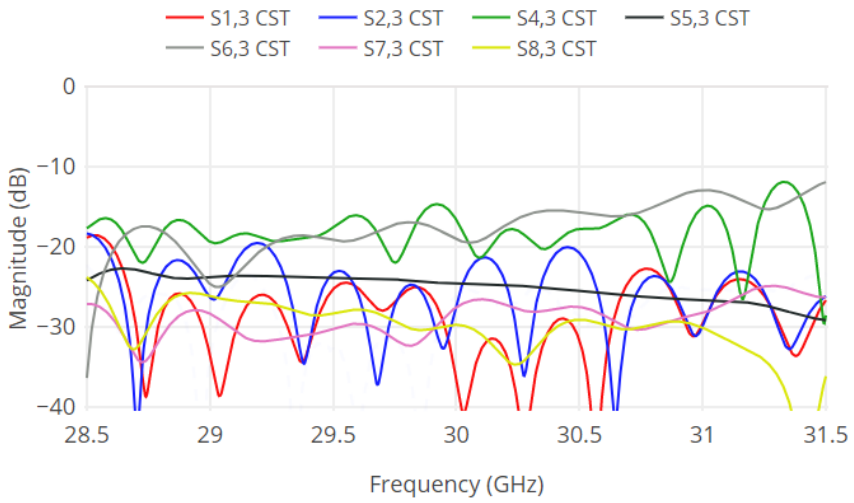

Figure 3.54: Simulated isolation results of 2-dimensional beamforming network; Port 3 excited.

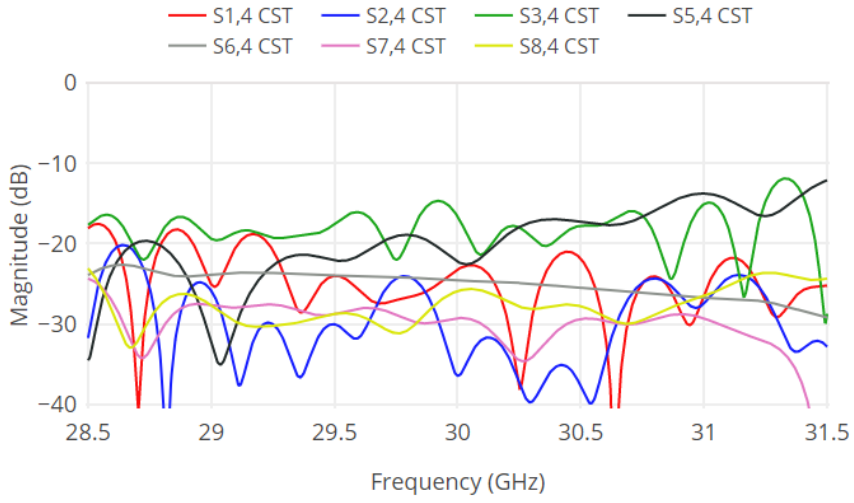

Figure 3.55: Simulated isolation results of 2-dimensional beamforming network; Port 4 excited.

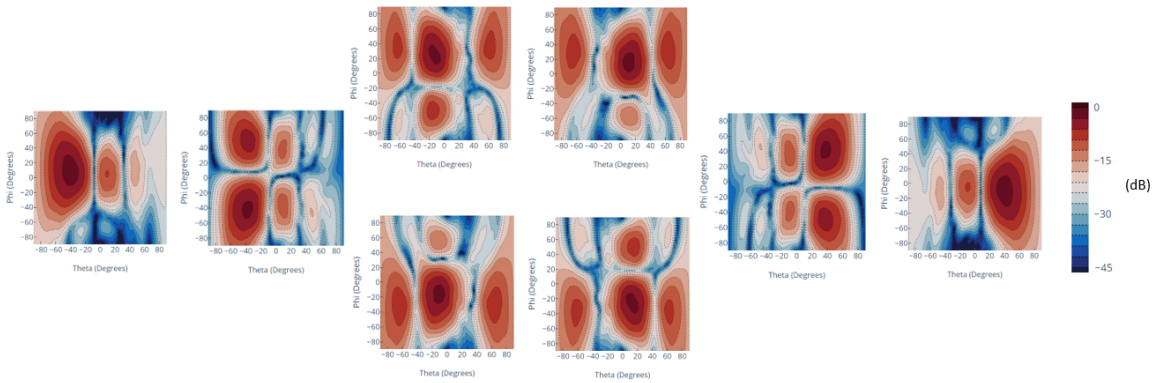

Figure 3.56: Normalized beam patterns of beamforming network with 2-dimensional scanning array at 29 GHz.

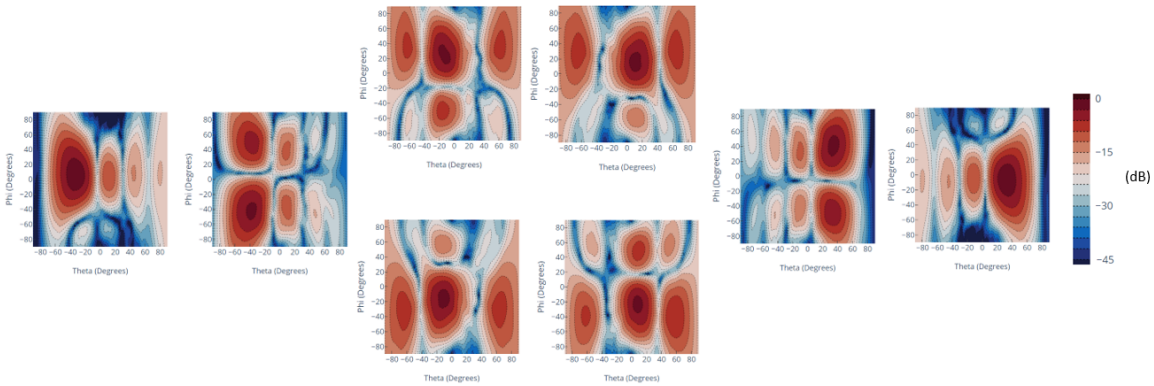

Figure 3.57: Normalized beam patterns of the beamforming network with 2-dimensional scanning array at 31 GHz.

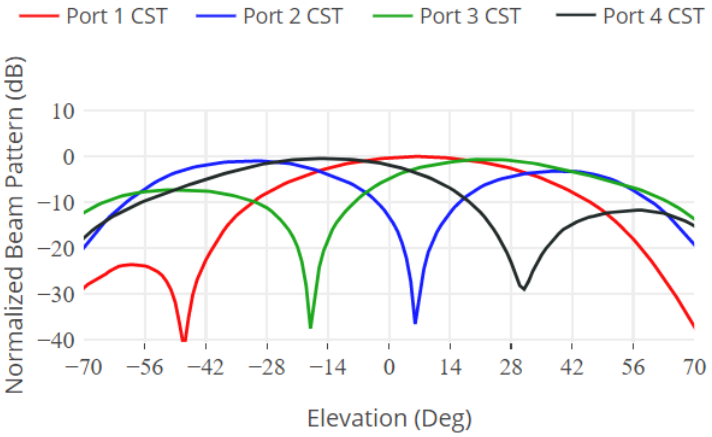

Figure 3.58: Normalized beam patterns of the beamforming network with 2-dimensional scanning array at 30 GHz (elevation cut of beam maxima).

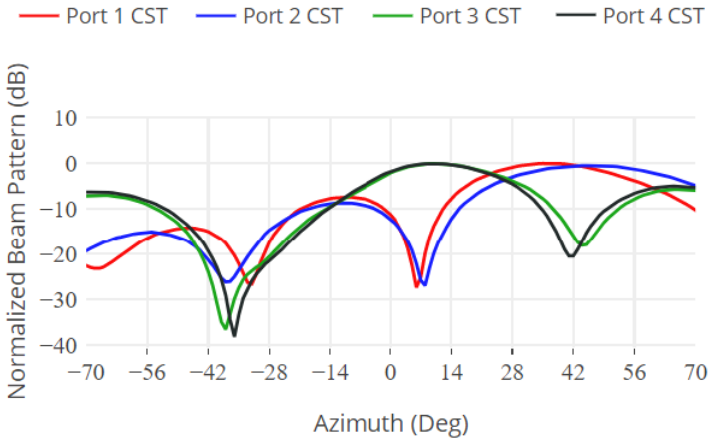

Figure 3.59: Normalized beam patterns of the beamforming network with 2-dimensional scanning array at 30 GHz (azimuth cut of beam maxima).

Chapter 4

Measurements and Testing

Prototypes of both the 1-dimensional and 2-dimensional beamforming networks were manufactured in Rogers Duroid 5880 with a substrate thickness of 0.508 mm and a metallization thickness of 0.035 mm. Figures 4.1 to 4.3 depict the via hole and slot layout of each layer that was sent for manufacturing. The 1-dimensional beamforming structure prototype is shown in Figure 4.4. The 2-dimensional beamforming structure prototype is shown in Figure 4.5. For both structures the maximum height and width is 235.0 mm x 193.3 mm. Nylon screws are used to mount the top layer structures to the bottom layer structure. Both of the circuits' S-parameter measurements were recorded using an Anritsu 37397C Vector Network Analyzer. End-launch connectors were used to connect the test cables to the microstrip input lines. TRL calibration standards were manufactured using the same dimensions for microstrip-to-SIW transitions as discussed in Section 3.1.6. Since the circuit simulations are fed by dielectric waveguide ports, the use of TRL calibration standards cancels the effects of the microstrip transitions and end-launch connectors; this is done to match the prototypes' measured S-parameter results to the simulated S-parameter results as closely as possible. Microwave absorbent material was placed on each of the microstrip input lines while not in use as a termination point.

For the analysis of the beam patterns, the anechoic chambers at the University of Victoria and at Queens University were used to test the 1-dimensional beamforming structure in the far-field. The 2-dimensional beamforming structure was tested with a near-field scanner at the University of Waterloo. Further discussion of the S-parameters and the beam pattern measurements are detailed in the forthcoming subsections.

Additional information on Rogers Duroid 5880, Southwest End-launch connectors 1902-03A-6, and Laird Eccosorb GDS can be found in Appendix A.

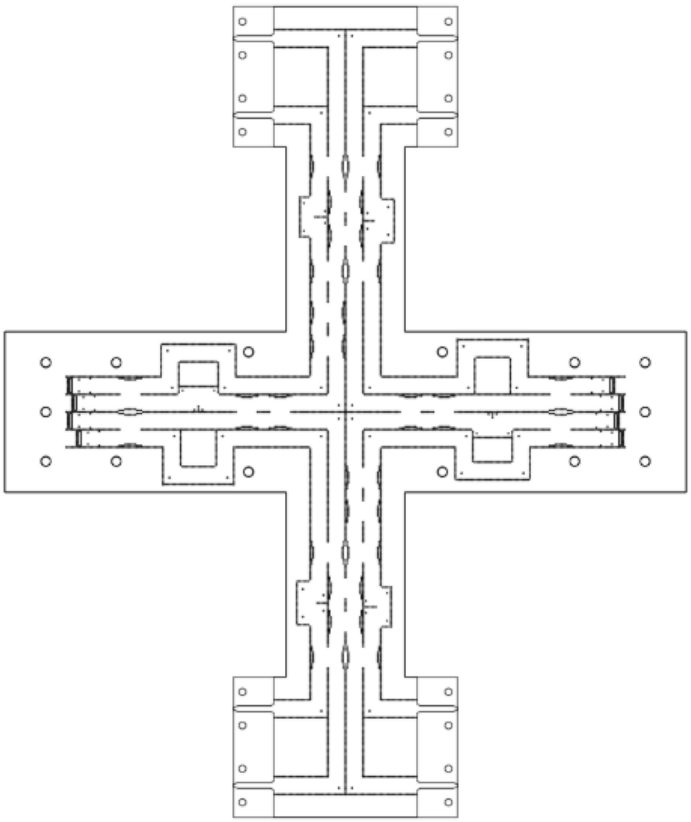

Figure 4.1: 8x8 cross-configuration Butler matrix layout for manufacture.

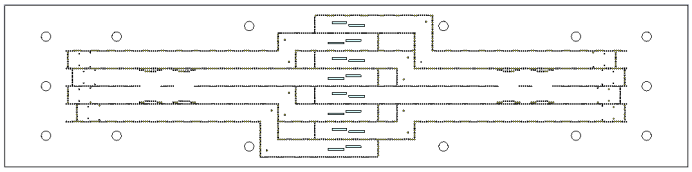

Figure 4.2: 1-dimensional array layout for manufacture.

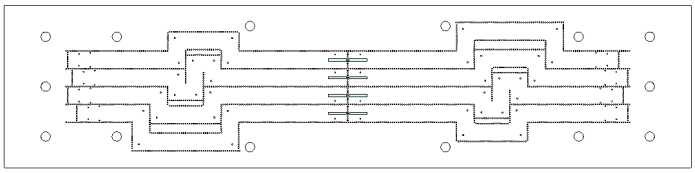

Figure 4.3: 2-dimensional array layout for manufacture.

Figure 4.4: Manufactured 1-dimensional beamforming prototype.

Figure 4.5: Manufactured 2-dimensional beamforming prototype.

4.1 Comparisons Between Simulated and Measured Results of the 1-Dimensional Beamforming Network

As discussed in Section 3.2.3, the 1-dimensional circuit is fully symmetric except for the layout of the antennas; the simulated reflection coefficient results differ slightly but are considered quite similar and for the purpose of this discussion, ports 1 through 4 are considered symmetric to ports 5 through 8. The simulated and measured reflection coefficient and isolation results for port 1 through 4 are compared in Figures 4.6 to 4.10. Studying the reflection coefficient comparison in Figure 4.6, it can be observed that the measured results follow the simulated results quite well. Each of the measured return loss values is better than 14.3 dB over the operating frequency range, and better

than 23.4 dB at 30 GHz. (Images of the reflection coefficients have been separated and added to the Appendix for reference). The isolation parameters in Figure 4.7 to 4.10 agree closely as well and follow the same general patterns. The majority of the measured isolation parameters remain around or below -20 dB over the spectrum investigated. Additionally, it can be noted that the highest isolation parameter (S7,2) of Figure 4.8 has a measured value better than 11.5 dB and is several decibels better then the simulations in the higher frequency range. Due to the layout of the structure, ports 5 through 8 also demonstrate similar results.

For demonstration of the beam sweep, ports 1 through 8 were measured at 29.5 and 30.5 GHz. During analysis of the data, it was noted that reflections were causing deterioration of the most outer beams (2, 5, 6, and 7). These reflections ranged on the order of several decibels. In order to reduce the reflections, the input cable, end-launch connector, and full structure surrounding the slot antennas were coated in an Eccosorb microwave absorbing material. The most notable reflections seemed to be caused by the metal cable connector and end-launch connector. Upon re-measurement, the reflections were dramatically reduced and a re-examination of the data produced the beam images depicted in Figures 4.11 and 4.12. These figures illustrate a comparison of the simulated and measured results over ±80 degrees for 29.5 and 30.5 GHz, respectively. Good agreement between the simulated and measured values can be observed. The gain of the beams produced from exciting ports 1 through 4 were calculated at 28.5 GHz, 29 GHz, 29.5 GHz, 30 GHz, 30.5 GHz, 31 GHz, and 31.5 GHz. The simulated and measured results are compared in Figure 4.13. The simulated gain ranges from approximately 9.6 dB to 13.5 dB while the measured gain ranges from approximately 7.6 dB to 13.0 dB.

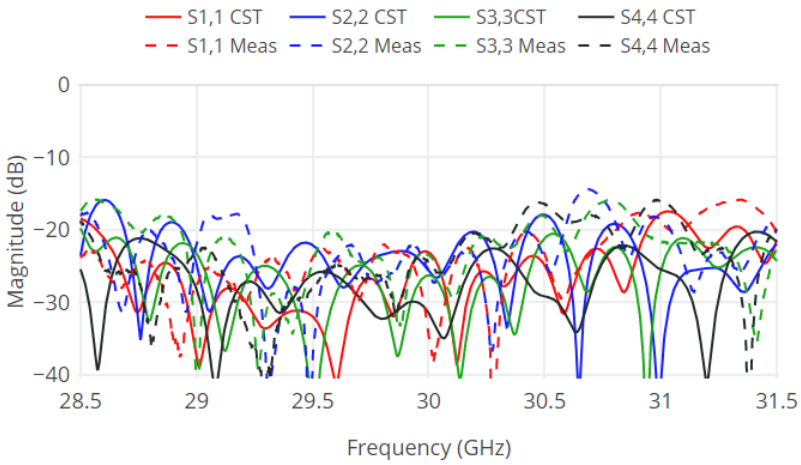

Figure 4.6: Simulated vs. measured reflection coefficient results of 1-dimensional beamforming network.

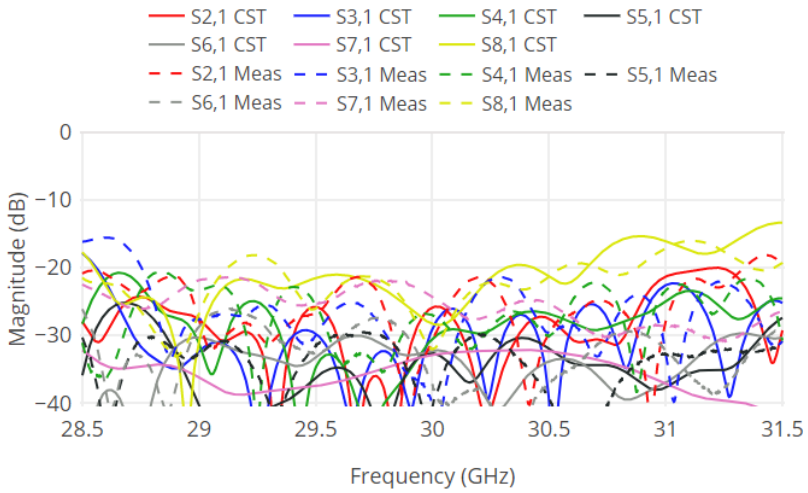

Figure 4.7: Simulated vs. measured isolation results of 1-dimensional beamforming network; Port 1 excited.

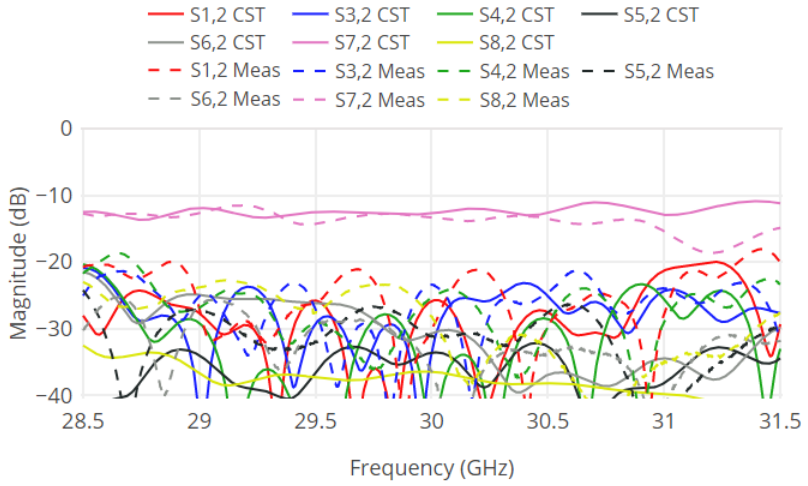

Figure 4.8: Simulated vs. measured isolation results of 1-dimensional beamforming network; Port 2 excited.

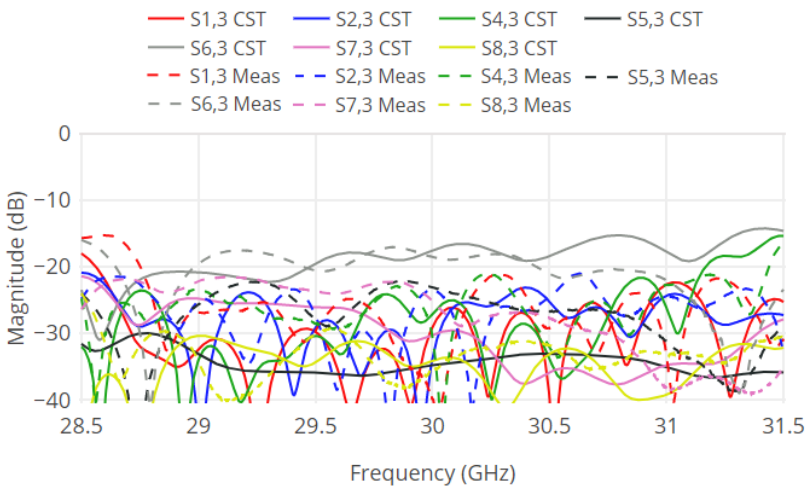

Figure 4.9: Simulated vs. measured isolation results of 1-dimensional beamforming network; Port 3 excited.

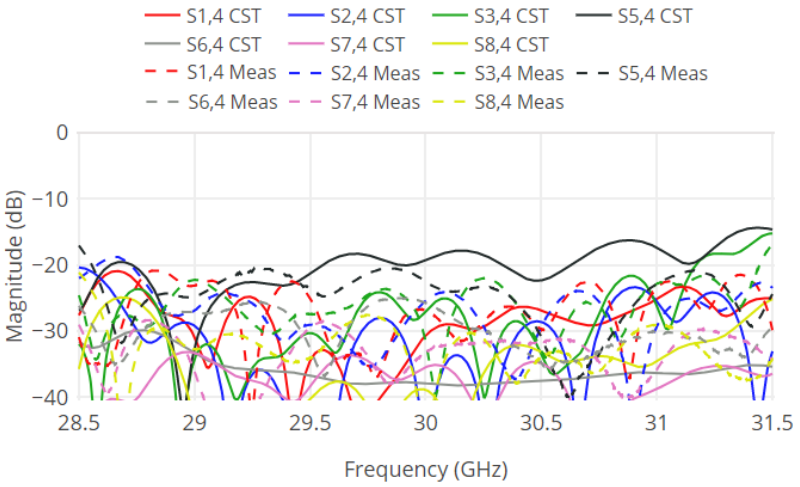

Figure 4.10: Simulated vs. measured isolation results of 1-dimensional beamforming network; Port 4 excited.

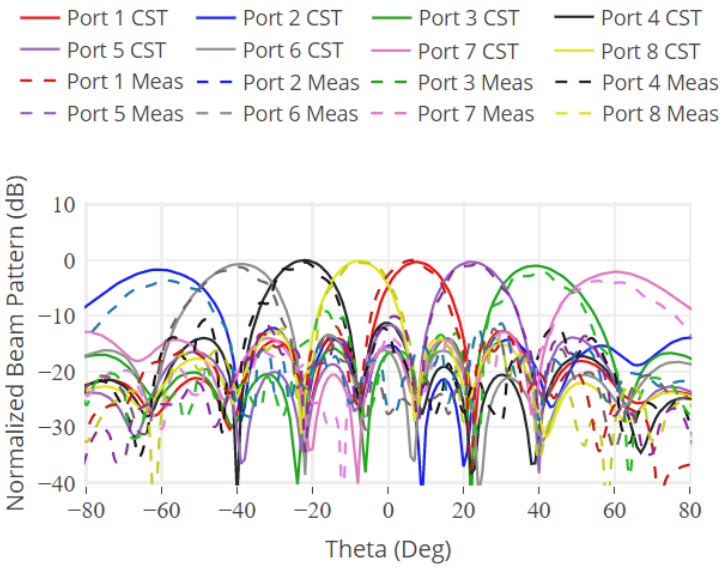

Figure 4.11: Simulated vs. measured beam patterns of 1-dimensional beamforming network at 29.5 GHz.

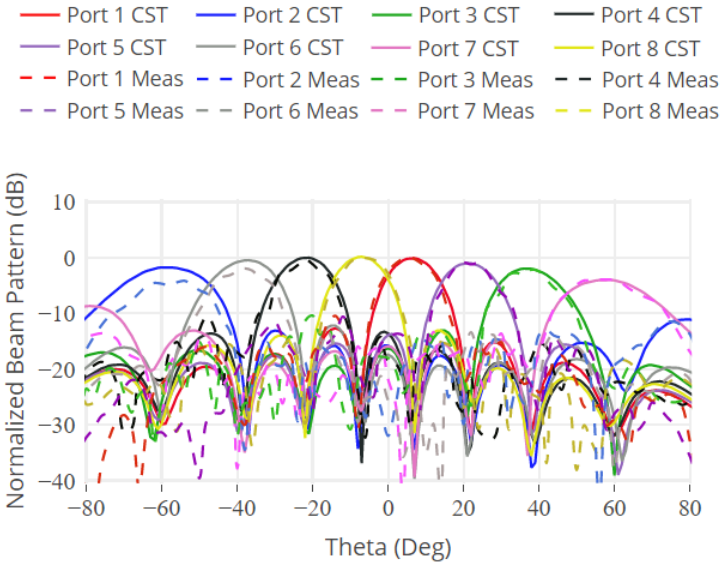

Figure 4.12: Simulated vs. measured beam patterns of 1-dimensional beamforming network at 30.5 GHz.

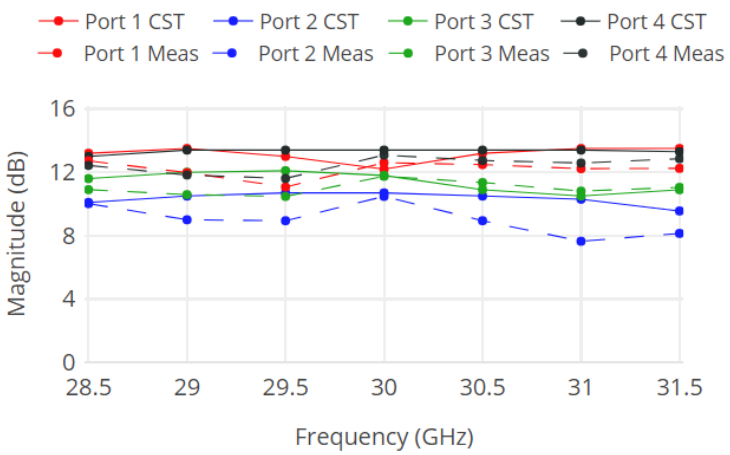

Figure 4.13: Simulated vs. measured gain of 1-dimensional beamforming network.

4.2 Comparisons Between Simulated and Measured Results of the 2-Dimensional Beamforming Network

The simulated and measured reflection coefficient and isolation results for port 1 through 4 are compared in Figures 4.14 to 4.18 for the 2-dimensional beamforming network. Studying the reflection coefficient comparison in Figure 4.14, it can be observed that the measured results follow the simulated results quite well. Each of the measured return loss values is better than 13.6 dB over the operating frequency range, and better than 17.6 dB at 30 GHz. The isolation parameters in Figure 4.15 to 4.18 agree closely as well and follow the same general patterns. The lowest measured isolation value is 13.4 dB and the majority of the measured isolation parameters remain around or below the -20 dB level over the spectrum investigated. Due to the layout of the structure, ports 5 though 8 also demonstrate similar results.

For demonstration of the 2-dimensional beam sweep, near-field measurements were taken at the University of Waterloo CAIRS facility. The following results demonstrate the beam patterns with the use of Eccosorb padding to mitigate reflections in the beam patterns. Figures 4.19 through 4.22 demonstrate the simulated and measured elevation and azimuth cuts along the beam maxima axes for 29.5 and 30.5 GHz. The beam angles are depicted over ± 70 degrees. Good agreement between the simulated and measured values can be observed. For ports 1 though 4, the gain of the beams was calculated at the maxima points for 29 GHz, 29.5 GHz, 30 GHz, 30.5 GHz, and 31 GHz, and then plotted in Figure 4.23. The simulated gain ranges from approximately

8.3 dB to 10.8 dB while the measured gain ranges from approximately 7.6 dB to 10.1 dB.

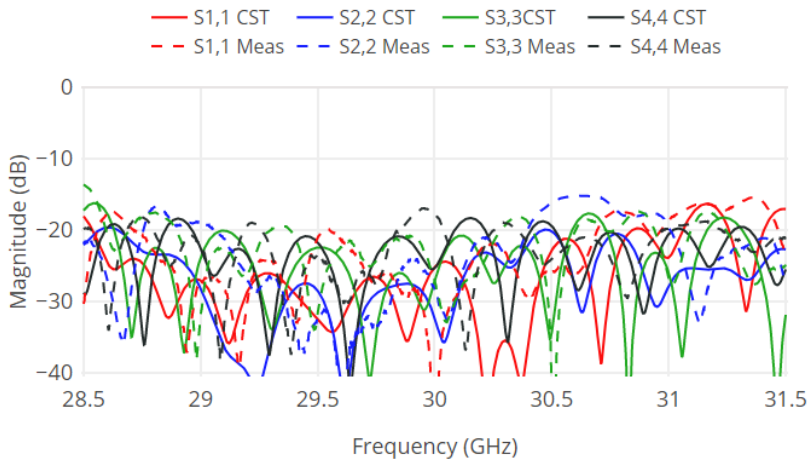

Figure 4.14: Simulated vs. measured reflection coefficient results of 2-dimensional beamforming network.

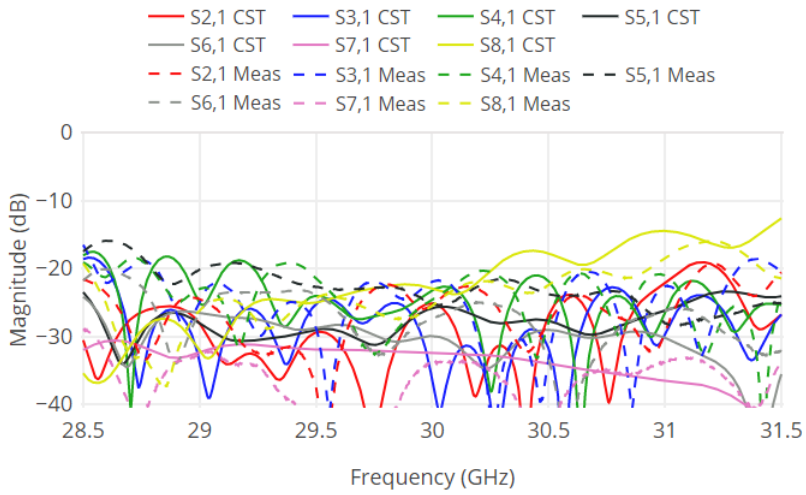

Figure 4.15: Simulated vs. measured isolation results of 2-dimensional beamforming network; Port 1 excited.

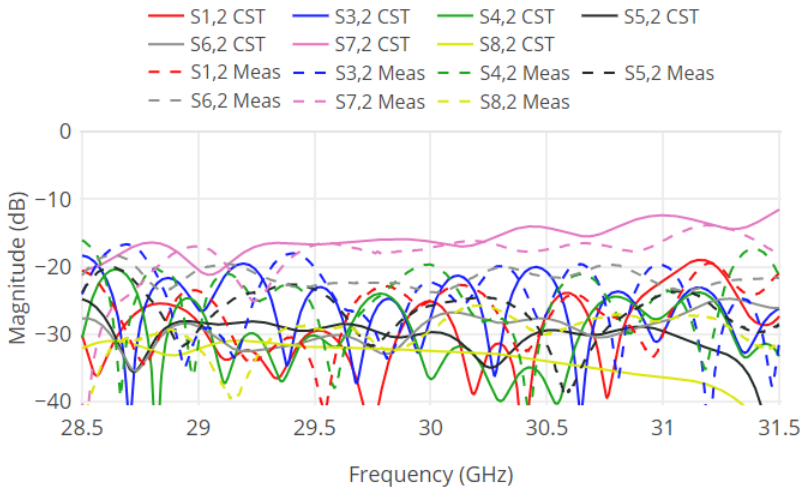

Figure 4.16: Simulated vs. measured isolation results of 2-dimensional beamforming network; Port 2 excited.

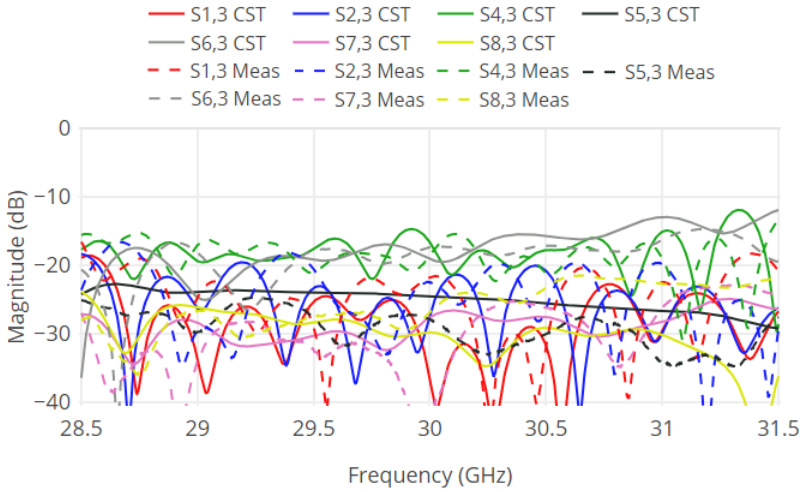

Figure 4.17: Simulated vs. measured isolation results of 2-dimensional beamforming network; Port 3 excited.

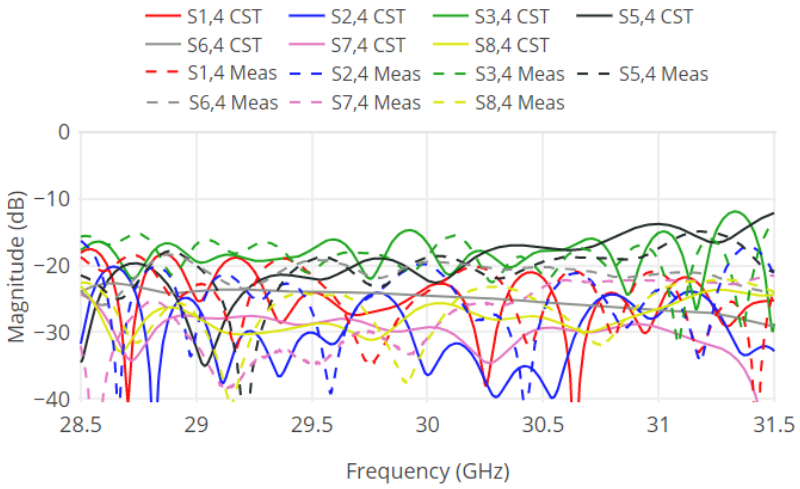

Figure 4.18: Simulated vs. measured isolation results of 2-dimensional beamforming network; Port 4 excited.

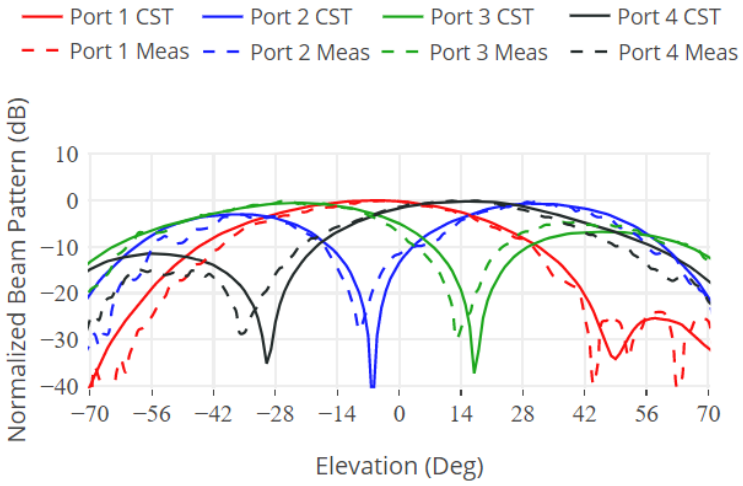

Figure 4.19: Simulated vs. measured elevation cuts of 2-dimensional beamforming network at beam maxima (29.5 GHz).

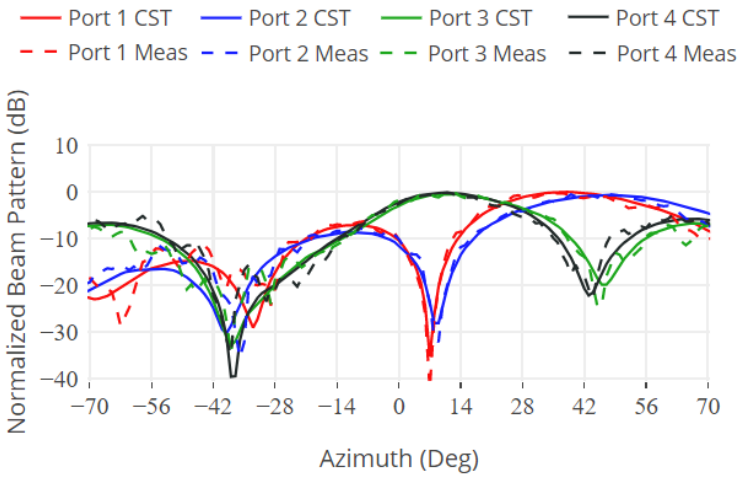

Figure 4.20: Simulated vs. measured azimuth cuts of 2-dimensional beamforming network at beam maxima (29.5 GHz).

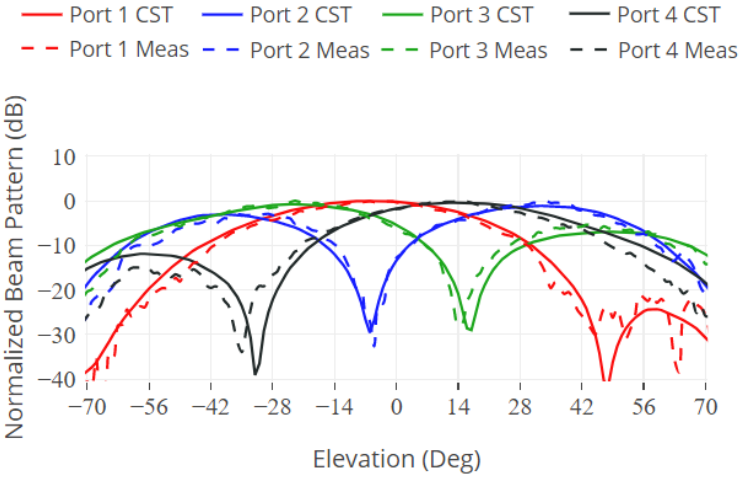

Figure 4.21: Simulated vs. measured elevation cuts of 2-dimensional beamforming network at beam maxima (30.5 GHz).

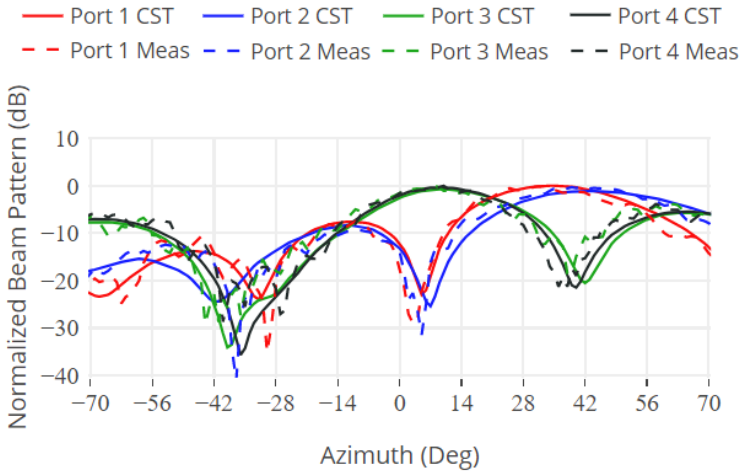

Figure 4.22: Simulated vs. measured azimuth cuts of 2-dimensional beamforming network at beam maxima (30.5 GHz).

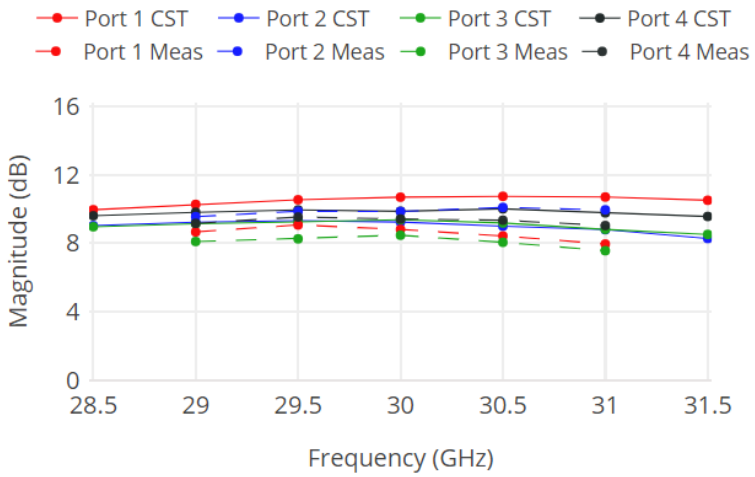

Figure 4.23: Simulated vs. measured gain of 2-dimensional beamforming network at beam maxima coordinates.

For both the 1-D and 2-D examples in this work, the measured results agree closely with the simulated results, thus validating the design approach and feasibility of the 8x8 cross-configuration Butler matrix as a beamforming network in SIW technology. Physical reconfigurability of the system is an important attribute for future applications that may require different beam specifications; restrictions such as cost and the impact of environmental surroundings can be taken into account in this manner.

The location of passband filters between the top and bottom SIW layers also allow for more versatile configurations that can include expanded array sizes, as well as the integration of larger or more stringent filters to be designed.

Chapter 5

Conclusion and Future Work

5.1 Summary

As demands for larger bandwidths rise, substrate integrated waveguide circuits are presented as a feasible option due to their desirable characteristics at high frequencies. In contrast to rectangular waveguides, substrate integrated waveguides offer a low-cost, light-weight, and compact solution while maintain a high quality-factor. Due to being manufactured on a dielectric material, substrate integrated circuits are versatile and transitions can be used to easily incorporate other technologies such as microstrip or to attach active component elements.

Butler matrices have been demonstrated as a powerful technique for beam steering. Many applications and configurations are available for use in different technologies. Miniaturization, component reduction, and phase error reduction are all topics of interest in advancing Butler matrix applications. In this work, a substrate integrated 8x8 Butler matrix was reconfigured into a cross configuration. The number of cross-over couplers is reduced to six in the bottom layer. A second layer serving as the array structure was connected using direct coupled folded passband filters. Two separate array structures were created and tested to demonstrate a typical 1-dimensional sweep with eight individual beams and a 2-dimensional sweep with eight individual beams. The 1-dimensional array requires two additional cross-over couplers in order to distribute the signals appropriately. The 2-dimensional array requires no additional cross-overs, but requires further manipulation of phase delay lines in order to compensate for the layout of the array. The 1-dimensional beamforming systems measured results have been shown to have a return loss better than 14.3 dB and isolation better than 11.5 dB. These measured results agree closely with the simulated results. By

applying microwave absorbent material to reduce reflections, the 1-dimensional measured beams agree well with the simulated results and demonstrate a measured gain of approximately 7.6 to 13 dB over 28.5 to 31.5 GHz. The 2-dimensional beamforming system's measured results have been shown to have a return loss better than 13.6 dB and isolation better than 13.4 dB. These results agree closely with the simulated results as well. By applying microwave absorbent material to reduce reflections while taking near-field measurements, the measured patterns agree well with the simulated results and demonstrate a measured gain of approximately 7.6 to 10.1 dB over 29.0 to 31.0 GHz.

5.2 Future Work

This work was able to demonstrate good results utilizing the given cross-configured Butler matrix in the range of 28.5 to 31.5 GHz. As for future developments and research interests on this system, several notes can be made and are addressed as follows:

System Integration and Enclosure

Although reflections in the beam patterns have been successfully mitigated with the use of Eccosorb microwave absorbing material, the integration and development of a proper circuit housing can be investigated further. Dielectric waveguide ports were used to feed the circuit in the simulations with the hopes that future advancements in substrate-integrated circuits will eliminate the use of bulky input connections or even microstrip input lines. By eliminating the input connectors and cables, as well as mounting in a proper electromagnetic enclosure, reflections can be eliminated.

Miniaturization

The configuration of this matrix addresses the use of components throughout the system but an optimal arrangement can be further investigated to reduce the physical size. Many areas of the structure can have redundant via holes removed, and the phase shifters can be rearranged to save space. The reduction of physical size and component arrangement is an area of future interest.

Isolation

An area of interest in future work is on the matter of isolation parameter S7,2 of Figure 4.8 in Chapter 4. This isolation value is worse than most of the isolation parameters observed in the system. A similar result can be seen in the multi-layer system of [6]. Future work on this type of system can investigate and possibly mitigate this isolation value.

Phase Error

Phase error and phase distribution in Butler matrices is an important topic of interest. In this configuration, there is abundant physical and conceptual room for phase error reduction through the careful use of components and phase shifters. A considerable amount of time can be spent addressing this.

Filter Dynamics

In this project, a simple direct coupled folded filter was used as the transition medium between the SIW layers; future work can include the use of more dynamic filters that utilize transmission zeros and are designed for specific applications.

Beam Patterns

Regarding the top layer array configurations, the antenna positions and array layout in both the 1-dimensional and 2-dimensional structures can be easily altered. Research can be conducted to developed more creative (or dramatic) beam patterns and beam widths. Additionally, research can be conducted to reduce asymmetries as well as investigate side-lobe suppression.

Computational Time

Due to the size and format of the beamforming networks, the computational time becomes excessively long without the use of GPUs. Simulations must have a balanced trade off between the computation time and cost to be practical. Reducing either of these constraints can open up a wide range of future work such as aforementioned research interests or even work on multi-layer multi-port power amplifiers. As computer systems advance, and computational time (and cost) decreases, significant advancements can be contributed to this type of system.

Bibliography

[1] I. Uchendu and J. R. Kelly, "Survey of beam steering techniques available for millimeter wave applications," *Progress in Electromagnetics Research*, vol. 68, pp. 35–54, 2016.

[2] V. Geethanjali, T. Mohan, and I. Rao, "Beamforming networks to feed array antennas," *Indian Journal of Science and Technology*, vol. 8, no. S2, pp. 78–81, 2015.

[3] J. Butler and R. Lowe, "Beam-forming matrix simplifies design of electronically scanned antenna," *Electron. Design*, vol. 9, pp. 170–173, 1961.

[4] X. Cheng, Y. Yao, T. Tomura, J. Hirokawa, T. Yu, J. Yu, and X. Chen, "A compact multi-beam end-fire circularly polarized septum antenna array for millimeter-wave applications," *IEEE Access*, vol. 6, pp. 62784–62792, 2018.

[5] Y. Li and K.-M. Luk, "A multibeam end-fire magnetoelectric dipole antenna array for millimeter-wave applications," *IEEE Transactions on Antennas and Propagation*, vol. 64, no. 7, pp. 2894–2904, 2016.

[6] L.-H. Zhong, Y.-L. Ban, J.-W. Lian, Q.-L. Yang, J. Guo, and Z.-F. Yu, "Miniaturized SIW multibeam antenna array fed by dual-layer 8×8 Butler matrix," *IEEE Antennas Wireless Propag. Lett*, vol. 16, pp. 3018–3021, 2017.

[7] J.-W. Lian, Y.-L. Ban, Y.-Q. Wu, and L.-H. Zhong, "Compact 28-GHz two-dimensionally scanning multibeam array with sidelobe suppression," in *2018 IEEE MTT-S International Wireless Symposium*, pp. 1–4, 2018.

[8] W. Yang, Y. Yang, W. Che, C. Fan, and Q. Xue, "94-GHz compact 2-d multi-beam LTCC antenna based on multifolded SIW beam-forming network," *IEEE Transactions on Antennas and Propagation*, vol. 65, no. 8, pp. 4328–4333, 2017.

[9] K. Wincza, S. Gruszczynski, and K. Sachse, "Broadband planar fully integrated 8x8 Butler matrix using coupled-line directional couplers," *IEEE Transactions on Microwave Theory and Techniques*, vol. 59, no. 10, pp. 2441–2446, 2011.

[10] K. Wincza and S. Gruszczynski, "Broadband integrated 8x8 Butler matrix utilizing quadrature couplers and Schiffman phase shifters for multibeam antennas

with broadside beam," *IEEE Transactions on Microwave Theory and Techniques*, vol. 64, no. 8, pp. 2596–2604, 2016.

[11] J. G. Andrews, S. Buzzi, W. Choi, S. V. Hanly, A. Lozano, A. C. Soong, and J. C. Zhang, "What will 5G be?," *IEEE Journal on Selected Areas in Communications*, vol. 32, no. 6, pp. 1065–1082, 2014.

[12] M. U. Memon and S. Lim, "Review of reconfigurable substrate-integrated-waveguide antennas," *Journal of Electromagnetic Waves and Applications*, vol. 28, no. 15, pp. 1815–1833, 2014.

[13] M. Bozzi, A. Georgiadis, and K. Wu, "Review of substrate-integrated waveguide circuits and antennas," *IET Microwaves, Antennas & Propagation*, vol. 5, no. 8, p. 909, 2011.

[14] A. Kumar and S. Raghavan, "A review: Substrate integrated waveguide antennas and arrays," *Journal of Telecommunication, Electronic and Computer Engineering (JTEC)*, vol. 8, no. 5, pp. 95–104, 2016.

[15] K. Wu, D. Deslandes, and Y. Cassivi, "The substrate integrated circuits-a new concept for high-frequency electronics and optoelectronics," in *Proceedings of the 6th International Conference on Telecommunications in Modern Satellite, Cable and Broadcasting Service*, vol. 1, pp. P–III, IEEE, 2003.

[16] D. Deslandes and K. Wu, "Accurate modeling, wave mechanisms, and design considerations of a substrate integrated waveguide," *IEEE Transactions on Microwave Theory and Techniques*, vol. 54, no. 6, pp. 2516–2526, 2006.

[17] W. Che, K. Deng, D. Wang, and Y. L. Chow, "Analytical equivalence between substrate-integrated waveguide and rectangular waveguide," *IET Microwaves, Antennas & Propagation*, vol. 2, no. 1, pp. 35–41, 2008.

[18] F. Xu and K. Wu, "Guided-wave and leakage characteristics of substrate integrated waveguide," *IEEE Transactions on Microwave Theory and Techniques*, vol. 53, no. 1, pp. 66–73, 2005.

[19] L. Yan, W. Hong, G. Hua, J. Chen, K. Wu, and T. J. Cui, "Simulation and experiment on SIW slot array antennas," *IEEE Microwave and Wireless Components Letters*, vol. 14, no. 9, pp. 446–448, 2004.

[20] M. Salehi and E. Mehrshahi, "A closed-form formula for dispersion characteristics of fundamental SIW mode," *IEEE Microwave and Wireless Components Letters*, vol. 21, no. 1, pp. 4–6, 2011.

[21] Y. Cassivi, L. Perregrini, P. Arcioni, M. Bressan, K. Wu, and G. Conciauro, "Dispersion characteristics of substrate integrated rectangular waveguide," *IEEE Microwave and Wireless Components Letters*, vol. 12, no. 9, pp. 333–335, 2002.

[22] Z. Kordiboroujeni and J. Bornemann, "Designing the width of substrate integrated waveguide structures," *IEEE Microwave and Wireless Components Letters*, vol. 23, no. 10, pp. 518–520, 2013.

[23] F. Taringou, *Transitions from substrate integrated waveguide to planar transmission lines and their applications to amplifier integration.* PhD thesis, University of Victoria, Victoria, BC, Canada, 2012.

[24] H. J. Riblet, "The short-slot hybrid junction," *Proceedings of the IRE*, vol. 40, no. 2, pp. 180–184, 1952.

[25] Z. Hao, W. Hong, J. Chen, H. Zhou, and K. Wu, "Single-layer substrate integrated waveguide directional couplers," *IEE Proceedings-Microwaves, Antennas and Propagation*, vol. 153, no. 5, pp. 426–431, 2006.

[26] Z. Kordiboroujeni, J. Bornemann, and T. Sieverding, "Mode-matching design of substrate-integrated waveguide couplers," in *Proceedings of the Asia-Pacific Symposium on Electromagnetic Compatibility*, pp. 701–704, 2012.

[27] B. Rahali and M. Feham, "Design of K-band substrate integrated waveguide coupler, circulator and power divider," *International Journal of Information and Electronics Engineering*, vol. 4, no. 1, p. 47, 2014.

[28] D. M. Pozar, *Microwave Engineering, 3rd ed.* John Wiley & Sons, 2005.

[29] H. J. Riblet, "A mathematical theory of directional couplers," *Proceedings of the IRE*, vol. 35, no. 11, pp. 1307–1313, 1947.

[30] T. A. Denidni and T. E. Libar, "Wide band four-port Butler matrix for switched multibeam antenna arrays," in *14th International Symposium on Personal, Indoor and Mobile Radio Communication Proceedings*, vol. 3, pp. 2461–2464, 2003.

[31] R. Elliott and L. Kurtz, "The design of small slot arrays," *IEEE Transactions on Antennas and Propagation*, vol. 26, no. 2, pp. 214–219, 1978.

[32] C. A. Balanis, *Antenna Theory: Analysis and Design.* Wiley Interscience, 2005.

[33] J. Volakis, *Antenna Engineering Handbook, 4th Ed,.* McGrawHill Companies. Inc., 2007.

[34] H. G. Booker, "Slot aerials and their relation to complementary wire aerials (Babinet's principle)," *Journal of the Institution of Electrical Engineers-Part IIIA: Radiolocation*, vol. 93, no. 4, pp. 620–626, 1946.

[35] S. Clauzier, S. M. Mikki, A. Shamim, and Y. M. Antar, "A new method for the design of slot antenna arrays: Theory and experiment," in *Proceedings of the 10th European Conference on Antennas and Propagation (EuCAP)*, pp. 1–5, 2016.

[36] D. K. Cheng, *Field and Wave Electromagnetics, 2nd ed.* Addison-Wesley, 1989.

[37] K. Song, Y. Fan, G. Yue, and B. Zhang, "Novel substrate integrated waveguide layer-to-layer transitions," in *Proceedings of the Asia-Pacific Microwave Conference*, pp. 1–4, 2008.

[38] V. A. Labay and J. Bornemann, "E-plane directional couplers in substrate-integrated waveguide technology," in *Proceedings of the Asia-Pacific Microwave Conference*, pp. 1–3, 2008.

[39] J. Wang, Y. Li, L. Ge, J. Wang, and K.-M. Luk, "A 60-GHz horizontally polarized magnetoelectric dipole antenna array with two-dimensional multi-beam end-fire radiation," *IEEE Transactions on Antennas and Propagation*, vol. 65, no. 11, pp. 5837–5845, 2017.

[40] N. Grigoropoulos, B. Sanz-Izquierdo, and P. R. Young, "Substrate integrated folded waveguides (SIFW) and filters," *IEEE Microwave and Wireless Components Letters*, vol. 15, no. 12, pp. 829–831, 2005.

[41] Z. C. Hao, W. Hong, X. P. Chen, J. X. Chen, K. Wu, and T. J. Cui, "Multilayered substrate integrated waveguide (MSIW) elliptic filter," *IEEE Microwave and Wireless Components Letters*, vol. 15, no. 2, pp. 95–97, 2005.

[42] J. Meyler, K. Garb, and R. Kastner, "Waveguide E-plane folded cross-coupled filters," in *Proceedings of the 2013 IEEE International Conference on Microwaves, Communications, Antennas and Electronics Systems*, pp. 1–5, 2013.

[43] T.-M. Shen, C.-F. Chen, T.-Y. Huang, and R.-B. Wu, "Design of vertically stacked waveguide filters in LTCC," *IEEE Transactions on Microwave Theory and Techniques*, vol. 55, no. 8, pp. 1771–1779, 2007.

[44] S. B. Cohn, "Direct-coupled-resonator filters," *Proceedings of the IRE*, vol. 45, no. 2, pp. 187–196, 1957.

[45] R. Levy, "Theory of direct-coupled-cavity filters," *IEEE Transactions on Microwave Theory and Techniques*, vol. 15, no. 6, pp. 340–348, 1967.

[46] J. Uher, J. Bornemann, and U. Rosenberg, *Waveguide Components for Antenna Feed Systems: Theory and CAD.* Artech House, 1993.

[47] G. Matthaei, L. Young, and E. Jones, *Microwave Filters, Impedance-Matching Networks, and Coupling Structures.* Artech House, 1980.

[48] Q. Wang and J. Bornemann, "Synthesis and design of direct-coupled rectangular waveguide filters with arbitrary inverter sequence," in *Proceedings of the 16th International Symposium on Antenna Technology and Applied Electromagnetics*, pp. 1–6, 2014.

[49] Z. Kordiboroujeni, F. Taringou, and J. Bornemann, "Efficient mode-matching design of substrate-integrated waveguide filters," in *Proceedings of the 42nd European Microwave Conference*, pp. 253–256, 2012.

[50] K. Sellal, L. Talbi, T. Denidni, and J. Lebel, "Design and implementation of a substrate integrated waveguide phase shifter," *IET Microwaves, Antennas & Propagation*, vol. 2, no. 2, pp. 194–199, 2008.

[51] M. K. Eslamloo and P. Mohammadi, "Compact size, equal-length and unequal-width substrate integrated waveguide phase shifter," in *18th International Conference on Advanced Communication Technology*, pp. 373–376, 2016.

[52] B. Liu, W. Hong, Z. C. Hao, and K. Wu, "Substrate integrated waveguide 180-degree narrow-wall directional coupler," in *Proceedings of the Asia-Pacific Microwave Conference Proceedings*, vol. 1, pp. 3–pp, 2005.

[53] X. Xu, R. G. Bosisio, and K. Wu, "A new six-port junction based on substrate integrated waveguide technology," *IEEE Transactions on Microwave Theory and Techniques*, vol. 53, no. 7, pp. 2267–2273, 2005.

[54] Y. J. Cheng, K. Wu, and W. Hong, "Substrate integrated waveguide (siw) broadband compensating phase shifter," in *IEEE MTT-S International Microwave Symposium Digest*, pp. 845–848, 2009.

[55] C.-H. Tseng, C.-J. Chen, and T.-H. Chu, "A low-cost 60-GHz switched-beam patch antenna array with butler matrix network," *IEEE Antennas and Wireless Propagation Letters*, vol. 7, pp. 432–435, 2008.

[56] Q.-L. Yang, Y.-L. Ban, K. Kang, C.-Y.-D. Sim, and G. Wu, "SIW multibeam array for 5G mobile devices," *IEEE Access*, vol. 4, pp. 2788–2796, 2016.

[57] G. Adamidis and I. Vardiambasis, "Design and implementation of a 4x4 Butler-matrix switched-beam antenna array at the MCEMA lab of the T.E.I. of Crete," in *Proceedings of the 2005 WSEAS International Conference on Engineering Education*, pp. 374–379, 2005.

[58] Y. J. Cheng, W. Hong, and K. Wu, "Millimeter-wave multibeam antenna based on eight-port hybrid," *IEEE Microwave and Wireless components letters*, vol. 19, no. 4, pp. 212–214, 2009.

[59] J.-S. G. Hong and M. J. Lancaster, *Microstrip filters for RF/microwave applications*. John Wiley & Sons, 2004.

[60] D. Deslandes, "Design equations for tapered microstrip-to-substrate integrated waveguide transitions," in *IEEE MTT-S International Microwave Symposium Digest*, pp. 704–707, 2010.

[61] D. Deslandes and K. Wu, "Integrated microstrip and rectangular waveguide in planar form," *IEEE Microwave and Wireless Components Letters*, vol. 11, no. 2, pp. 68–70, 2001.

[62] Z. Kordiboroujeni and J. Bornemann, "New wideband transition from microstrip line to substrate integrated waveguide," *IEEE Transactions on Microwave Theory and Techniques*, vol. 62, no. 12, pp. 2983–2989, 2014.

Appendix A

Additional Information

Duroid 5880 Data Sheet

ROGERS CORPORATION

Data Sheet

RT/duroid® 5870 /5880
High Frequency Laminates

RT/duroid® 5870 and 5880 glass microfiber reinforced PTFE composites are designed for exacting stripline and microstrip circuit applications.

The randomly oriented microfibers result in exceptional dielectric constant uniformity.

The dielectric constant of RT/duroid 5870 and 5880 laminates is uniform from panel to panel and is constant over a wide frequency range.
Its low dissipation factor extends the usefulness of RT/duroid 5870 and 5880 laminates to Ku-band and above.

RT/duroid 5870 and 5880 laminates are easily cut, sheared and machined to shape. They are resistant to all solvents and reagents, hot or cold, normally used in etching printed circuits or in plating edges and holes.

Normally supplied as a laminate with electrodeposited copper of ½ to 2 ounces/ft.^{2} (8 to 70μm) or reverse treated EDC on both sides, RT/duroid 5870 and 5880 composites can also be clad with rolled copper foil for more critical electrical applications. Cladding with aluminum, copper or brass plate may also be specified.

When ordering RT/duroid 5870 and 5880 laminates, it is important to specify dielectric thickness, tolerance, rolled, electrodeposited or reverse treated copper foil, and weight of copper foil required.

Features:

- Lowest electrical loss for reinforced PTFE material
- Low moisture absorption
- Isotropic
- Uniform electrical properties over frequency
- Excellent chemical resistance

Some Typical Applications:

- Commercial Airline Broadband Antennas
- Microstrip and Stripline Circuits
- Millimeter Wave Applications
- Military Radar Systems
- Missile Guidance Systems
- Point to Point Digital Radio Antennas

Advanced Connectivity Solutions
100 S. Roosevelt Avenue, Chandler, AZ 85226
Tel: 480-961-1382 Fax: 480-961-4533 www.rogerscorp.com

PROPERTY	TYPICAL VALUES RT/duroid 5870		TYPICAL VALUES RT/duroid 5880		DIRECTION	UNITS[3]	CONDITION	TEST METHOD
[1]Dielectric Constant, ε_r Process	2.33 2.33 ± 0.02 spec.		2.20 2.20 ± 0.02 spec.		Z Z	N/A	C24/23/50 C24/23/50	1 MHz IPC-TM-650 2.5.5.3 10 GHz IPC-TM 2.5.5.5
[4]Dielectric Constant, ε_r Design	2.33		2.20		Z	N/A	8 GHz - 40 GHz	Differential Phase Length Method
Dissipation Factor, tan δ	0.0005 0.0012		0.0004 0.0009		Z Z	N/A	C24/23/50 C24/23/50	1 MHz IPC-TM-650, 2.5.5.3 10 GHz IPC-TM-2.5.5.5
Thermal Coefficient of ε_r	-115		-125		Z	ppm/°C	-50 - 150°C	IPC-TM-650, 2.5.5.5
Volume Resistivity	2 X 10^7		2 X 10^7		Z	Mohm cm	C96/35/90	ASTM D257
Surface Resistivity	2 X 10^7		3 X 10^7		Z	Mohm	C/96/35/90	ASTM D257
Specific Heat	0.96 (0.23)		0.96 (0.23)		N/A	J/g/K (cal/g/C)	N/A	Calculated
Tensile Modulus	Test at 23 °C	Test at 100 °C	Test at 23 °C	Test at 100 °C	N/A			
	1300 (189)	490 (71)	1070 (156)	450 (65)	X	MPa (kpsi)	A	ASTM D638
	1280 (185)	430 (63)	860 (125)	380 (55)	Y			
ultimate stress	50 (7.3)	34 (4.8)	29 (4.2)	20 (2.9)	X			
	42 (6.1)	34 (4.8)	27 (3.9)	18 (2.6)	Y			
ultimate strain	9.8	8.7	6.0	7.2	X	%		
	9.8	8.6	4.9	5.8	Y			
Compressive Modulus	1210 (176)	680 (99)	710 (103)	500 (73)	X	MPa (kpsi)	A	ASTM D695
	1360 (198)	860 (125)	710 (103)	500 (73)	Y			
	803 (120)	520 (76)	940 (136)	670 (97)	Z			
ultimate stress	30 (4.4)	23 (3.4)	27 (3.9)	22 (3.2)	X			
	37 (5.3)	25 (3.7)	29 (5.3)	21 (3.1)	Y			
	54 (7.8)	37 (5.3)	52 (7.5)	43 (6.3)	Z			
ultimate strain	4.0	4.3	8.5	8.4	X	%		
	3.3	3.3	7.7	7.8	Y			
	8.7	8.5	12.5	17.6	Z			
Moisture Absorption	0.02		0.02		N/A	%	.062" (1.6mm) D48/50	ASTM D570
Thermal Conductivity	0.22		0.20		Z	W/m/K	80°C	ASTM C518
Coefficient of Thermal Expansion	22 28 173		31 48 237		X Y Z	ppm/°C	0-100°C	IPC-TM-650, 2.4.41
Td	500		500		N/A	°C TGA	N/A	ASTM D3850
Density	2.2		2.2		N/A	gm/cm³	N/A	ASTM D792
Copper Peel	27.2 (4.8)		31.2 (5.5)		N/A	pli (N/mm)	1 oz (35mm) EDC foil after solder float	IPC-TM-650 2.4.8
Flammability	V-0		V-0		N/A	N/A	N/A	UL94
Lead-Free Process Compatible	Yes		Yes		N/A	N/A	N/A	N/A

[1] Specification values are measured per IPC-TM-650, method 2.5.5.5 @ ~10GHz, 23°C. Testing based on 1 oz. electrodeposited copper foil. e_r values and tolerance reported by IPC-TM-650 method 2.5.5.5 are the basis for quality acceptance, but for some products these values may be incorrect for design purposes, especially microstrip designs. We recommend that prototype boards for new designs be verified for desired electrical performance.
[2] Typical values should not be used for specification limits, except where noted.
[3] SI unit given first with other frequently used units in parentheses.
[4] The design Dk is an average number from several different tested lots of material and on the most common thickness/s. If more detailed information is required, please contact Rogers Corporation. Refer to Rogers' technical paper "Dielectric Properties of High Frequency Materials" available at http://www.rogerscorp.com.

Standard Thickness	Standard Panel Size	Standard Copper Cladding	Non-Standard Copper Cladding
0.005" (0.127mm) 0.031" (0.787mm) 0.010" (0.254mm) 0.062" (1.575mm) 0.015" (0.381mm) 0.125" (3.175mm) 0.020" (0.508mm) Non-standard thicknesses are available	18" X 12" (457 X 305mm) 18" X 24" (457 X 610mm) Non-standard sizes are available up to 18" X 48" (457 X 1219 mm)	½ oz. (18µm) and 1 oz. (35µm) electrodeposited and rolled copper foil	¼ oz. (9 µm) electrodeposited copper foil ½ oz. (18µm), 1 oz. (35µm) and 2 oz. (70µm) reverse treat copper foil 2 oz. (70µm) electrodeposited and rolled copper foil
		Thick metal claddings may be available based on dielectric and plate thickness. Contact customer service for more information on available non-standard and custom thicknesses, claddings and panel sizes	

Eccosorb Material Data Sheet

EMERSON & CUMING MICROWAVE PRODUCTS

RoHS Compliant

ECCOSORB® GDS

High-Loss Silicone Rubber Sheet

Material Characteristics

- Thin, flexible, electrically non-conductive silicone rubber sheet
- Frequency range from 6 - 35 GHz
- Does not support fungal growth per MIL-STD-810E
- Impervious to moisture and can be subjected to moisture with no adverse effects
- Low out-gassing properties for space applications
- Can be cut and fitted to compound curves

Applications

- When placed within a cavity ECCOSORB® GDS has proven to be very effective at dampening resonances due to the absorbers high permittivity and permeability
- When bonded to a metal surface, ECCOSORB® GDS will significantly reduce the reflectivity of metal objects or structures due to the flow of microwave currents on that surface
- It can be applied to antenna elements, microwave dishes, the inner or outer surfaces of waveguides for isolation, attenuation, or modification of radiating patterns.
- When applied to side or even rear surfaces of certain objects, ECCOSORB® GDS will cause a significant reduction in "head on" reflectivity or backscattering.
- Although not intended as a specular absorber, it will reduce metal plate reflectivity by a few dB.

Instructions for Use

- ECCOSORB® GDS should be bonded to a metal surface for optimal *reflectivity* performance. If a metal surface is not available, it can be supplied upon request with an aluminum foil backing (ML) designated as GDS/ML

Typical Properties

Electrical Properties taken at 8.6 GHz

Service Temperature	Cryogenic to 350°F (177°C)
Specific Gravity (g/cc)	3.6
Volume Resistivity	$>10^{11}$ ohm-cm
Hardness, Shore A	>70
%TML (with SS6M)	0.2 (0.33)
%CVCM (with SS6M)	0.081 (0.09)
Dielectric Constant e'	13
Dielectric Loss Tangent, tan δ_d	0.2
Magnetic Permeability, μ'	1.7
Magnetic Loss Tangent, tan δ_m	0.78
Weight, lbs/ft^2 (kg/m^2)	0.6 (2.92)
Weight, lbs/ft^2 (kg/m^2) with SS6M PSA	0.7 (3.41)

Availability

- ECCOSORB® GDS is available in sheets 0.030" x 12" x 12" (0.076 cm x 30.5 cm x 30.5 cm)
- Upon special request, ECCOSORB® GDS can be supplied in sheets up to 36" (914.4mm) in length
- It can be supplied with a Pressure Sensitive Adhesive (PSA). Product designation denoting ECCOSORB® GDS with a PSA is ECCOSORB® GDS/SS6M
- ECCOSORB® GDS is available in other sizes and customer specified configurations and thicknesses upon request

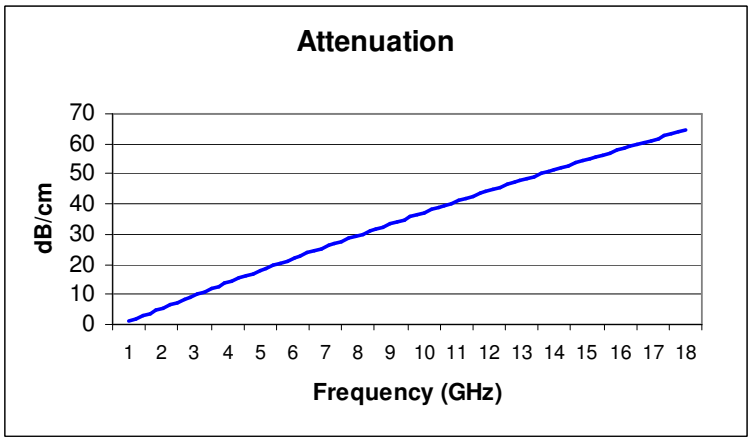

End-Launch Connector Data Sheet

DWG No.:

91Y60926

NOTE: Information herein is believed by Southwest Microwave, Inc. to be accurate. However, Southwest Microwave assumes no responsibility for any omissions or errors or inaccuracies for its use or for any infringements of patents or other rights of third parties that may result from its use. Data is intended for informational purpose only and does not constitute a contract of sale or any express or implied warranty, including any warranty of merchant ability or fitness for a particular purpose.

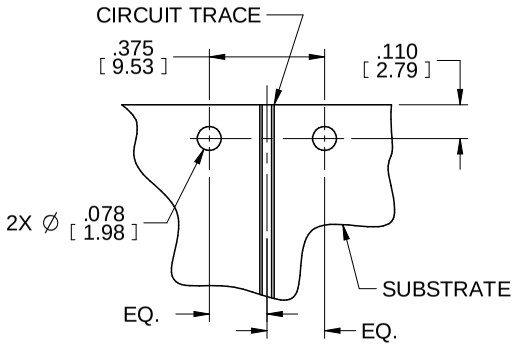

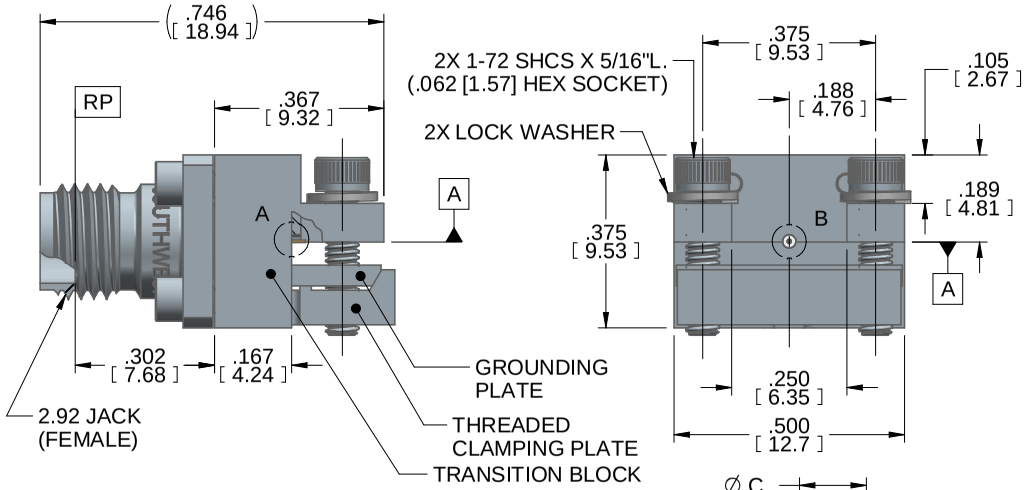

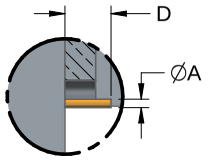

DETAIL A

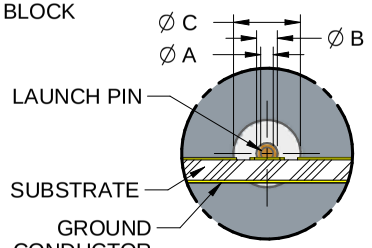

DETAIL B

Model	Ø A	Ø B	Ø C	D
1092-03A-6	.010	.020	.0635	.050
1092-02A-6	.007	.015	.0480	.030
1092-04A-6	.007	.012	.0390	.030
1092-01A-6	.005	.009	.0290	.030

HOUSING:	STEEL, CRES ALLOY UNS-30300 PER ASTM A582 PASSIVATED PER ASTM A967-99
CONTACT:	BeCu UNS-C17300 PER ASTM B196 GOLD PLATE PER MIL-DTL-45204
BEAD:	KEL-F (PCTFE) PER ASTM D1430
CAPTURE BEAD:	ULTEM 1000 PER ASTM D5205
ITEM	MATERIAL & FINISH
2.92 CONNECTOR	

TRANSITION BLOCK, GROUNDING PLATE, THREADED CLAMPING PLATE	C360 BRASS ALLOY UNS-C36000 PER ASTM B16. NICKEL PLATE PER AMS 2404B
LAUNCH PIN:	BeCu UNS-C17300 PER ASTM B196 GOLD PLATE PER MIL-DTL-45204
TRANSITION BLOCK DIELECTRIC:	VIRGIN PTFE FLUOROCARBON PER ASTM D1710, TYPE 1 GRADE 1, CLASS B
ITEM	MATERIAL & FINISH
TRANSITION BLOCK	

1. ALL DIMENSIONS ARE IN INCHES. ALL ANGLES ARE IN DEGREES. DIMENSIONS SHOWN IN BRACKETS [XXX] ARE IN MILLIMETERS.

NOTES: UNLESS OTHERWISE SPECIFIED.

REV		APRVD.	DATE:
A	RELEASE	PLC	10/1/12

SOUTHWEST MICROWAVE

Southwest Microwave, Inc.
9055 South McKemy Street
Tempe, Arizona 85284-2946
Telephone (480) 783-0201
Fax (480) 783-0360

TITLE

2.92mm JACK (FEMALE) END LAUNCH CONNECTOR LOW PROFILE

DRN BY:	DATE:	DWG. NO.	REV.
EAG	09/26/12	91Y60926	A

SHEET: 1 OF 1

1-Dimensional Reflection Coefficients of Figure 4.6

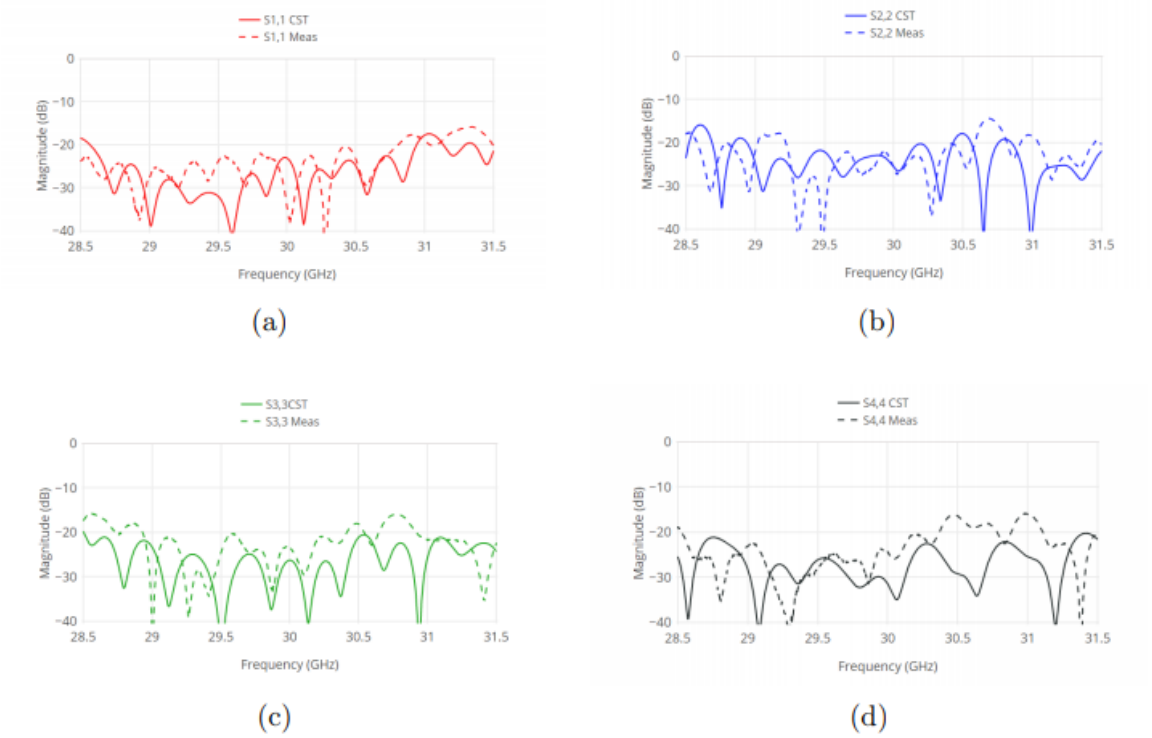

Figure: Separated images of the reflection coefficients (Ports 1 through 4) of the 1-dimensional beamforming network